

**UNIVERSIDADE FEDERAL DE ALAGOAS
CENTRO DE TECNOLOGIA
PROGRAMA DE PÓS-GRADUAÇÃO EM MATERIAIS**

ARNALDO DOS SANTOS JÚNIOR

**APPLICATION OF TOPOLOGY OPTIMIZATION FOR THE OPTIMAL DESIGN OF
PERIODIC CELLULAR MATERIALS EMPLOYING THE FINITE-VOLUME
THEORY**

**MACEIÓ
2024**

ARNALDO DOS SANTOS JÚNIOR

**APPLICATION OF TOPOLOGY OPTIMIZATION FOR THE OPTIMAL DESIGN OF
PERIODIC CELLULAR MATERIALS EMPLOYING THE FINITE-VOLUME
THEORY**

Tese de Doutorado apresentada ao Programa de Pós-Graduação em Materiais da Universidade Federal de Alagoas, como requisito parcial para obtenção do título de Doutor em Ciências com ênfase em Materiais.

Orientador: Prof. Dr. Márcio André Araújo Cavalcante

**MACEIÓ
2024**

Catálogo na Fonte
Universidade Federal de Alagoas
Biblioteca Central
Divisão de Tratamento Técnico

Bibliotecário: Marcelino de Carvalho Freitas Neto – CRB-4 – 1767

S237a Santos Júnior, Arnaldo dos.
Application of topology optimization for the optimal design of periodic cellular materials employing the finite-volume theory / Arnaldo dos Santos Júnior. – 2024.
80 f. : il.

Orientador: Márcio André Araújo Cavalcante.
Tese (doutorado em Materiais) – Universidade Federal de Alagoas. Centro de Tecnologia. Programa de Pós-Graduação em Materiais. Maceió, 2024.
Texto em inglês.

Bibliografia: f. 68-74.
Apêndices: f. 75-80.

1. Material celular. 2. Teoria da homogeneização. 3. Otimização topológica. 4. Teoria de volumes finitos. I. Título.

CDU: 66.09

Arnaldo dos Santos Júnior

**APPLICATION OF TOPOLOGY OPTIMIZATION FOR THE
OPTIMAL DESIGN OF PERIODIC CELLULAR MATERIALS
EMPLOYING THE FINITE-VOLUME THEORY**

Tese apresentada ao Programa de Pós-Graduação em Materiais da Universidade Federal de Alagoas e aprovada em 08 de agosto de 2024.

BANCA EXAMINADORA

Documento assinado digitalmente
 **MARCIO ANDRE ARAUJO CAVALCANTE**
Data: 08/08/2024 19:24:22-0300
Verifique em <https://validar.iti.gov.br>

Prof. Dr. Márcio André Araújo Cavalcante (Orientador – PPGMateriais/UFAL)

Documento assinado digitalmente
 **SEVERINO PEREIRA CAVALCANTI MARQUES**
Data: 08/08/2024 19:31:09-0300
Verifique em <https://validar.iti.gov.br>

Prof. Dr. Severino Pereira Cavalcanti Marques (CTEC/UFAL)

Documento assinado digitalmente
 **EDUARDO NOBRE LAGES**
Data: 08/08/2024 19:38:43-0300
Verifique em <https://validar.iti.gov.br>

Prof. Dr. Eduardo Nobre Lages (CTEC/UFAL)

Documento assinado digitalmente
 **SILVANA MARIA BASTOS AFONSO DA SILVA**
Data: 09/08/2024 11:22:45-0300
Verifique em <https://validar.iti.gov.br>

Prof^a. Dr^a. Silvana Maria Bastos Afonso da Silva (UFPE)

Documento assinado digitalmente
 **EDUARDO ALBERTO FANCELLO**
Data: 09/08/2024 12:05:09-0300
Verifique em <https://validar.iti.gov.br>

Prof. Dr. Eduardo Alberto Fancello (UFSC)

Documento assinado digitalmente
 **VOLNEI TITA**
Data: 09/08/2024 12:14:31-0300
Verifique em <https://validar.iti.gov.br>

Prof. Dr. Volnei Tita (USP)

To my wife, Vera Nbia, my tireless partner in life, and every step of this journey, your support has been my greatest strength. To my children, Maria Clara, Louise, and Nicolas, whose boundless curiosity inspires me daily, you are my deepest motivation, and I love you all beyond words!

ACKNOWLEDGMENTS

I am deeply grateful to my parents, Arnaldo Santos and Edileide Carvalho, for their unconditional support and the values they taught me. You have always believed in me, even in the most challenging moments, giving me the strength and motivation to move forward. I am eternally grateful for everything you have done and continue to do for me.

I want to thank my professor and friend, Márcio Cavalcante, for the countless hours of guidance and dedication to this work. Thank you so much!

To the examining professors Severino Marques, Eduardo Nobre, Volnei Tita, Silvana Silva, and Eduardo Fancello, whose contributions were essential to improving the final version of this dissertation.

I am grateful to my PhD colleagues Marcelo Araujo, Wesley Sampaio, Jéssica Dantas, and Vinícius Correia for our mutual support and enriching discussions throughout this journey. Your companionship and knowledge exchange were fundamental in making this experience lighter and more meaningful.

To my friend Romildo Escarpini Filho, I am immensely grateful for always being available to discuss ideas and for guiding me through moments of doubt.

RESUMO

A otimização topológica é uma técnica empregada na engenharia para determinar a distribuição ótima de material dentro de um domínio de projeto definido para várias aplicações. Essa técnica tem sido aplicada ao projeto de materiais celulares visando criar um arranjo microestrutural eficiente que atenda aos critérios de desempenho necessários e minimize o peso do material. Este trabalho apresenta uma abordagem inovadora que combina princípios da teoria dos volumes finitos, métodos de homogeneização e otimização topológica baseada em densidade para projetar materiais celulares periódicos altamente eficientes com propriedades elásticas macroscópicas otimizadas. Os métodos de homogeneização aplicado a materiais periódicos, baseados no conceito de célula unitária, determinam as propriedades elásticas efetivas do material celular como uma etapa intermediária no procedimento de otimização topológica. Para encontrar a topologia microestrutural ótima, são consideradas combinações lineares específicas das componentes da matriz constitutiva efetiva a fim de obter propriedades elásticas extremas, como máximos módulos de cisalhamento e volumétrico ou coeficiente de Poisson negativo, considerando uma restrição de volume prescrita. A abordagem proposta utiliza uma estratégia baseada em funções potenciais de rigidez do material para penalizar densidades intermediárias do material e aplicar o método de continuação para minimizar a instabilidade decorrente de problemas de extremos locais. Exemplos numéricos envolvendo materiais com microestruturas celulares periódicas são analisados, e os resultados encontrados demonstram o excelente desempenho da teoria dos volumes finitos para o projeto ótimo de materiais celulares.

Palavras-chave: Materiais celulares. Homogeneização. Otimização topológica. Teoria de volumes finitos.

ABSTRACT

Topology optimization is a technique employed in engineering to determine the optimal distribution of material within a defined design domain for various applications. This technique has been applied to the design of cellular materials to create an efficient microstructural arrangement that meets the necessary performance criteria and minimizes the weight of the material. This work presents an innovative approach that combines principles from finite-volume theory, homogenization methods, and density-based topology optimization to design highly efficient periodic cellular materials with optimized macroscopic elastic properties. The homogenization methods applied to periodic materials based on the unit cell concept determine the effective elastic properties of cellular material as an intermediate step in the topology optimization procedure. To find the optimal microstructural topology, specific linear combinations of components of the effective constitutive matrix are considered to obtain extreme elastic properties, such as maximum shear and bulk moduli or negative Poisson's ratio, considering a prescribed volume constraint. The proposed approach uses a strategy based on potential functions of material stiffness to penalize intermediate material densities and apply the continuation method to minimize instability arising from the extreme local problem. Numerical examples involving materials with periodic cellular microstructures are analyzed, and the results demonstrate the excellent performance of the finite-volume theory for the optimal design of cellular materials.

Keywords: Cellular materials. Homogenization. Topology optimization. Finite-volume theory.

FIGURE LIST

Figure 1 – Illustration of a topologically optimized craniofacial skeletal region . . .	15
Figure 2 – Unfiltered topologies presenting checkerboard patterns	16
Figure 3 – The representation of discretized analysis domain and local coordinate system of a generic subvolume (q)	22
Figure 4 – Enforcing PBC to an RUC which leads to the elimination of redundant degrees of freedom	25
Figure 5 – Average number of degrees of freedom	26
Figure 6 – Microstructural periodic arrangement with three different squares representative unit cells	27
Figure 7 – RVE and RUC of a periodic composite material	29
Figure 8 – Effective elastic moduli estimated by different approaches	33
Figure 9 – Publications on topology optimization restricted to the search fields: engineering, materials science, and multidisciplinary	35
Figure 10 – Effect of the material penalization parameter	38
Figure 11 – Illustration of filtering technique	42
Figure 12 – Illustrative analysis domain employed in the Cartesian coordinates formulation of the FVT	44
Figure 13 – Comparison of material density distribution considering the continuation scheme with the increment $\Delta p = 1$ for the SIMP and RAMP methods	50
Figure 14 – Evolutionary trajectory of the maximized shear modulus	52
Figure 15 – Maximized bulk modulus for different optimized topologies and the HS upper bound as a function of the volume fraction constraint (ϑ), considering no-filtering scenario	59
Figure 16 – Maximized bulk modulus for different optimized topologies and the HS upper bound as a function of the volume fraction constraint ϑ, considering filtering applications	60
Figure 17 – Normalized macroscopic elastic modulus for rotated axes relative to the material principal axes: shear modulus maximization	61
Figure 18 – Normalized macroscopic elastic modulus for rotated axes relative to the material principal axes: bulk modulus maximization	62
Figure 19 – Flowchart of the TopMatFVT for the topology optimization of periodic cellular materials	80

TABLE LIST

Table 1 – Optimized topologies with maximized shear modulus employing Top-MatFVT and topX codes	46
Table 2 – Optimized topologies with maximized shear modulus employing continuation method	48
Table 3 – Optimized topologies with maximized shear modulus employing fixed penalization	49
Table 4 – Impact of initial material design on the optimized topology with maximized shear modulus	53
Table 5 – Impact of initial material design on the optimized topology with maximized shear modulus considering different repeat unit cells with the same periodic arrangement	54
Table 6 – Optimized topologies with maximized shear modulus, considering four levels of volume fraction constraints (ϑ)	55
Table 7 – Optimized topologies with maximized bulk modulus for fixed solid volume fractions constraint of 50%, considering four values of Poisson’s ratio (ν)	57
Table 8 – Optimized topologies with maximized bulk modulus, considering four levels of volume fraction constraints (ϑ)	58
Table 9 – Optimized topologies with negative Poisson’s ratio for a fixed $\beta = 0.8$, considering four levels of volume fraction constraints (ϑ)	64
Table 10 – Optimized topologies with negative Poisson’s ratio for a fixed volume fraction constraints of 50%, considering other two values of β parameter	64

LIST OF ABBREVIATIONS

BESO	Bidirectional evolutionary structural optimization
CFD	Computational fluid dynamics
DOF	Degrees of freedom
ESO	Evolutionary structural optimization
FEM	Finite element method
FVDAM	Finite-volume direct averaging micromechanics
FVT	Finite-volume theory
GMC	Generalized method of cells
HFGMC	High-fidelity generalized method of cells
HOTFGM	Higher-order theory for functionally graded materials
HS	Hashin-Shtrikman
MEMS	Microelectromechanical systems
MMA	Method of moving asymptotes
OC	Optimality criteria
PBC	Periodic boundary conditions
RAMP	Rational approximation of material properties
RUC	Repeating unit cell
SIMP	Solid isotropic material with penalization
TO	Topology optimization
TopMatFVT	Topology optimization of material with finite-volume theory

SYMBOLS LIST

CHAPTER 2

$u_i^{(q)}$	Displacement field in the q th subvolume
$u_i'^{(q)}$	Fluctuating displacement components
$\bar{\epsilon}_{ij}$	Macroscopic strains
$W_{i(mn)}^{(q)}$	Unknown displacement field coefficients
l_q	Subvolume dimension in horizontal direction
h_q	Subvolume dimension in vertical direction
$\hat{u}_i'^{(q,f)}$	Surface-averaged fluctuating displacement components at the subvolume faces
$\hat{\mathbf{u}}'^{(q)}$	Surface-averaged fluctuating displacement vector
$\hat{u}_i'^{(q,f)}$	Surface-averaged fluctuating displacement components at the subvolume faces
$\hat{\mathbf{u}}'^{(q)}$	Surface-averaged fluctuating displacement vector
$\hat{t}_i^{(q,f)}$	Surface-averaged traction components at the subvolume faces
$\hat{\mathbf{t}}^{(q)}$	Surface-averaged traction vector
$\mathbf{N}^{(q)}$	Matrix containing components of normal vector at the subvolume faces
$\mathbf{C}^{(q)}$	Constitutive matrix of the subvolume q
$\mathbf{R}^{(q)}$	Resultant of forces acting at the subvolume faces
$\hat{\mathbf{H}}^{(q)}$	Macroscopic load at the subvolume level
$\mathbf{K}^{(q)}$	local stiffness matrix (non-symmetric)
$\hat{\mathbf{K}}^{(q)}$	Modified local stiffness matrix (symmetric)
$\hat{\mathbf{F}}$	Global load vector
$\hat{\mathbf{K}}$	Global stiffness matrix
$\hat{\mathbf{L}}^{(q)}$	Matrix containing the subvolume face dimensions
N_q	Total number of subvolumes

N_x	Number of subvolumes in horizontal direction
N_y	Number of subvolumes in vertical direction
ndof	Number of degrees of freedom
$\mathbf{Q}^{(q)}$	Kinematic and static compatibility matrices

CHAPTER 3

ε_{ij}	Kinematically admissible strain field
σ_{ij}	Statically admissible stress field
C_{ijkl}	Four-order elastic material constitutive tensor
\mathbf{C}	Constitutive matrix
E	Young's modulus
ν	Poisson's ratio
V	Domain of representative volume element
Ω	Domain of repeating unit cell
S	Boundary surface of representative volume element
ε_{ij}^0	Uniform symmetry strain tensor
$\bar{\varepsilon}_{ij}$	Average strain tensor on the domain V
ε'_{ij}	Fluctuating strain tensor due to the heterogeneous microstructure
$\bar{\varepsilon}_{ij}^\Omega$	Average strain tensor over the repeating unit cell
U	Structural Strain energy
\bar{U}	Strain energy density
$W^{(q)}$	Work done by external forces at the subvolume
$\bar{\varepsilon} _{(.)}$	Macroscopic strain case (.)
$\hat{\mathbf{u}}^{(q)}$	Surface-averaged displacement field
$\hat{\mathbf{u}}^{(q)} _{(.)}$	Surface-averaged displacement field due to the application of macroscopic strain case (.)
\mathbf{C}^*	Effective constitutive matrix

C_{ij}^*	Effective constitutive matrix components
$\mathbb{A}^{(q)}$	Elastic strain concentration tensor
$c^{(q)}$	Volume fraction of the subvolume q

CHAPTER 4

ρ_q	Density design variable
$\boldsymbol{\rho}$	Density vector
E_q	Young's modulus of the subvolume q
E_0	Young's modulus of the solid material
E_{min}	Minimum Young's modulus (void)
p	Material penalization parameter
$\hat{\mathbf{K}}^{(q)}$	Modified local stiffness matrix
$\hat{\mathbf{K}}^0$	Modified local stiffness matrix considering a unit Young's modulus
κ^*	Effective bulk modulus
μ^*	Effective shear modulus
E^*	Effective Young's modulus
ϕ	Objective function
ϑ	Solid volume fraction constraint
v_q	Volume of the q th subvolume
α_{ij}	Weight factor, which defines diverse objective functions
$\hat{\mathbf{u}}' _{(i)}$	Global surface-averaged fluctuating displacement vector due to the application of the strain case (i)
$\hat{\mathbf{F}} _{(i)}$	Global load vector due to the application of the strain case (i)
$\bar{\mathbf{B}}^{(q)}$	Strain/displacement operator
$\hat{\boldsymbol{\lambda}}^{(q)}$	Adjoint vector solution
β_q	Optimality condition
$iter$	Design iteration number

m	Move limit in optimality criteria method
η	Numerical damping factor in optimality criteria method
λ	Lagrangian multiplier
H_{qi}	Convolution operator
r_{fil}	Filter radius
$\frac{\widehat{\partial\phi}}{\partial\rho_q}$	Modified subvolumes sensitivities
$\widetilde{\rho}_q$	Modified subvolumes densities

SUMMARY

1	INTRODUCTION	14
1.1	Motivation	14
1.2	Objectives	17
1.3	Contribution and its Highlights	18
2	FINITE-VOLUME THEORY	19
2.1	A Brief Overview	19
2.2	Standard Formulation for Periodic Materials	21
2.2.1	Displacement field representation	21
2.2.2	Local stiffness matrix calculation	22
2.2.3	Global stiffness matrix assembly	24
2.2.4	Order of magnitude of the problem	25
3	NUMERICAL HOMOGENIZATION	27
3.1	Fundamental Concepts	27
3.2	Linear Elasticity	28
3.3	Average-strain Theorem	29
3.3.1	Periodicity conditions and the average-strain	30
3.4	Effective Properties of Periodic Materials	30
3.4.1	Strain energy-based approach	31
3.4.2	Mean-field theory approach	32
4	TOPOLOGY OPTIMIZATION	34
4.1	Density-based Approach	35
4.1.1	Hashin-Shtrikman bounds for two-phase materials	37
4.1.2	Problem formulation for material design	39
4.2	Sensitivity Analysis	40
4.3	Optimality Criteria Method	40
4.4	Filtering Techniques	41
4.5	Continuation Method	42
5	NUMERICAL EXAMPLES	44

5.1	Initial Remarks	44
5.2	Cellular Materials Shear Modulus Maximization	45
5.2.1	Comparison with finite element analysis	45
5.2.2	Influence of the continuation method	47
5.2.3	Impact of initial material design	52
5.2.4	Influence of volume fraction constraint	54
5.3	Cellular Materials Bulk Modulus Maximization	55
5.3.1	Influence of Poisson's ratio	56
5.3.2	Influence of volume fraction constraint	57
5.3.3	Comparison with the Hashin-Shtrikman upper bound	58
5.4	Cellular Materials with Negative Poisson's ratio	62
5.4.1	Influence of volume fraction constraint	63
6	CONCLUSIONS	65
	REFERENCES	68
	APPENDIX A – SENSITIVITY EQUATIONS	75
	APPENDIX B – COMPUTATIONAL PROCEDURE	79

1 INTRODUCTION

1.1 Motivation

Over the past few decades, cellular materials have attracted research attention and found numerous applications across various industry sectors due to their flexibility in tailoring optimized microstructural layouts. These materials possess advantageous properties that make them especially valuable in aerospace, automotive, construction, architecture, and other areas where reducing weight while enhancing stiffness is crucial. Inspired by their significant prevalence in nature, demonstrated by structures like bamboo and human bone tissue, cellular materials are becoming increasingly commonplace in structural design. Specifically in biomedical engineering, structures often made of cellular materials, so-called scaffold materials, have inspired the development of innovative designs for bone tissue engineering. Chen et al. (2020) assert that these scaffolds provide a porous structure and ample space for cell accommodation, low Young's modulus, and high compressive strength.

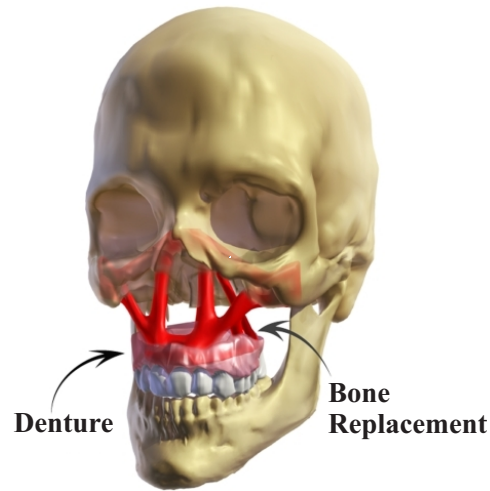
However, the primary challenge in material design is creating an efficient structural layout that meets the required performance criteria while minimizing material weight. Engineers have employed topology optimization (TO) techniques to address this challenge and develop optimal microstructures that enhance structural performance by systematically distributing material within a given design domain. Since the pioneering work on the homogenization method by Bendsøe and Kikuchi (1988), topology optimization has rapidly grown and successfully applied to practical applications, including material design, heat transfer, acoustics, fluid dynamics, aeroelasticity, and other multi-physics systems (Deaton; Grandhi, 2013).

The advancements of topology optimization techniques have been driven by the refinement of classical methods and the emergence of promising new approaches. One widely used method is the density-based strategy, which includes, among others, the solid isotropic material with penalization (SIMP) method (Bendsøe, 1989; Zhou; Rozvany, 1991; Rozvany et al., 1992) and rational approximation of material properties (RAMP) developed by Stolpe and Svanberg (2001). These methods utilize a non-linear interpolation model to handle material properties effectively and aim to penalize intermediate density values, providing the “most relaxed” problem and preventing the occurrence of gray regions seen in the homogenization method introduced by Bendsøe and Kikuchi (1988).

Nowadays, the integration of advanced computer simulations and topology optimization techniques has revolutionized the field of surgical interventions, particularly in designing patient-specific extensive craniofacial segmental bone replacements. These personalized bone replacements are crucial in restoring normal function and appearance in massive facial injuries resulting in bone loss (Sutradhar et al., 2010). Furthermore, the advancements in manufacturing processes have made it possible to transform engineering ideas into completely functional and robust structures, regardless of their complicated geometry, including architectures composed of

porous, graded, or composite materials (Collet et al., 2018; Bose et al., 2018; Wu et al., 2021). Figure 1 illustrates the simulated optimal bone topology inserted into the skull, highlighting the practical feasibility of the final configuration. It demonstrates how integrating computer simulations and topology optimization techniques can effectively contribute to successfully implementing personalized bone replacements.

Figure 1 – Illustration of a topologically optimized craniofacial skeletal region

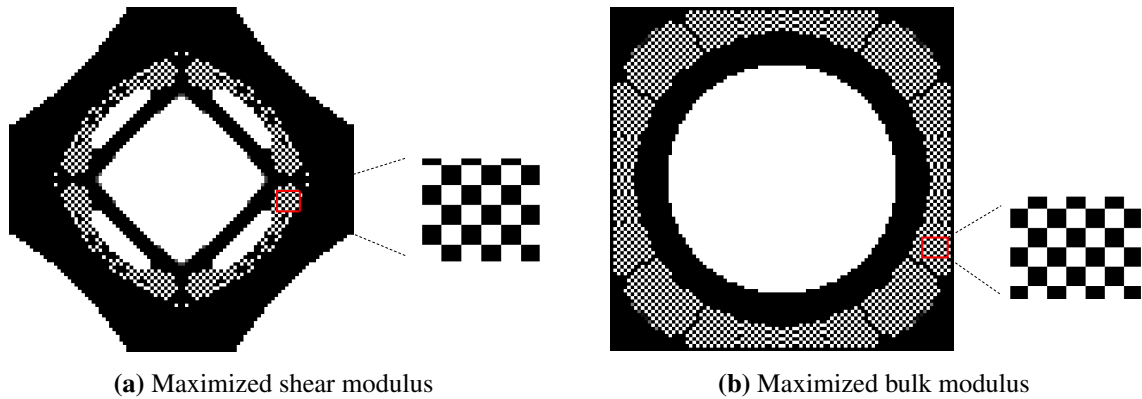


Font: Sutradhar et al. (2010).

Traditionally, topology optimization problems have predominantly been solved using the well-established finite element method (FEM). However, despite the advancements, challenges like numerical instability as checkerboard patterns persist in simulations, demanding a regularization scheme, especially when employing linear triangular and quadrilateral finite elements, leading to undesired final topology that does not represent a manufacturable optimal material distribution. The term “checkerboard” refers to forming regions composed of alternating solid-and-void elements arranged in a checkerboard-like fashion. Díaz and Sigmund (1995) assert that checkerboard patterns arise in topology design because these material arrangements exhibit artificially increased stiffness in continuous layout optimization problems of compliance minimization when employing lower-order quad or triangular elements.

Figure 2 illustrates microstructures with maximized elastic properties generated running the topX educational FEM code developed by Xia and Breitkopf (2015). These results, produced without any regularization filter, inspire developing strategies to achieve checkerboard-free designs without necessarily employing filtering techniques.

Figure 2 – Unfiltered topologies presenting checkerboard patterns



Font: Through topX educational code.

Numerous alternatives employing finite element analysis have been developed to address the checkerboard pattern instability in topological design for minimum compliance-based problems. Sigmund and Petersson (1998) tackled this issue by employing high-order finite elements, which enhance the accuracy of the solutions and reduce numerical instabilities associated with lower-order elements. Jang et al. (2003) proposed using non-conforming elements, which do not follow traditional finite elements' standard connectivity and shape functions, providing greater flexibility and stability in the optimization process and effectively reducing numerical issues as the checkerboard pattern problems. Talischi et al. (2012) introduced isoparametric polygonal elements, which extend the capabilities of traditional linear triangles and bilinear quadrilaterals by offering a more versatile and robust element formulation that can adapt better to complex geometries. More recently, Kumar (2022) developed a topology optimization approach employing hexagonal elements, providing optimal space-filling and mechanical performance, making them highly suitable for advanced structural designs. These diverse strategies highlight the continuous efforts to refine topology optimization techniques and overcome the checkerboard problem, ensuring more reliable and manufacturable designs in engineering applications.

Araujo (2018) significantly contributed to structural topology optimization problems by employing the finite-volume theory (FVT). This powerful numerical technique establishes connections between adjacent subvolume faces as a crucial part of the approach. Consequently, finite-volume theory procedures yield optimized structural designs that overcome the prevalent problem of checkerboard regions, enhancing overall effectiveness. This important aspect has been consistently emphasized in a series of publications by Araujo (2018), Araujo et al., (2020a, 2020b), and Araujo (2022). They explained that the checkerboard region occurs due to the satisfaction of equilibrium and continuity conditions at the nodes of the elements, specifically for triangular and quadrilateral finite elements providing singular connectivity, which results in high-strain energy modes in these connections. On the other hand, the finite-volume theory ensures the satisfaction of equilibrium equations at the subvolume level, and the compatibility conditions (kinematic and static) are established through the interfaces between adjacent subvolumes in an average sense, resulting in one approach more closely with the continuum mechanics.

However, solutions to topology optimization problems in materials design still need to be improved, especially in the absence of a regularization scheme. The adoption of regularization techniques such as smoothing or filtering methods indeed becomes imperative to mitigate the occurrence of checkerboard patterns and ensure manufacturability within the density-based topology optimization schemes, as advocated by Andreassen et al. (2014), Xia and Breitkopf (2015), and other researchers in the field. Advancing in this context, the current study represents a continuation of the research initially proposed by Araujo (2018). Nonetheless, it deviates from the previous investigation by concentrating on designing periodic cellular materials with optimized elastic properties.

The present work involves a comprehensive analysis of two-dimensional problems modeled employing a periodic square unit cell, which can be interpreted as perforated sheets, commonly recommended for applications where the passage of water or air is crucial, such as in ventilation or filtration systems and usually are very light and thin (Hiremath, 2020). The perforated metal materials incorporate a range of properties, including rigidity, strength, lightweight, small thickness, a dosed transparency, and decorative attractiveness. All these features lead to new applications for the construction industry, as mentioned by Mironovs et al. (2017).

1.2 Objectives

This dissertation aims to introduce an innovative approach that synthesizes principles from finite-volume theory, homogenization methods, and density-based topology optimization to design high-performance periodic cellular materials. The focus lies on optimizing the material configuration at the microstructural level to achieve certain macroscopic properties, such as maximized shear and bulk moduli (Sigmund, 2000; Neves et al., 2000), and to attain a negative Poisson's ratio for auxetic materials (Sigmund, 1994a; Andreassen et al., 2014), while satisfying a prescribed volume fraction constraint without necessarily adopting filtering techniques. Specifically, the work has the following objectives:

- Propose a scientific density-based topology optimization methodology for periodic cellular materials based on finite-volume theory;
- Integrate two homogenization strategies into the topology optimization methodology and verify their computational efficiencies. These strategies include one based on strain energy equivalence and another employing the classical micromechanical mean-field theory;
- Apply the developed methodology to find a two-dimensional optimal microstructural topology, focusing on extreme elastic properties;
- Contribute to the academic community and engineers' motivation to develop strategies that yield optimized microstructures free from checkerboard patterns without necessarily employing filtering techniques.

1.3 Contribution and its Highlights

Two aspects justify this significant contribution: the first is that topology optimization techniques have never been applied to the design of periodic materials employing the finite-volume theory (the version developed explicitly for heterogeneous materials), as based on the author's knowledge. When employed in material design in the topology optimization context, this interesting theory achieves optimized microstructures free from the checkerboard pattern without incorporating additional constraints into the problem formulation, such as filtering techniques. The second aspect is the efficiency of the promising developed computational code TopMatFVT (Topology optimization of material with finite-volume theory), which enables the design of periodic materials with optimized properties and significantly enhances the practical utility in material design contexts.

2 FINITE-VOLUME THEORY

The scientific community and engineers commonly employ the finite-volume method to simulate various physical problems. This method ensures the satisfaction of the governing field equations (transport or equilibrium) within the control volumes of the discretized domain of interest in an integral sense, resulting in strict conservation. Moukalled et al. (2015) highlight that this essential feature, coupled with the method's simplicity and demonstrated stability, establishes the finite-volume procedure as a preferred choice in computational fluid dynamics (CFD) simulations. On the other hand, the acceptance of the finite-volume method within the heterogeneous materials mechanics community has been gradual, possibly due to multiple developed versions and often needing clarification with traditional fluid mechanics applications (Cavalcante et al., 2012).

The following sections provide a comprehensive historical perspective on the evolution of a significant technique used to address boundary-value problems in solid mechanics, advancements in applying it to periodic heterogeneous media unit cell problems, and the approach adopted in the present work.

2.1 A Brief Overview

The initial version of the finite-volume theory in the field of heterogeneous materials and structures has its origins in the higher-order theory for functionally graded materials (HOTFGM), developed in a sequence of papers and summarized by Aboudi et al. (1999). It provided the fundamental framework for constructing its homogenized counterpart for higher-order theory for periodic multiphase materials developed by Aboudi et al. (2001). After that, Aboudi et al. (2002) renamed this homogenized version to high-fidelity generalized method of cells (HFGMC).

The structural and homogenized versions of the higher-order theories were simplified by refining the analysis domain discretization and implementing a highly efficient local/global stiffness matrix approach compared to the original formulations (Bansal; Pindera, 2003; Zhong et al., 2004; Bansal; Pindera, 2005). Following this, Bansal and Pindera (2006) introduced a specific finite-volume theory for analyzing periodic materials within the homogenization framework, which they referred to as finite-volume direct averaging micromechanics (FVDAM). This approach is based on a direct averaging technique to satisfy the field equations within discretized subvolumes of the unit cell, in contrast with the original construction wherein higher-order moments of the equilibrium equations were also satisfied (Bansal; Pindera, 2006).

Later on, the reconstructed theories were further extended through a series of contributions that introduced parametric mapping, aiming to simplify the modeling of complex microstructures by employing arbitrary quadrilateral subvolumes. Cavalcante (2006) and Cavalcante et al. (2007a, 2007b) developed the parametric mapping strategy and applied it to the thermomechanical analysis of composites and functionally graded materials. After that, Gattu

(2007) and Gattu et al. (2008) employed this strategy to investigate periodic materials with elastic phases. In sequence, periodic materials with elastoplastic phases and periodic multilayers with wave architectures were examined by Khatam; Pindera (2009a and 2009b). Furthermore, Escarpini Filho (2010) employed the parametric mapping strategy to study the behavior of viscoelastic composite materials.

Cavalcante and Pindera (2012a) introduced a generalized finite-volume micromechanics theory applied to heterogeneous materials. This generalization systematically incorporates different orders to the zeroth-order finite-volume theory initially proposed by Bansal and Pindera (2003). In this approach, each order signifies a higher level of complexity in the displacement field. At each level, additional kinematic quantities are included and evaluated in an average sense at the subvolume faces. For instance, the first-order finite-volume theory introduces rotations in addition to the original version, while the second-order finite-volume theory incorporates both rotations and curvatures.

The finite-volume theory with parametric mapping has been widely employed to analyze multiphase heterogeneous materials in the last few years. In this context, Vieira and Marques (2019) introduced a new three-dimensional micromechanical model for evaluating the effective thermal conductivity of multiphase composite materials with periodic microstructure. Lages and Marques (2020) proposed implementation and application of an efficient strategy for computation of the average eigenstrain vector, which represents a crucial task required by the thermoelastic homogenization model. Yin et al. (2021) developed a novel homogenization theory for unidirectional composites with periodic domains and random fiber distributions, which treats the inclusions as meshfree components and uses discrete Fourier transforms to satisfy Navier's equations precisely. Zhao et al. (2023) accomplished a detailed parametric study to analyze the impact of microstructure effects and geometric parameters on the performance of piezoelectric composites, integrating the particle swarm optimization algorithm with multiphysics FVDAM to optimize the microstructure geometric parameters effectively and maximize the performance. In a recent study, Escarpini Filho and Almeida (2023) applied the FVDAM method for the first time in the numerical analysis of reinforced masonry. Despite its antiquity, it is a material known for its complex behavior and frequent need for structural reinforcement.

In the context of topology optimization for compliance minimization problems, the pioneer study employing the finite-volume theory was realized by Araujo (2018), which subsequently resulted in the publications by Araujo et al. (2020a, 2020b). These contributions demonstrated that applying the finite-volume theory can entirely control the numerical issue associated with the checkerboard patterns. Furthermore, Araujo (2022) conducts an energy analysis of continuum elastic structures using the generalized finite-volume theory. This analysis encompasses various aspects of mechanical energy estimation, focusing on rectangular subvolumes. Notably, the optimized structural topology achieved through this approach is entirely free from the checkerboard pattern for all orders of the generalized finite-volume theory investigated. Moreover, specifically for the zeroth-order (standard) finite-volume formulation, the equivalence

between the structural strain energy and the work done by external forces is ensured once the differential equilibrium equations are satisfied point-wise inside the subvolume. Furthermore, in the problems investigated by Araujo et al. (2020b), the final topologies achieved through the standard formulation exhibit fewer bars, most of which have lower slenderness ratios than those derived from higher-order approaches. These characteristics aligned with manufacturing process requirements were crucial in selecting this formulation for the current study, focusing on periodic cellular materials.

2.2 Standard Formulation for Periodic Materials

2.2.1 Displacement field representation

The behavior of periodic materials is described by analyzing a single-unit cell subjected to periodic boundary conditions (PBC), and typically, such problems are addressed through asymptotic homogenization theory (Bensoussan et al., 1978). It is worth noting that periodic solutions have been successfully developed by employing the Fourier series expansion method for periodic mechanical fields with various unit cell architectures, as demonstrated by Nemat-Nasser and Taya (1981), Nemat-Nasser et al. (1982), Díaz et al. (2001), Rodríguez-Ramos et al. (2001) and more recently by Ramírez-Torres et al. (2019) and Lages and Marques (2020).

To improve the representation of the displacement field in the q th subvolume, the simplest homogenization approach introduced by Bensoussan et al. (1978) employs a two-scale expansion. This representation incorporates both global (\mathbf{x}) and local (\mathbf{y}) coordinates, considering macroscopic and microstructure-induced fluctuating components expressed as:

$$u_i^{(q)}(\mathbf{x}, \mathbf{y}) = \bar{\varepsilon}_{ij} x_j + u_i'^{(q)}(\mathbf{y}), \quad (1)$$

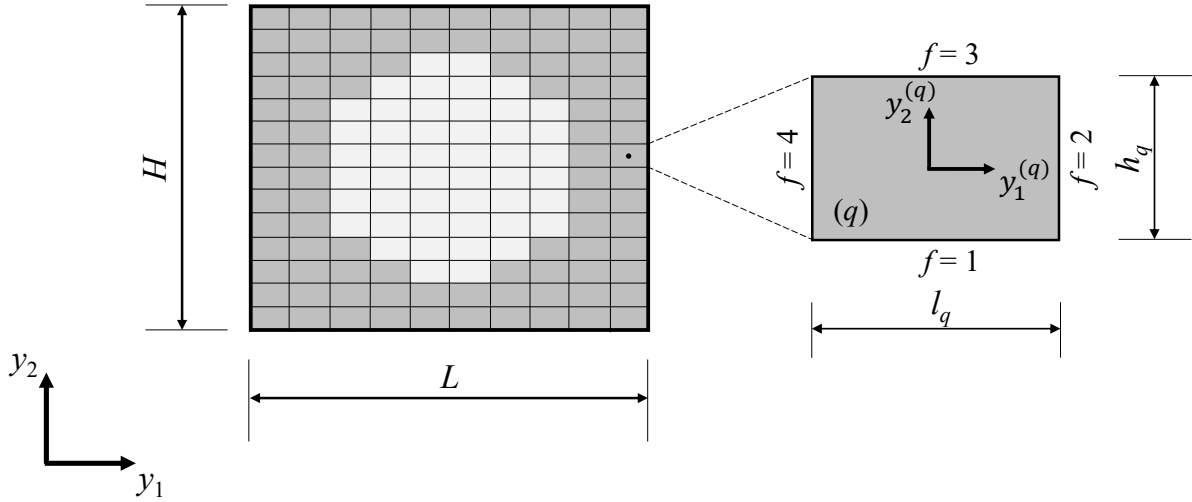
where $u_i'^{(q)}(\mathbf{y})$ denote fluctuating displacement components induced by the heterogeneous microstructure and $\bar{\varepsilon}_{ij}$ are the specified macroscopic (volume-averaged) strains applied to the entire material. Note that the subscripts are denoted as $i, j = 1, 2$ for two-dimensional analysis.

For two-dimensional problems in Cartesian coordinates, a rectangular domain within the $y_1 - y_2$ plane of analysis is employed, spanning the region $0 \leq y_1 \leq L$ and $0 \leq y_2 \leq H$ as shown in Figure 3. Inside this domain are subvolumes with dimensions l_q and h_q along the $y_1^{(q)}$ and $y_2^{(q)}$ axes, respectively. These subvolumes may contain different elastic materials with uniform values inside them. In the present zeroth-order or standard finite-volume theory formulation, only displacements are unknown quantities (Cavalcante; Pindera, 2012a). In this case, the components of the fluctuating displacements field in the local coordinates system are approximated by the second-order Legendre polynomial as follows:

$$\begin{aligned} u_i'^{(q)} = & W_{i(00)}^{(q)} + y_1^{(q)} W_{i(10)}^{(q)} + y_2^{(q)} W_{i(01)}^{(q)} + \frac{1}{2} \left[3 \left(y_1^{(q)} \right)^2 - \frac{l_q^2}{4} \right] W_{i(20)}^{(q)} + \\ & + \frac{1}{2} \left[3 \left(y_2^{(q)} \right)^2 - \frac{h_q^2}{4} \right] W_{i(02)}^{(q)}, \end{aligned} \quad (2)$$

with $W_{i(mn)}^{(q)}$ being unknown displacement field coefficients.

Figure 3 – The representation of discretized analysis domain and local coordinate system of a generic subvolume (q)



Font: Author (2024).

2.2.2 Local stiffness matrix calculation

The finite-volume theory employs the volume average of the different fields that define the material behavior and imposes boundary and continuity conditions between adjacent subvolumes in an average sense, aiming to satisfy the equilibrium equations. Following Cavalcante et al. (2012), the surface-averaged fluctuating displacement components at the subvolume faces $\hat{u}_i'^{(q,f)}$ can be evaluated as:

$$\begin{aligned}\hat{u}_i'^{(q,f=1,3)} &= \frac{1}{l_q} \int_{-\frac{l_q}{2}}^{\frac{l_q}{2}} u_i'^{(q)} \left(y_1^{(q)}, \mp \frac{h_q}{2} \right) dy_1^{(q)} = W_{i(00)}^{(q)} \mp \frac{h_q}{2} W_{i(01)}^{(q)} + \frac{h_q^2}{4} W_{i(02)}^{(q)}, \\ \hat{u}_i'^{(q,f=2,4)} &= \frac{1}{h_q} \int_{-\frac{h_q}{2}}^{\frac{h_q}{2}} u_i'^{(q)} \left(\pm \frac{l_q}{2}, y_2^{(q)} \right) dy_2^{(q)} = W_{i(00)}^{(q)} \pm \frac{l_q}{2} W_{i(10)}^{(q)} + \frac{l_q^2}{4} W_{i(20)}^{(q)}.\end{aligned}\quad (3)$$

Employing the components of the displacement field from Eq. (2) in Eq. (3), eight expressions are obtained for the surface-averaged fluctuating displacements as a function of the displacement field coefficients. These expressions can be represented in matrix notation as follows:

$$\hat{\mathbf{u}}'^{(q)} = \mathbf{A}^{(q)} \mathbf{W}^{(q)} + \mathbf{a}^{(q)} \mathbf{W}_{00}^{(q)}, \quad (4)$$

where $\hat{\mathbf{u}}'^{(q)} = \left\{ \hat{u}_1'^{(q,1)}, \hat{u}_2'^{(q,1)}, \hat{u}_1'^{(q,2)}, \hat{u}_2'^{(q,2)}, \hat{u}_1'^{(q,3)}, \hat{u}_2'^{(q,3)}, \hat{u}_1'^{(q,4)}, \hat{u}_2'^{(q,4)} \right\}^T$ is the surface-averaged fluctuating displacement vector, $\mathbf{W}^{(q)} = \left\{ W_{1(10)}^{(q)}, W_{1(01)}^{(q)}, W_{1(20)}^{(q)}, W_{1(02)}^{(q)}, \dots, W_{2(02)}^{(q)} \right\}^T$ is the vector containing the first and second-order unknown coefficients and $\mathbf{W}_{00}^{(q)} = \left\{ W_{1(00)}^{(q)}, W_{2(00)}^{(q)} \right\}^T$ is the vector containing the zeroth-order unknown coefficients, and the matrices $\mathbf{A}^{(q)}$ and $\mathbf{a}^{(q)}$ are

defined as follows:

$$\mathbf{A}^{(q)} = \begin{bmatrix} 0 & -\frac{1}{2}h_q & 0 & \frac{1}{4}h_q^2 & 0 & 0 & 0 & 0 \\ 0 & 0 & 0 & 0 & 0 & -\frac{1}{2}h_q & 0 & \frac{1}{4}h_q^2 \\ \frac{1}{2}l_q & 0 & \frac{1}{4}l_q^2 & 0 & 0 & 0 & 0 & 0 \\ 0 & 0 & 0 & 0 & \frac{1}{2}l_q & 0 & \frac{1}{4}l_q^2 & 0 \\ 0 & \frac{1}{2}h_q & 0 & \frac{1}{4}h_q^2 & 0 & 0 & 0 & 0 \\ 0 & 0 & 0 & 0 & 0 & \frac{1}{2}h_q & 0 & \frac{1}{4}h_q^2 \\ -\frac{1}{2}l_q & 0 & \frac{1}{4}l_q^2 & 0 & 0 & 0 & 0 & 0 \\ 0 & 0 & 0 & 0 & -\frac{1}{2}l_q & 0 & \frac{1}{4}l_q^2 & 0 \end{bmatrix} \quad \text{and} \quad \mathbf{a}^{(q)} = \begin{bmatrix} 1 & 0 \\ 0 & 1 \\ 1 & 0 \\ 0 & 1 \\ 1 & 0 \\ 0 & 1 \\ 1 & 0 \\ 0 & 1 \end{bmatrix}. \quad (5)$$

According to Cavalcante et al. (2012), the surface-averaged strains are determined based on the unknown coefficients of the fluctuating displacement field and the macroscopic strains, which are then expressed explicitly in terms of the macroscopic strains and the surface-averaged fluctuating displacement components upon the use of the definitions given in Eq. (3). Moreover, the surface-averaged traction components at the subvolume faces $\hat{t}_i^{(q,f)}$ are similarly expressed in terms of stresses via Cauchy's relations as follows:

$$\begin{aligned} \hat{t}_i^{(q,f=1,3)} &= \mp \frac{1}{l_q} \int_{-\frac{l_q}{2}}^{\frac{l_q}{2}} \sigma_{2i}^{(q,f)} \left(y_1^{(q)}, \mp \frac{h_q}{2} \right) dy_1^{(q)}, \\ \hat{t}_i^{(q,f=2,4)} &= \pm \frac{1}{h_q} \int_{-\frac{h_q}{2}}^{\frac{h_q}{2}} \sigma_{1i}^{(q,f)} \left(\pm \frac{l_q}{2}, y_2^{(q)} \right) dy_2^{(q)}. \end{aligned} \quad (6)$$

The application of the following equilibrium equations in the absence of body forces at the subvolume level

$$\int_S \mathbf{t}^{(q)} dS = \sum_{f=1}^4 \int_{L_f} \mathbf{t}^{(q,f)} dL_f = \sum_{f=1}^4 L_f \hat{\mathbf{t}}^{(q,f)} = \mathbf{0}, \quad (7)$$

where $L_1^{(q)} = l_q$, $L_2^{(q)} = h_q$, $L_3^{(q)} = l_q$ and $L_4^{(q)} = h_q$, leads to the relationship between the surface-averaged tractions and surface-averaged fluctuating displacements given in terms of the local stiffness matrix $\mathbf{K}^{(q)}$ for the q th subvolume:

$$\hat{\mathbf{t}}^{(q)} = \mathbf{N}^{(q)} \mathbf{C}^{(q)} \bar{\boldsymbol{\varepsilon}} + \mathbf{K}^{(q)} \hat{\mathbf{u}}'^{(q)}, \quad (8)$$

where $\hat{\mathbf{t}}^{(q)} = \left\{ \hat{t}_1^{(q,1)}, \hat{t}_2^{(q,1)}, \hat{t}_1^{(q,2)}, \hat{t}_2^{(q,2)}, \hat{t}_1^{(q,3)}, \hat{t}_2^{(q,3)}, \hat{t}_1^{(q,4)}, \hat{t}_2^{(q,4)} \right\}^T$ is the surface-averaged traction vector, $\mathbf{N}^{(q)}$ and $\mathbf{C}^{(q)}$ are the matrices containing components of normal vector at the subvolume faces and material constitutive matrix, respectively, and $\bar{\boldsymbol{\varepsilon}}$ denotes the macroscopic strain. In the Cartesian coordinate system, the matrix $\mathbf{N}^{(q)}$ remains constant across all subvolumes within the analysis domain. The local stiffness matrix is given by $\mathbf{K}^{(q)} = \mathbf{B}^{(q)} \bar{\mathbf{A}}^{(q)}$, where the matrix $\mathbf{B}^{(q)}$

depends of on constitutive matrix components and the subvolume face dimensions as follows:

$$\mathbf{B}^{(q)} = \begin{bmatrix} 0 & -C_{33} & 0 & \frac{3}{2}C_{33}h_q & -C_{33} & 0 & 0 & 0 \\ -C_{12} & 0 & 0 & 0 & 0 & -C_{22} & 0 & \frac{3}{2}C_{22}h_q \\ C_{11} & 0 & \frac{3}{2}C_{11}l_q & 0 & 0 & C_{12} & 0 & 0 \\ 0 & C_{33} & 0 & 0 & C_{33} & 0 & \frac{3}{2}C_{33}l_q & 0 \\ 0 & C_{33} & 0 & \frac{3}{2}C_{33}h_q & C_{33} & 0 & 0 & 0 \\ C_{12} & 0 & 0 & 0 & 0 & C_{22} & 0 & \frac{3}{2}C_{22}h_q \\ -C_{11} & 0 & \frac{3}{2}C_{11}l_q & 0 & 0 & -C_{12} & 0 & 0 \\ 0 & -C_{33} & 0 & 0 & -C_{33} & 0 & \frac{3}{2}C_{33}l_q & 0 \end{bmatrix}, \quad (9)$$

where the matrix $\bar{\mathbf{A}}^{(q)} = \left(\mathbf{A}^{(q)}\right)^{-1} - \left(\mathbf{A}^{(q)}\right)^{-1} \mathbf{a}^{(q)} \bar{\mathbf{a}}^{(q)}$,

with $\bar{\mathbf{a}}^{(q)} = \left[\sum_{f=1}^4 \left(\mathbf{B}^{(q,f)} L_f^{(q)}\right) \left(\mathbf{A}^{(q)}\right)^{-1} \mathbf{a}^{(q)} \right]^{-1} \sum_{f=1}^4 \left(\mathbf{B}^{(q,f)} L_f^{(q)}\right) \left(\mathbf{A}^{(q)}\right)^{-1}$. It is worth adding that the local stiffness matrix is non-symmetric (pseudo stiffness matrix), which increases the computational cost of the topology optimization process. On the other hand, evaluating in terms of energetically conjugated quantities (force and displacement) at the subvolume level, Eq. (8) becomes,

$$\mathbf{R}^{(q)} = \hat{\mathbf{H}}^{(q)} \bar{\boldsymbol{\varepsilon}} + \hat{\mathbf{K}}^{(q)} \hat{\mathbf{u}}'^{(q)}, \quad (10)$$

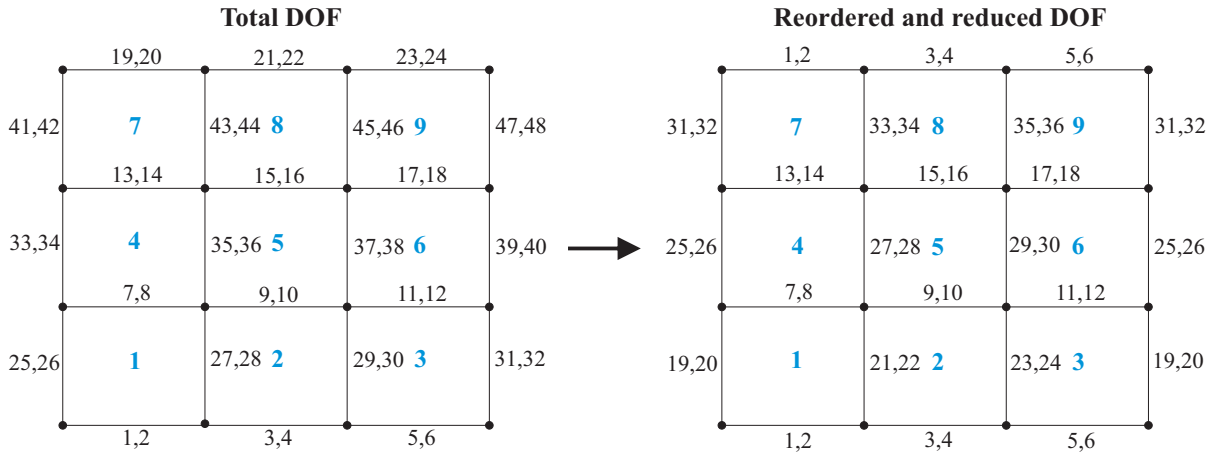
where $\mathbf{R}^{(q)} = \hat{\mathbf{L}}^{(q)} \hat{\mathbf{t}}^{(q)}$ is the resultant of forces acting at the faces of the subvolume q , $\hat{\mathbf{H}}^{(q)} = \hat{\mathbf{L}}^{(q)} \mathbf{N}^{(q)} \mathbf{C}^{(q)}$ corresponds to the macroscopic load at subvolume level due to the application of macroscopic strain, $\hat{\mathbf{K}}^{(q)} = \hat{\mathbf{L}}^{(q)} \mathbf{K}^{(q)}$ is a modified local stiffness matrix (symmetric), and $\hat{\mathbf{L}}^{(q)}$ is the matrix containing the subvolume face dimensions expressed as:

$$\hat{\mathbf{L}}^{(q)} = \begin{bmatrix} \mathbf{L}_{(1)}^{(q)} & \mathbf{0} & \mathbf{0} & \mathbf{0} \\ \mathbf{0} & \mathbf{L}_{(2)}^{(q)} & \mathbf{0} & \mathbf{0} \\ \mathbf{0} & \mathbf{0} & \mathbf{L}_{(3)}^{(q)} & \mathbf{0} \\ \mathbf{0} & \mathbf{0} & \mathbf{0} & \mathbf{L}_{(4)}^{(q)} \end{bmatrix}, \quad \text{for } \mathbf{L}_{(f)}^{(q)} = \begin{bmatrix} L_{(f)}^{(q)} & 0 \\ 0 & L_{(f)}^{(q)} \end{bmatrix}. \quad (11)$$

2.2.3 Global stiffness matrix assembly

The assembling of a global system of equations in the context of the finite-volume theory employing energetically conjugated quantities results in a global symmetric stiffness matrix, particularly in the case of meshes with rectangular subvolumes. This accelerates the solution of the global system of equations through efficiently implemented computational tools. If the domain is subdivided in $N_q = N_x N_y$ subvolumes, considering two degrees of freedom (DOF) per face, $\text{ndof} = 2N_x(N_y + 1) + 2N_y(N_x + 1)$ corresponds to the total number of degrees of freedom for the discretized model, being N_x and N_y the number of subvolumes in horizontal and vertical directions, respectively. Additionally, as shown in Figure 4, the imposition of PBC reduces the overall degrees of freedom, resulting in computational savings. The imposition of PBC for this coarse mesh discretization reduces the total number of degrees of freedom from 48 to 36.

Figure 4 – Enforcing PBC to an RUC which leads to the elimination of redundant degrees of freedom



Font: Author (2024).

Based on the kinematic and static compatibility conditions, the expression that evaluates the global system of equations can be written considering energetically conjugated quantities (force and displacement) as follows:

$$\sum_{q=1}^{N_q} \mathbf{Q}^{(q)T} \mathbf{R}^{(q)} = \sum_{q=1}^{N_q} \mathbf{Q}^{(q)T} \hat{\mathbf{H}}^{(q)} \bar{\boldsymbol{\varepsilon}} + \sum_{q=1}^{N_q} \mathbf{Q}^{(q)T} \hat{\mathbf{K}}^{(q)} \mathbf{Q}^{(q)} \hat{\mathbf{u}}' = \mathbf{0}, \quad (12)$$

$\mathbf{Q}^{(q)T}$ and $\mathbf{Q}^{(q)}$ are the static and kinematic compatibility matrices of the structure, respectively. Evaluating the resultant of forces, the term on the left-hand side of the Eq. (12) vanishes due to the anti-periodicity of total surface-averaged tractions. Then, the system of equations can be rewritten as:

$$\hat{\mathbf{K}} \hat{\mathbf{u}}' = \hat{\mathbf{F}}, \quad (13)$$

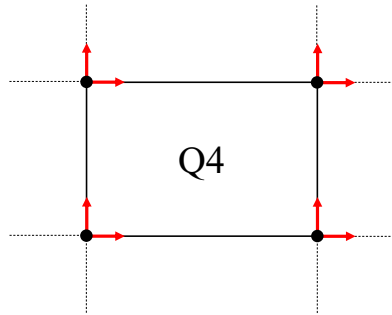
where $\hat{\mathbf{K}} = \sum_{q=1}^{N_q} \mathbf{Q}^{(q)T} \hat{\mathbf{K}}^{(q)} \mathbf{Q}^{(q)}$ is the global stiffness matrix, $\hat{\mathbf{u}}'$ represents the global surface-averaged fluctuating displacement vector, and $\hat{\mathbf{F}} = - \sum_{q=1}^{N_q} \mathbf{Q}^{(q)T} \hat{\mathbf{H}}^{(q)} \bar{\boldsymbol{\varepsilon}}$ is the global load vector due to the heterogeneity and the macroscopic strain. This global load vector depends on the differences in the material stiffness matrices of adjacent subvolumes and vanishes if the analyzed model consists of homogeneous material.

2.2.4 Order of magnitude of the problem

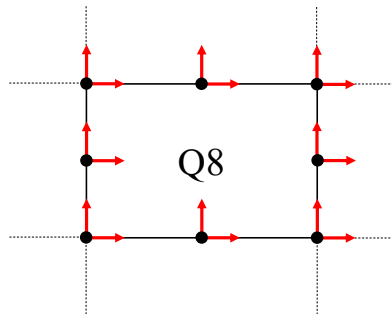
The average contributions, measured in terms of degrees of freedom, for quadrilateral finite elements (Q4 and Q8) or subvolumes (in the case of FVT) at the mesh center are evaluated from the analysis shown in Figure 5. Quadrilateral finite elements contribute with 2 (Q4) and 6 (Q8) degrees of freedom for the global system of equations. In comparison, in the finite-volume theory, the subvolumes located in the middle of the mesh contribute with 4 degrees of freedom for the global system of equations, being in an intermediary position between the Q4 and Q8 finite

elements in terms of the size of the global system of equations, which defines the computational cost of the numerical solution per iteration.

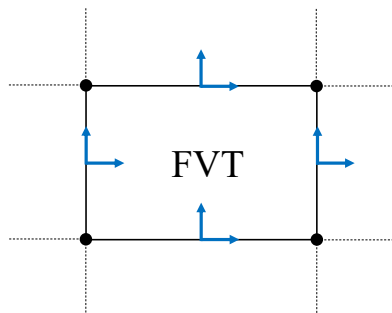
Figure 5 – Average number of degrees of freedom



8 degrees of freedom shared
by 4 elements
=
2 degrees of freedom per element
in the global system of equations



8 degrees of freedom shared
by 4 elements and 8 degrees of freedom shared
by 2 elements
=
6 degrees of freedom per element
in the global system of equations



8 degrees of freedom shared
by 2 subvolumes
=
4 degrees of freedom per subvolume
in the global system of equations

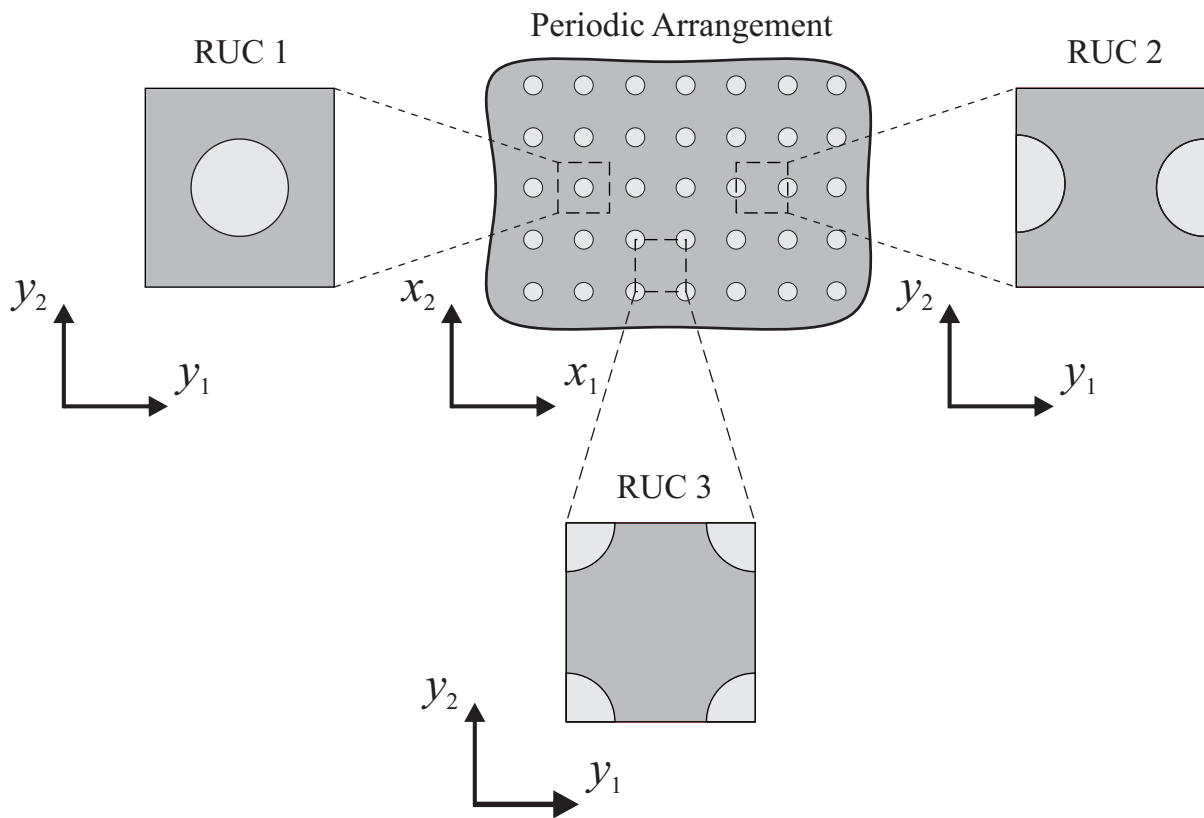
Font: Adapted from Cavalcante (2006).

3 NUMERICAL HOMOGENIZATION

3.1 Fundamental Concepts

Micromechanical analyses of composite materials involve two fundamental concepts: (i) the representative volume element (RVE) and (ii) the repeating unit cell (RUC). These concepts are based on different geometric representations of heterogeneous microstructures and require distinct boundary conditions. The aim is to analyze the smallest material subvolume whose response is indistinguishable from that of the material-at-large (Drago; Pindera, 2007; Pindera et al., 2009; Aboudi et al., 2012).

Figure 6 – Microstructural periodic arrangement with three different squares representative unit cells



Font: Author (2024).

The RVE is typically defined as a volume large enough to represent the heterogeneous material statistically. It is a volume where averaging results in sufficiently accurate effective properties. On the other hand, the RUC involves fewer inhomogeneities, sometimes just one, that are replicated to generate the periodically repeating material microstructure. Both representative volume patterns simplify the analysis but require solutions to boundary value problems with different boundary conditions. The conditions for the representative volume element involve either homogeneous displacement or homogeneous traction. Conversely, the repeating unit cell requires periodic boundary conditions. The primary focus of this study lies in materials

exhibiting periodic microstructures. Figure 6 shows three different squares RUCs representing the same microstructural periodic arrangement. Although it displays distinct unit cells, the various representations produce similar results for the macroscopic or effective properties of the homogenized material. In other words, regardless of the specific geometric choices at the microstructural level, the behavior of the resulting material at a macroscopic scale remains the same.

3.2 Linear Elasticity

This work is limited to linear elastic material under the infinitesimal deformation assumption. In the case of a typical RUC, the kinematically admissible strain field ε_{ij} is related to a respective displacement field u_i through the relation described below:

$$\varepsilon_{ij} = \frac{1}{2} \left(\frac{\partial u_i}{\partial y_j} + \frac{\partial u_j}{\partial y_i} \right). \quad (14)$$

In the absence of body forces, the statically admissible stress field σ_{ij} satisfies the equilibrium equation given by:

$$\frac{\partial \sigma_{ij}}{\partial y_j} = 0. \quad (15)$$

In the most general case, the stress and strain fields are then related by Hooke's law as follows:

$$\sigma_{ij} = C_{ijkl} \varepsilon_{kl}, \quad (16)$$

where C_{ijkl} corresponds to the four-order elastic material constitutive tensor. This constitutive tensor consists of 81 components in its most general form (Qu; Cherkaoui, 2006). However, due to the symmetry of stress and strain, the number of independent components is reduced to 36. Besides, for hyperelastic materials where a strain energy potential governs the elastic material response leads to $C_{ijkl} = C_{klij}$. Then, the number of independent components of the constitutive matrix is further reduced to 21, and can be expressed in Voigt notation as a symmetric matrix represented by:

$$\mathbf{C} = \begin{bmatrix} C_{1111} & C_{1122} & C_{1133} & C_{1123} & C_{1113} & C_{1112} \\ & C_{2222} & C_{2233} & C_{2223} & C_{2213} & C_{2212} \\ & & C_{3333} & C_{3323} & C_{3313} & C_{3312} \\ & & & C_{2323} & C_{2313} & C_{2312} \\ & & & & C_{1313} & C_{1312} \\ \text{sym.} & & & & & C_{1212} \end{bmatrix}. \quad (17)$$

In the particular case of plane stress state with all stress components in the out-of-plane direction (3-direction) being zero, and to facilitate the computational implementation, the indices can be compressed as $11 \rightarrow 1$, $22 \rightarrow 2$, and $12 \rightarrow 3$, allowing to write the constitutive matrix for orthotropic materials as:

$$\mathbf{C} = \begin{bmatrix} C_{11} & C_{12} & 0 \\ & C_{22} & 0 \\ \text{sym.} & & C_{33} \end{bmatrix}, \quad (18)$$

and for isotropic materials as:

$$\mathbf{C} = \frac{E}{1-\nu^2} \begin{bmatrix} 1 & \nu & 0 \\ & 1 & 0 \\ \text{sym.} & & \frac{1-\nu}{2} \end{bmatrix}, \quad (19)$$

where E and ν correspond to the Young's modulus and Poisson's ratio, respectively.

3.3 Average-strain Theorem

The development of the theorems in this section depends on the definition of average strain on the domain V with boundary surface S (Figure 7). The conventional approach involves evaluating the macroscopic quantities by averaging their microscopic counterparts over the representative volume element, as outlined by Hill (1963) and evaluated as follows:

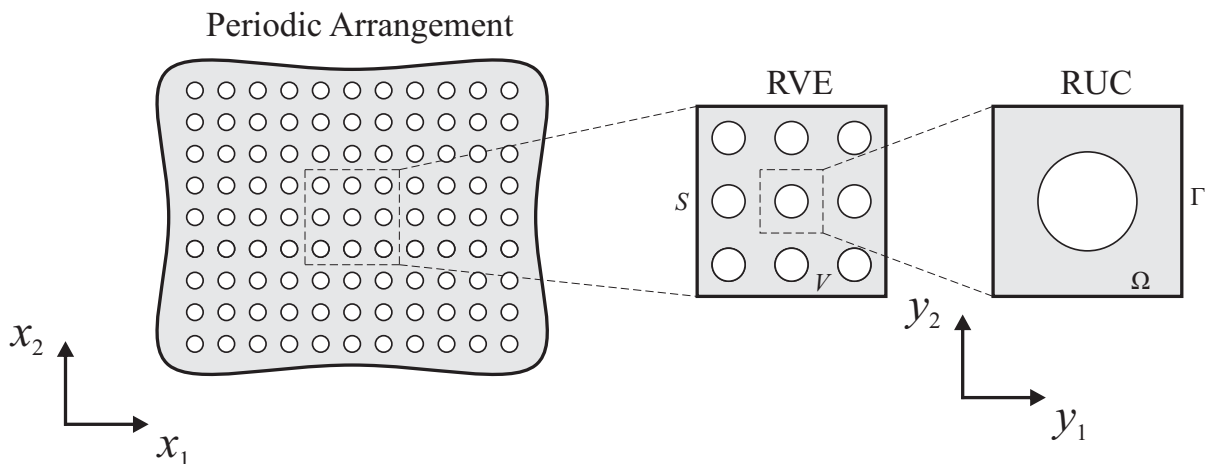
$$\begin{aligned} \bar{\varepsilon}_{ij} &= \frac{1}{V} \int_V \varepsilon_{ij} dV = \frac{1}{2V} \int_V \left(\frac{\partial u_i}{\partial x_j} + \frac{\partial u_j}{\partial x_i} \right) dV \\ &= \frac{1}{2V} \int_V \frac{\partial u_i}{\partial x_j} dV + \frac{1}{2V} \int_V \frac{\partial u_j}{\partial x_i} dV, \end{aligned} \quad (20)$$

and by application of the divergence theorem,

$$\bar{\varepsilon}_{ij} = \frac{1}{2V} \int_S u_i n_j dS + \frac{1}{2V} \int_S u_j n_i dS, \quad (21)$$

where the overbar stands for the volume average.

Figure 7 – RVE and RUC of a periodic composite material



Font: Author (2024).

Consider a representative volume element (RVE) of a periodic composite material shown in Figure 7, with volume V and boundary surface S with outward normal vector n_j , subject to the *homogenous displacement boundary conditions* $u_i(S) = \varepsilon_{ij}^0 x_j$, for $x_j \in S$, where ε_{ij}^0 is a uniform symmetry strain tensor. Substituting this boundary condition into Eq. (21),

$$\bar{\varepsilon}_{ij} = \frac{1}{2V} \int_S \varepsilon_{ik}^0 x_k n_j dS + \frac{1}{2V} \int_S \varepsilon_{jk}^0 x_k n_i dS. \quad (22)$$

Applying the divergence theorem in Eq. (22) and considering the symmetry of the strain tensor, the average strain tensor of the RVE is given by:

$$\bar{\varepsilon}_{ij} = \frac{1}{2V} \int_V \varepsilon_{ik}^0 \frac{\partial x_k}{\partial x_j} dV + \frac{1}{2V} \int_V \varepsilon_{jk}^0 \frac{\partial x_k}{\partial x_i} dV = \frac{1}{2} (\varepsilon_{ij}^0 + \varepsilon_{ji}^0) = \varepsilon_{ij}^0. \quad (23)$$

The average strain tensor on the domain V is equal to the applied uniform strain tensor on the RVE boundary surface S , independently of the material microstructure.

3.3.1 Periodicity conditions and the average-strain

Assume that at each point on the surface boundary Γ of an RUC defined by the domain Ω , the strain field ε_{ij} is represented in two scales through the relation $\varepsilon_{ij} = \varepsilon_{ij}^0 + \varepsilon'_{ij}$, being ε_{ij}^0 the uniform strain and ε'_{ij} the periodic or fluctuating strain due to the heterogeneous microstructure. Making use of the average-strain theorem, the average strain tensor taken over the RUC is given by:

$$\bar{\varepsilon}_{ij}^{(\Omega)} = \varepsilon_{ij}^0 + \frac{1}{2\Omega} \int_{\Omega} \frac{\partial u'_i}{\partial y_j} d\Omega + \frac{1}{2\Omega} \int_{\Omega} \frac{\partial u'_j}{\partial y_i} d\Omega. \quad (24)$$

Applying the divergence theorem in the second and third terms on the right side of Eq. (24), and making use of the periodicity of fluctuating displacements on the boundary Γ ,

$$\bar{\varepsilon}_{ij}^{(\Omega)} = \varepsilon_{ij}^0 + \frac{1}{2\Omega} \int_{\Gamma} u'_i n_j d\Gamma + \frac{1}{2\Omega} \int_{\Gamma} u'_j n_i d\Gamma = \varepsilon_{ij}^0. \quad (25)$$

The average strain tensor on the RUC is also equal to the uniform strain tensor of the *homogeneous boundary condition* applied on the outer surface of the RVE. Note that the homogenization problem can be solved considering that the response of the entire RVE under the above *homogeneous displacement boundary conditions* is identical to the response of an arbitrary RUC under appropriate PBC, representing a considerable simplification of the problem. This conclusion was also demonstrated by Escarpini Filho and Marques (2014) in the context of the thermal homogenization problem.

3.4 Effective Properties of Periodic Materials

Nemat-Nasser and Taya (1981) and Nemat-Nasser et al. (1982) introduced a theoretically rigorous method for predicting the effective properties of periodic composite materials using the Fourier expansion of the strain field to derive an integral equilibrium equation. However, when dealing with complex microstructure, the analytical determination of material behavior becomes impractical, and a numerical method must be employed. In this context, several numerical approaches have been developed to evaluate effective properties of periodic materials, e.g., Guedes and Kikuchi (1990) with the finite element method and Bansal and Pindera (2006) with the finite-volume theory, among others.

This work shows two equivalent paths for evaluating effective elastic properties of two-dimensional cellular materials based on asymptotic homogenization theory: a strain energy-based

approach, through the satisfaction of the Hill-Mandel condition (Qu; Cherkaoui, 2006), which directly relates the strain energy in the heterogeneous microstructure with the strain energy in the equivalent or homogenized material, and the other through the principles of micromechanics mean-field theory.

3.4.1 Strain energy-based approach

In this approach, homogenization can be interpreted as finding a homogeneous material energetically equivalent to a given material with a heterogeneous microstructure. Considering the zeroth-order formulation of the finite-volume theory, Araujo et al. (2021) demonstrated the equivalence between the structural strain energy (U) and the work done by external forces (W), once the differential equilibrium equations are satisfied point-wise inside the subvolumes. Based on this observation and using the strain energy density definition ($\bar{U} = U/\Omega$),

$$\bar{U} = \frac{1}{\Omega} \sum_{q=1}^{N_q} W^{(q)} = \frac{1}{\Omega} \sum_{q=1}^{N_q} \frac{1}{2} \mathbf{R}^{(q)T} \hat{\mathbf{u}}^{(q)} = \frac{1}{\Omega} \sum_{q=1}^{N_q} \frac{1}{2} \hat{\mathbf{u}}^{(q)T} \hat{\mathbf{K}}^{(q)} \hat{\mathbf{u}}^{(q)}, \quad (26)$$

where $\hat{\mathbf{u}}^{(q)}$ corresponds to the total surface-averaged displacement field (macroscopic + fluctuating) of the subvolume q . Making use of the micro-macro Hill's energy equivalence,

$$\begin{aligned} \frac{1}{2} \bar{\boldsymbol{\sigma}}^T \bar{\boldsymbol{\varepsilon}} &= \frac{1}{2\Omega} \int_{\Omega} \boldsymbol{\sigma}^T \boldsymbol{\varepsilon} d\Omega = \frac{1}{\Omega} \sum_{q=1}^{N_q} \frac{1}{2} \hat{\mathbf{u}}^{(q)T} \hat{\mathbf{K}}^{(q)} \hat{\mathbf{u}}^{(q)}, \\ \bar{\boldsymbol{\varepsilon}}^T \mathbf{C}^* \bar{\boldsymbol{\varepsilon}} &= \frac{1}{\Omega} \sum_{q=1}^{N_q} \hat{\mathbf{u}}^{(q)T} \hat{\mathbf{K}}^{(q)} \hat{\mathbf{u}}^{(q)}. \end{aligned} \quad (27)$$

Calculating the total surface-averaged displacement vectors involves combining different cases of macroscopic strains. This method is based on Maxwell-Betti's reciprocal work theorem, where for linear elastic analysis, the work done by the macroscopic stress associated with the macroscopic strain case (i) through the macroscopic strain case (j) is equal to the work done by the macroscopic stress related to the macroscopic strain case (j) through the macroscopic strain case (i). This way, for determining the components of the effective constitutive matrix \mathbf{C}^* , it is necessary previously to apply linearly independent cases of unit macroscopic strain to calculate the corresponding total surface-averaged displacements. In the plane stress state, the independent macroscopic strains can be $\bar{\boldsymbol{\varepsilon}}|_{(1)} = \{1, 0, 0\}^T$, $\bar{\boldsymbol{\varepsilon}}|_{(2)} = \{0, 1, 0\}^T$ and $\bar{\boldsymbol{\varepsilon}}|_{(3)} = \{0, 0, 1\}^T$, that involve two cases of normal strains, occurring in orthogonal directions, and a pure shear strain, respectively. Therefore, the effective constitutive matrix components are evaluated as follows:

$$C_{ij}^* = \frac{1}{\Omega} \sum_{q=1}^{N_q} \hat{\mathbf{u}}^{(q)T}|_{(i)} \hat{\mathbf{K}}^{(q)} \hat{\mathbf{u}}^{(q)}|_{(j)}, \quad (28)$$

with $i, j = 1, 2, 3$ and $\hat{\mathbf{u}}^{(q)}|_{(i)}$ representing the total surface-averaged displacement field for the q th subvolume, due to the application of macroscopic strain case (i).

3.4.2 Mean-field theory approach

Mean-field theory or average-field theory operates on the principle that the effective mechanical properties observed in experiments result from the relationship between the volume-averaged strain and stress of microscopically heterogeneous specimens. Consequently, macro-fields are defined as the volume averages of their corresponding micro-fields, and effective properties are established as the relationships between these averaged micro-fields (Hori; Nemat-Nasser, 1999).

According to Cavalcante et al. (2012), the crucial problem in the micromechanics of heterogeneous materials is the determination of localization relations for the subdomains into which the smallest domain representative of the material's response is subdivided for analysis purposes. For a linear elastic analysis, the localization relation is given by:

$$\bar{\boldsymbol{\varepsilon}}^{(q)} = \mathbb{A}^{(q)} \bar{\boldsymbol{\varepsilon}}, \quad (29)$$

where \mathbb{A} is the elastic strain concentration tensor calculated just once for every q th subdomain (Hill, 1963). Specifically, each column of $\mathbb{A}^{(q)}$ is obtained by applying one nonzero macroscopic strain case $\bar{\boldsymbol{\varepsilon}}|_{(\cdot)}$ at a time, and solving Eq. (29) to generate the corresponding q th subvolume-averaged strain $\bar{\boldsymbol{\varepsilon}}^{(q)}$.

In order to determine the volume-averaged stress ($\bar{\boldsymbol{\sigma}}$) within the unit cell domain (Ω) based on the subvolume stresses ($\boldsymbol{\sigma}^{(q)}$), consider the following expression:

$$\bar{\boldsymbol{\sigma}} = \frac{1}{\Omega} \int_{\Omega} \boldsymbol{\sigma} d\Omega = \frac{1}{\Omega} \sum_{q=1}^{N_q} \int_{\Omega_q} \boldsymbol{\sigma}^{(q)} d\Omega_q = \sum_{q=1}^{N_q} c^{(q)} \bar{\boldsymbol{\sigma}}^{(q)}, \quad (30)$$

where $c^{(q)}$ is the volume fraction of the subvolume q . Employing the homogenized Hooke's law for the material-at-large ($\bar{\boldsymbol{\sigma}} = \mathbf{C}^* \bar{\boldsymbol{\varepsilon}}$) and for the local subvolume ($\bar{\boldsymbol{\sigma}}^{(q)} = \mathbf{C}^{(q)} \bar{\boldsymbol{\varepsilon}}^{(q)}$), the effective constitutive matrix can be evaluated as:

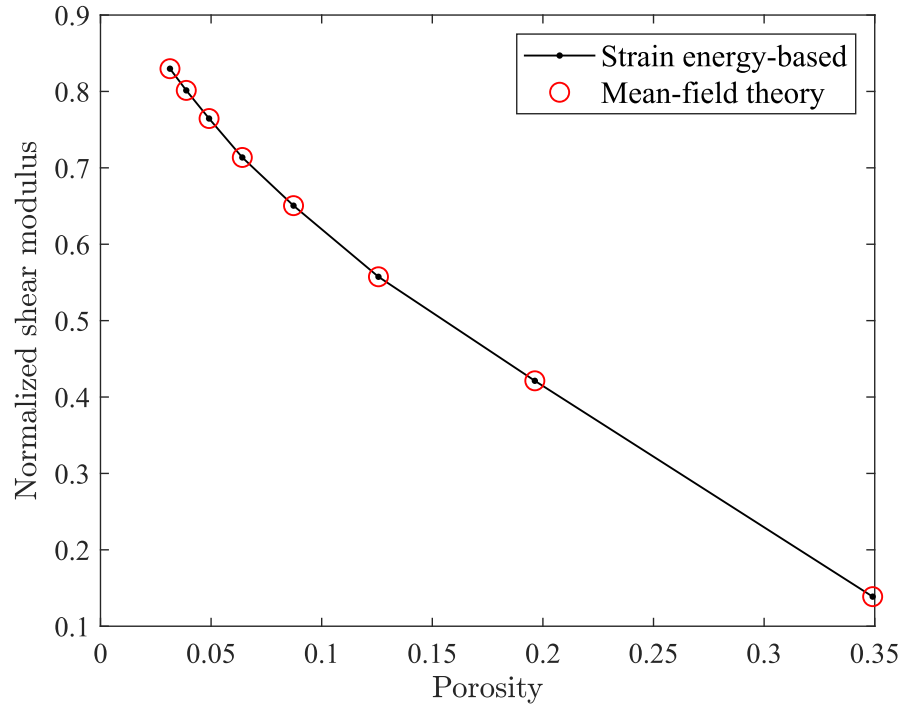
$$\mathbf{C}^* = \sum_{q=1}^{N_q} c^{(q)} \mathbf{C}^{(q)} \mathbb{A}^{(q)}. \quad (31)$$

The application of Eqs. (28) and (31) leads to the same effective elastic properties of the material, differing only in the calculation method. Sensitivity equations are necessary for the density-based topology optimization procedure, and the complexities of the referred equations above will be presented in Section 4.2.

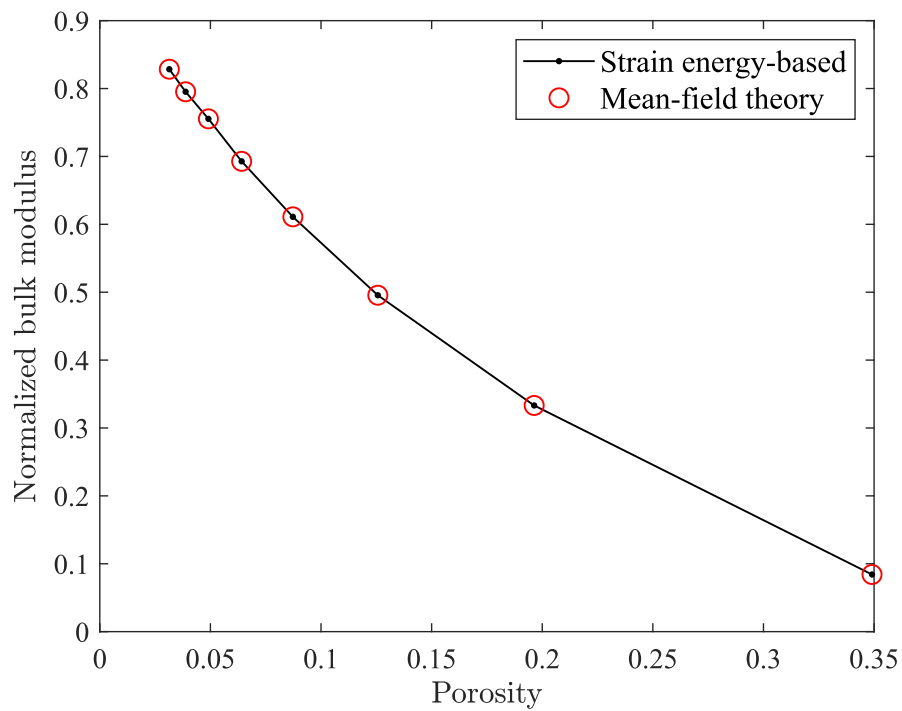
To verify the algorithm's implementation for computing the effective elastic moduli by the strain energy-based and mean-field theory approaches, a perforated square aluminum sheet with Young's modulus of $E = 68.95$ GPa and a Poisson's ratio of $\nu = 0.30$ is examined assuming various porosities levels. The analysis is realized considering the plane stress state and employing a repeating unit cell, as shown in Figure 7. As theoretically expected, the results illustrated in Figures 8 demonstrate that the strain energy-based and the mean-field theory approaches yield

identical numerical values for a porous material's effective elastic moduli for different porosity levels.

Figure 8 – Effective elastic moduli estimated by different approaches



(a) Shear modulus



(b) Bulk modulus

Font: Author (2024).

4 TOPOLOGY OPTIMIZATION

Topology optimization (TO) is an iterative design process that optimizes a material distribution in a given design domain considering a specified objective function and a set of constraints (Andreassen et al., 2014). This method originates from the weight minimization problem of structures proposed by Michell (1904), where a solution method for the classical Michell truss structures was derived.

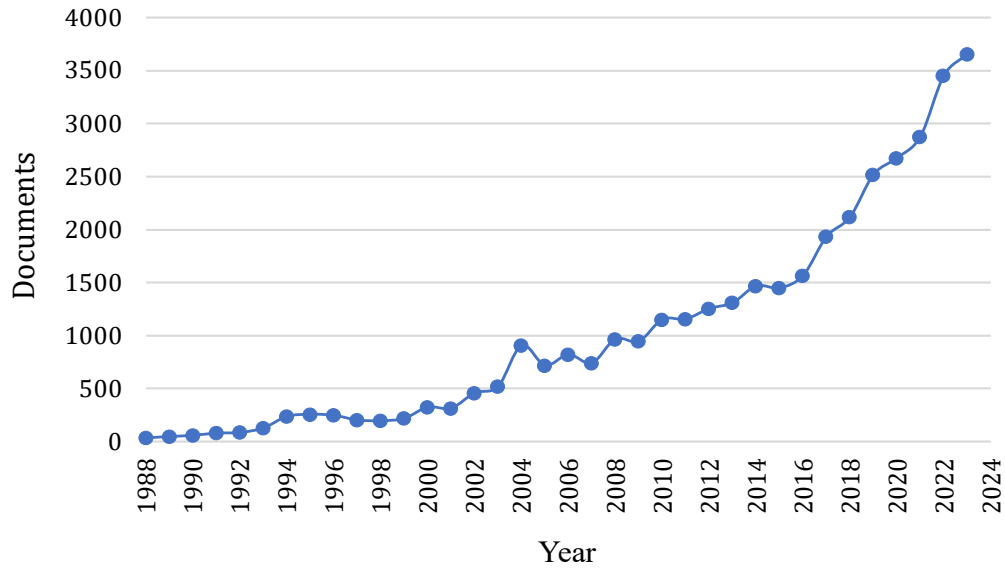
Topology optimization algorithms generally determine where the material should be included to generate a black-and-white or a solid-and-void design. Therefore, the structural material distribution is obtained by a binary “0-1”, where 0 indicates void and 1 indicates the presence of material. However, these algorithms lead to an integer programming problem, which has been revealed to be an unfeasible approach for large-scale topology optimization problems.

In the seminal work proposed by Bendsøe and Kikuchi (1988), a topology optimization strategy was introduced to exploit numerical homogenization to compute effective elastic properties of parametrized porous microstructures and provide the optimal shape design. After the significant contribution by Bendsøe and Kikuchi (1988), several numerical TO approaches have been proposed and published by many researchers (Figure 9). Sigmund (1994b) introduced the first application of topology optimization methods to design periodic materials employing inverse homogenization. This approach consists of formulating and implementing a numerical procedure to construct materials with any prescribed constitutive tensor. The subject has been later successively addressed by the density-based approach, such as SIMP - solid isotropic material with penalization (Bendsøe, 1989; Zhou; Rozvany, 1991; Rozvany et al., 1992) and RAMP - rational approximation of material properties (Stolpe; Svanberg, 2001), and more recently by other approaches such as ESO - evolutionary structural optimization (Huang; Xie, 2010), BESO - bidirectional evolutionary structural optimization (Huang et al., 2011) and the level-set-based topology optimization (Wang et al., 2003).

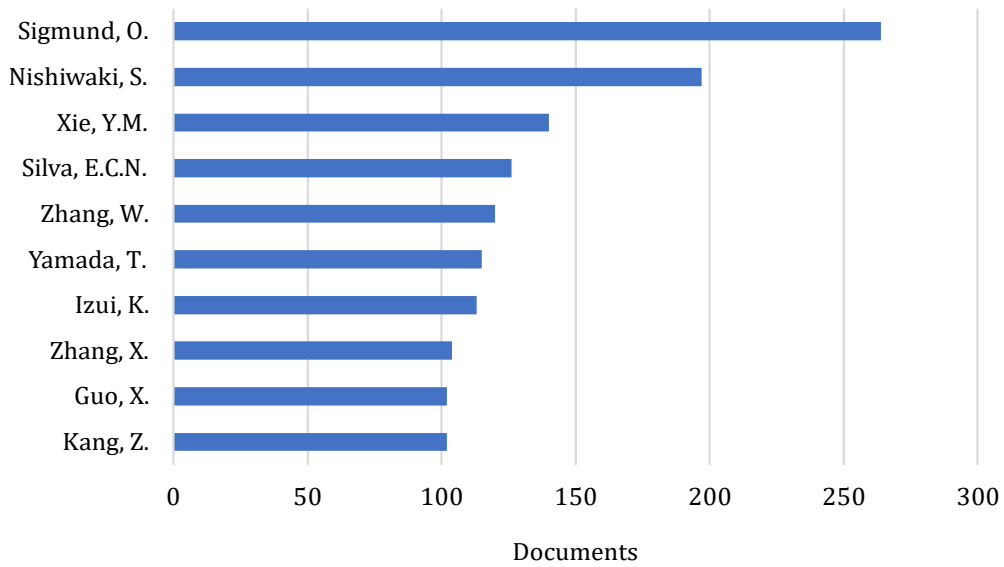
In the last decade, the dissemination of topology optimization concepts has been widespread due to the development of computational codes for academic purposes. In this context, Wang et al. (2021) and Wang et al. (2023) have published articles describing a comprehensive overview of educational computational codes, showcasing a variety of approaches and applications of topology optimization based on the finite element method.

The present dissertation employs the established density-based method due to its simplicity for computational implementation, concomitantly with the finite-volume theory for the microstructural analysis. The density-based method employs artificial density as a design variable through a non-linear interpolation model to handle material properties effectively, aiming to penalize intermediate density values to produce almost solid-and-void designs, providing physical consistency to the problem.

Figure 9 – Publications on topology optimization restricted to the search fields: engineering, materials science, and multidisciplinary



(a) by year



(b) by authors with more than 100 articles

Font: Scopus, access on January 22, 2024.

4.1 Density-based Approach

The most common form of topology optimization in structural applications is implemented through relaxed penalization methods, also called density-based approaches. This technique involves relaxing the original topology optimization problem by introducing a continuous design variable representing the presence of material, commonly named the relative artificial density, herein named only density. When employed in microstructural optimization, the objective is to identify the optimal topology within a representative unit cell that maximizes the effective material properties. The microstructural design allows for customizing various material behaviors,

defined by shear/bulk modulus, Poisson's ratio, thermal expansion, elasticity tensor, and other extremal properties (Sigmund; Torquato, 1997a; Sigmund, 2000; Xia; Breitkopf, 2015). This approach is justified by the considerations in Bendsøe and Kikuchi (1988), which indicates that the most important parameter to consider is the material density in the analysis domain, even though its description does not faithfully represent the material's micromechanical behavior.

In general, density-based methods employ a relation between the density design variable (ρ_q) and the local material property, in terms of Young's modulus (E_q), expressed by:

$$E_q(\rho_q) = g(\rho_q)E_0, \quad (32)$$

where E_0 is the Young's modulus of solid material and $g(\rho_q)$ corresponds to a non-linear density distribution function. In SIMP interpolation, the most widely used approach involves treating the local material as isotropic, with the density distribution function described by the following power-law:

$$g(\rho_q) = (\rho_q)^p, \quad (33)$$

where p is the material penalization parameter. Although quite common, this approach results in stiffness matrix singularity for low-density values, which is undesirable in numerical optimization and requires a minimum density threshold imposition. To circumvent this problem, Sigmund (2007) proposes the modified solid isotropic material with penalization, including a minimum value stiffness of soft (void) material (E_{min}), and the local material property can be expressed by:

$$E_q(\rho_q) = E_{min} + (\rho_q)^p (E_0 - E_{min}). \quad (34)$$

The modified SIMP interpolation method has many advantages, including the independence of the minimum stiffness value in terms of the material penalization parameter. Besides, the modified form is more straightforward for generalized use by various filtering schemes (Sigmund, 2007).

Another method for the density-based approach that is quite similar to the SIMP is the RAMP interpolation method. This approach's density distribution corresponds to a rational function of the local material properties. The expression of the modified rational approximation of material properties is given by:

$$E_q(\rho_q) = E_{min} + \frac{\rho_q}{1 + p(1 - \rho_q)} (E_0 - E_{min}). \quad (35)$$

The RAMP approach was introduced as a refinement of the original SIMP interpolation method, specifically designed to address the non-concavity issues and ensure convergence of solutions to a binary to "0-1" form (Stolpe; Svanberg, 2001; Sigmund; Maute, 2013). It addresses some limitations inherent to the SIMP method, mainly related to abrupt changes in material densities and the numerical instability associated with high penalization factors. The method employs a rational approximation of the penalization function, resulting in a smoother transition between

material densities and mitigating numerical issues, improving the convergence behavior and stability of the optimization process.

In general, density-based methods modify the local stiffness matrix in the following way:

$$\hat{\mathbf{K}}^{(q)}(\rho_q) = E_q(\rho_q)\hat{\mathbf{K}}^0, \quad (36)$$

where $\hat{\mathbf{K}}^0$ is the local stiffness matrix considering a unit Young's modulus.

4.1.1 Hashin-Shtrikman bounds for two-phase materials

The Hashin-Shtrikman (HS) bounds for two-phase materials express the theoretical limits of isotropic material properties by constructing composites from two linearly elastic isotropic materials (Bendsøe; Sigmund, 2003). Developed by Hashin and Shtrikman (1963), these limits express material parameters as functions of constituents volume fractions. They are determined based on variational principles where the medium is assumed to be infinite, and no geometric information of the constituents is considered.

Bendsøe and Sigmund (1999) rewritten the Hashin-Shtrikman bounds as functions of the material density ρ employed as interpolation schemes in topology optimization (all material laws involved are treated as isotropic). In SIMP and RAMP methods, the constitutive matrix corresponds to a composite material constructed from the void and the given material at a density ρ . Therefore, the effective bulk (κ^*) and shear (μ^*) moduli should satisfy the Hashin-Shtrikman bounds for two-phase materials. In the case of plane stress state and considering one phase as a void, the following expressions can be derived:

$$0 \leq \kappa^* \leq \frac{\rho\kappa_0\mu_0}{(1-\rho)\kappa_0 + \mu_0} \quad \text{and} \quad 0 \leq \mu^* \leq \frac{\rho\kappa_0\mu_0}{(1-\rho)(\kappa_0 + 2\mu_0) + \kappa_0}, \quad (37)$$

where κ_0 and μ_0 are the bulk and shear moduli of the solid material, respectively. Assuming a solid material with Poisson's ratio of $\nu = 1/3$, and evaluating Eq. (37) in terms of effective Young's modulus (E^*),

$$0 \leq E^* \leq \frac{\rho E_0}{3 - 2\rho}. \quad (38)$$

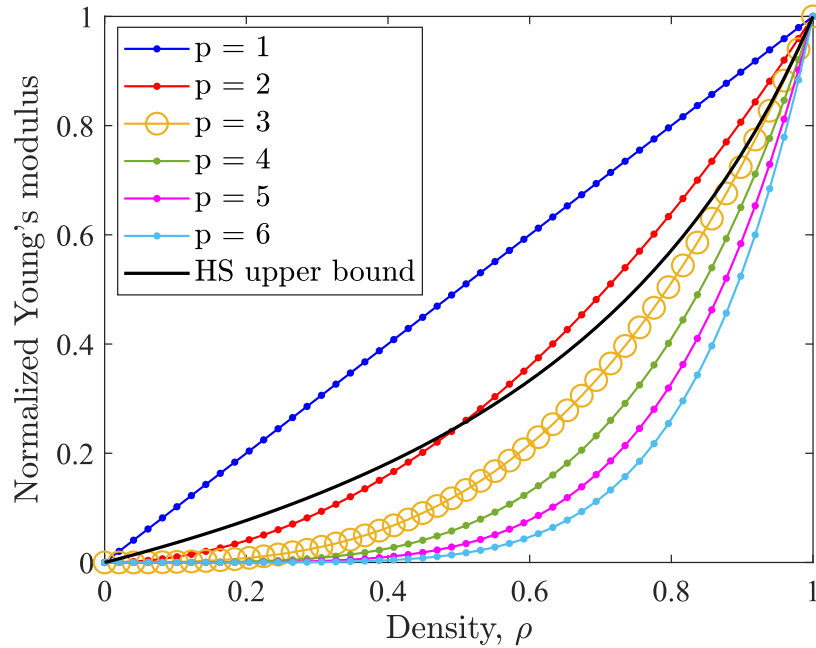
From the Eq. (38), the standard SIMP interpolation ($E = \rho^p E_0$) should satisfy:

$$\rho^p E_0 \leq \frac{\rho E_0}{3 - 2\rho} \quad \text{for all } 0 \leq \rho \leq 1. \quad (39)$$

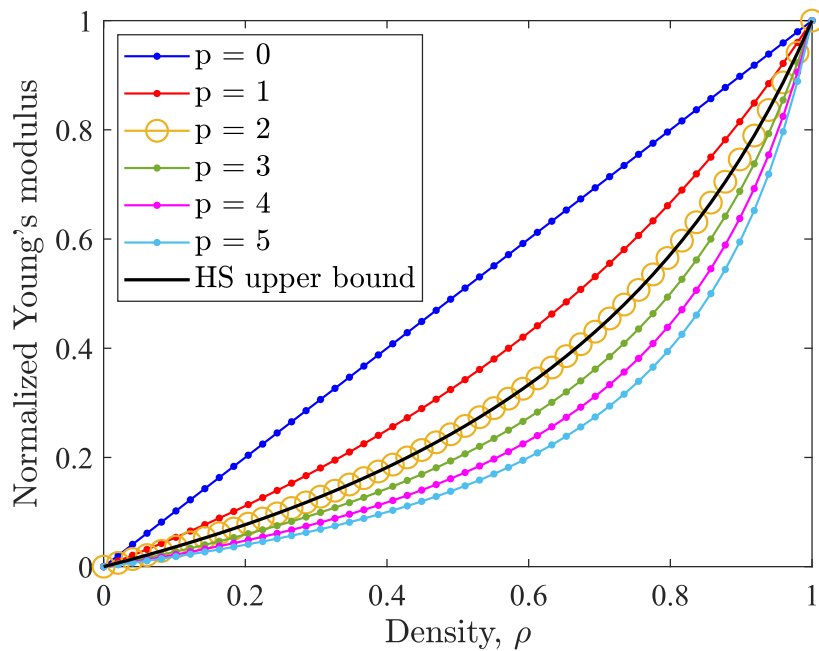
The relation in Eq. (39) is valid only when $p \geq 3$ and presumes that the Poisson's ratio is independent of the density, which results in a stronger restriction. Similarly, the RAMP requires $p \geq 2$. Figure 10 illustrates the effect of material penalization parameter p for SIMP and RAMP methods. Note that the SIMP, with $p \geq 3$, and the RAMP, with $p \geq 2$, adhere to the HS upper bound. The RAMP method mathematically expresses the HS upper bound in the particular instance where $p = 2$. In SIMP results, wide spacing of penalization curves is intrinsically related to abrupt changes in material densities. On the other hand, the RAMP method provides

thinner spacing, which leads to smoother transitions along penalization curves, a required aspect in the continuation method employing an interpolation scheme. Furthermore, as mentioned by Bendsøe and Sigmund (2003), if the design of two-material structures is the goal of the topology optimization, the RAMP model is, in a sense, more physical than SIMP.

Figure 10 – Effect of the material penalization parameter



(a) SIMP



(b) RAMP

Font: Author (2024).

The appearance of intermediate densities is essential for problem relaxation. However, this pattern in the final topology can be undesirable for the material designer, who must interpret

the result and propose a feasible final solution. Although desirable, very high values of the material penalization parameter lead the problem to the “0-1” design pattern, where a solution is not guaranteed, as mentioned by Rozvany et al. (1995). Therefore, the sensitivity of these optimization approaches to the choice of material penalization parameter p highlights the need for careful consideration and understanding of the constraints associated with each approach.

4.1.2 Problem formulation for material design

The following mathematical expression provides the general formulation for optimizing linearly elastic properties of periodic materials:

$$\begin{aligned}
& \text{find : } \boldsymbol{\rho} = \{\rho_1, \rho_2, \dots, \rho_{N_q}\}^T, \\
& \max_{\boldsymbol{\rho}} : \phi(\boldsymbol{\rho}) = \sum_{i,j=1}^3 \alpha_{ij} C_{ij}^*, \\
& \text{s.t. : } \hat{\mathbf{K}} \hat{\mathbf{u}}' |_{(i)} = \hat{\mathbf{F}} |_{(i)}, \\
& \quad : \frac{1}{\Omega} \sum_{q=1}^{N_q} v_q \rho_q \leq \vartheta, \\
& \quad : 0 \leq \rho_q \leq 1, \quad q = 1, \dots, N_q,
\end{aligned} \tag{40}$$

where $\boldsymbol{\rho}$ corresponds to the density vector, ϕ is the objective function defined by a linear combination of the effective constitutive matrix components, α_{ij} is the weight factor, enabling the definition of diverse objective functions by varying its values, v_q denotes the volume of the q th subvolume, ϑ is the volume fraction of solid material, $\hat{\mathbf{u}}' |_{(i)}$ and $\hat{\mathbf{F}} |_{(i)}$ are the global surface-averaged fluctuating displacement vector and the global load vector, respectively, due the application of the strain case (i). The global load vector depends on material properties, which makes it dependent on design variables (densities). This characteristic renders the topology optimization procedure in material design intrinsically dependent on the specific design load.

In this approach, the objective functions are established in terms of the effective constitutive matrix components. The cellular material shear modulus maximization corresponds to maximizing the function $\phi = C_{33}^*$, assuming the weight factor as $\alpha_{33} = 1$ and $\alpha_{ij} = 0$ for the other components. For the 2D cellular material bulk modulus maximization, the objective function in the optimization problem can be given by $\phi = 1/4 (C_{11}^* + C_{21}^* + C_{12}^* + C_{22}^*)$, where $\alpha_{33} = 0$ and $\alpha_{ij} = 1/4$ for the other components, considering a plain strain state, which is also known in the literature as the plane-strain bulk modulus (Hyer; Waas, 2017). Making use of the symmetry of the effective constitutive matrix ($C_{21}^* = C_{12}^*$) and known of rotating the RUCs shown in Figures 6-7 by 90-degree angle result in cells with the same effective materials properties, the objective function can be simplified as $\phi = 1/2 (C_{11}^* + C_{12}^*)$. Thus, considering the concept of plane-strain bulk modulus, the effective bulk modulus for the 2D cellular material can be evaluated as $\kappa^* = 1/2 (C_{11}^* + C_{12}^*)$.

In the case of cellular materials with negative Poisson's ratio, the optimization objective function adopted follows the strategy developed by Xia and Breitkopf (2015) for finite element analysis, and is defined as $\phi = -C_{12}^* + \beta^{iter} (C_{11}^* + C_{22}^*)$, where $0 < \beta < 1$ is a fixed numerical parameter controlling the structure's stiffness along the material principal directions, and the exponent $iter$ is the design iteration number. As the iteration number increases during optimization, the objective function tends towards $\phi = -C_{12}^*$, which results in cellular materials with negative Poisson ratios.

4.2 Sensitivity Analysis

The solution of the optimization problem defined in Eq. (40) commonly requires the calculation of the gradient of the objective function and constraints concerning the design variable. This calculation is essential for performing a sensitivity analysis of the problem, as it reveals how sensitive that function is to variations in the design variables. The sensitivity of the effective constitutive matrix components is evaluated as follows:

$$\frac{\partial C_{ij}^*}{\partial \rho_q} = \frac{1}{\Omega} \hat{\mathbf{u}}^{(q)T} |_{(i)} \frac{\partial \hat{\mathbf{K}}^{(q)}}{\partial \rho_q} \hat{\mathbf{u}}^{(q)} |_{(j)}. \quad (41)$$

Equation (41) relates the total surface-averaged displacement field to the derivatives of the local stiffness matrix concerning the density for the q th subvolume. Unlike the structural optimization problem with prescribed boundary load, setting periodic boundary conditions on the repeated unit cell leads to obtaining the sensitivity of the objective function with a positive sign, which implies maximizing the complementary strain energy and effective constitutive matrix components along the optimization process.

Another approach to calculating the gradient of the objective function can be established from the concepts of the mean-field theory. In this approach, the sensitivity of the effective constitutive matrix components is established as follows:

$$\frac{\partial C_{ij}^*}{\partial \rho_q} = c^{(q)} \bar{\boldsymbol{\varepsilon}}^T |_{(i)} \frac{\partial C_{ij}^{(q)}}{\partial \rho_q} \left(\bar{\boldsymbol{\varepsilon}} |_{(j)} + \bar{\mathbf{B}}^{(q)} \hat{\mathbf{u}}'^{(q)} |_{(j)} \right) + \hat{\boldsymbol{\lambda}}^{(q)T} \left(\frac{\partial \hat{\mathbf{K}}^{(q)}}{\partial \rho_q} \hat{\mathbf{u}}'^{(q)} |_{(j)} + \frac{\partial \hat{\mathbf{H}}^{(q)}}{\partial \rho_q} \bar{\boldsymbol{\varepsilon}} |_{(j)} \right), \quad (42)$$

where $\bar{\mathbf{B}}^{(q)}$ corresponds to the strain/displacement operator and $\hat{\boldsymbol{\lambda}}^{(q)}$ is the local solution of the adjoint problem (Bendsøe; Sigmund, 2003; Christensen; Klarbring, 2008). The mathematical proof of the sensitivities expressions in Eqs. (41-42) are shown in Appendix A.

4.3 Optimality Criteria Method

The optimality criteria (OC) method is one of several approaches to solve topology optimization problems. It corresponds to the heuristic updating scheme gradient-based optimization approach and represents a robust method frequently employed in structural optimization problems. As explained in Bendsøe and Sigmund (2003), after obtaining the displacement solution,

the TO defined by Eq. (40) is addressed by applying a standard optimality criteria method to update the density variable (ρ_q^{new}) according to the following strategy:

$$\rho_q^{new} = \begin{cases} \max(0, \rho_q - m), & \text{if } \rho_q (\beta_q)^\eta \leq \max(0, \rho_q - m), \\ \min(1, \rho_q + m), & \text{if } \rho_q (\beta_q)^\eta \geq \min(1, \rho_q + m), \\ \rho_q (\beta_q)^\eta, & \text{otherwise,} \end{cases} \quad (43)$$

where m is the positive move limit, η is a numerical damping factor, and β_q is the optimality condition evaluated by:

$$\beta_q = -\frac{\partial \phi}{\partial \rho_q} \left(\lambda \frac{\partial V}{\partial \rho_q} \right)^{-1}, \quad (44)$$

with λ representing the positive Lagrangian multiplier, which can be determined using a bisection algorithm to enforce the satisfaction of the constraint on the volume fraction of solid material (ϑ). The optimality criteria method, in general, is employed to solve compliance minimization problems. However, adopting periodic boundary conditions based on a displacement formulation and imposition of macroscopic strains maximizes the optimization procedure's compliance function and material stiffness. In this case, derivatives of the effective constitutive matrix components are always positive, which requires a modification in the original algorithm to consider only the positive gradients as follows:

$$\beta_q = \frac{\partial \phi}{\partial \rho_q} \left(\lambda \frac{\partial V}{\partial \rho_q} \right)^{-1}. \quad (45)$$

4.4 Filtering Techniques

In topology optimization, filtering techniques modify the density values (or sensitivities) to prevent numerical issues affecting the results' quality. These issues include checkerboarding, referring to the formation of adjacent solid-void subvolumes arranged in a checkerboard pattern, and mesh dependency, which is not as troublesome as the previous issue, where different topologies result from identical design domains with varying sizes of discretization (Deaton; Grandhi, 2013). Sigmund (2007) provides a comprehensive overview of filtering methods corresponding to the most common techniques, including the sensitivity filter (Sigmund; Petersson, 1998) and the density filter (Bourdin, 2001; Bruns; Tortorelli, 2001). These methods adjust a subvolume's sensitivity or density values, considering the sensitivities or densities of the subvolumes within a localized neighborhood.

The sensitivity filter modifies the subvolumes sensitivities $\partial \phi / \partial \rho_q$ as follows:

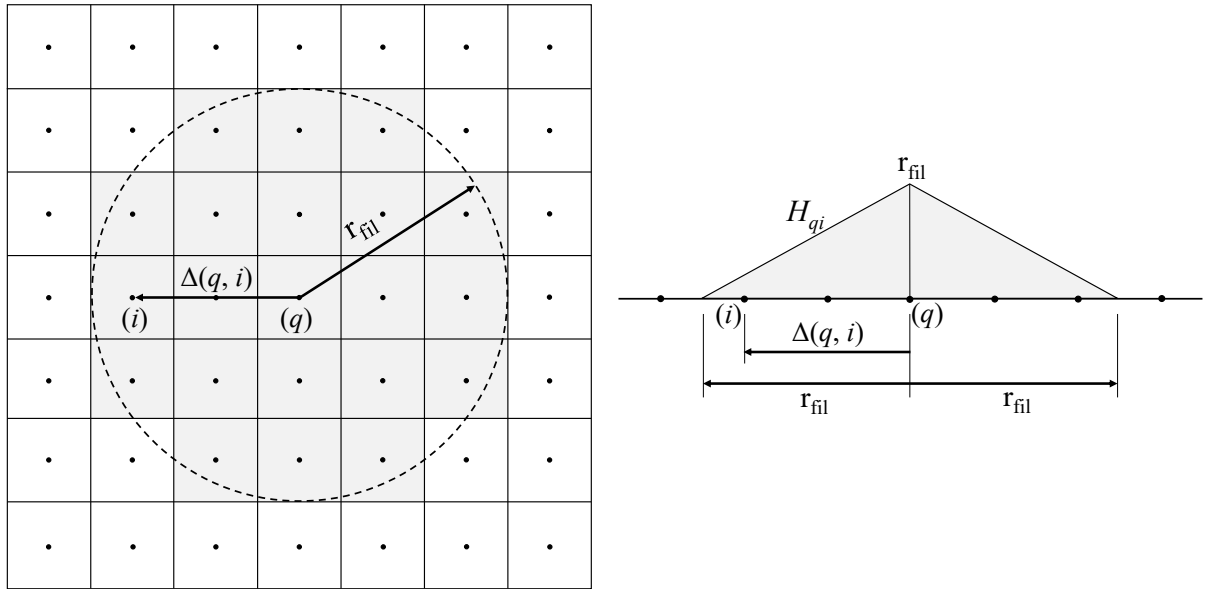
$$\widehat{\frac{\partial \phi}{\partial \rho_q}} = \frac{1}{\max(\gamma, \rho_q) \sum_{i \in N_q} H_{qi}} \sum_{i \in N_q} H_{qi} \rho_i \frac{\partial \phi}{\partial \rho_i}, \quad (46)$$

where the term γ is a small positive number equals to 10^{-3} introduced in order to avoid division by zero. The convolution operator H_{qi} in Eq. (46) is determined as follows:

$$H_{qi} = \begin{cases} r_{\text{fil}} - \Delta(q, i), & \text{if } \Delta(q, i) \leq r_{\text{fil}} \\ 0, & \text{if } \Delta(q, i) > r_{\text{fil}}, \end{cases} \quad (47)$$

where r_{fil} is the filter radius and the operator $\Delta(q, i)$ is defined as the distance between the center of subvolume q and the center of subvolume i . As shown in the illustration of Figure 11, the convolution operator H_{qi} decays linearly with the distance from subvolume q .

Figure 11 – Illustration of filtering technique



Font: Author (2024).

The density filter modifies the original density design variable for each subvolume, which depends on the densities of neighboring subvolumes. The filtered densities $\tilde{\rho}_q$ are referred to as the physical design variables because they are subsequently used directly in the simulation of the underlying problem (Sigmund, 2007). The filter density expression is given by:

$$\tilde{\rho}_q = \frac{1}{\sum_{i \in N_q} H_{qi}} \sum_{i \in N_q} H_{qi} \rho_i. \quad (48)$$

4.5 Continuation Method

A gradient-based algorithm employed to update topology strongly depends on choices of optimization parameters and starting guesses. Besides, the material interpolation methods that penalize intermediate variable densities introduce non-convexities into the problems, resulting in multiple local extremal solutions. It is expected to employ a continuation method to control the material penalization parameter (p), looking for a final design with a short distance from the global extremal solution (Rojas-Labanda; Stolpe, 2015). In this work, this method initially solves the problem with $p_0 = 1$ when employing the SIMP method, and $p_0 = 0$ for the RAMP method, where the optimal design typically features intermediate density values represented by gray regions. Subsequently, the material penalization parameter is gradually incremented in small steps (Δp), and the problem is repeatedly resolved until the desired value is achieved (p_{max}).

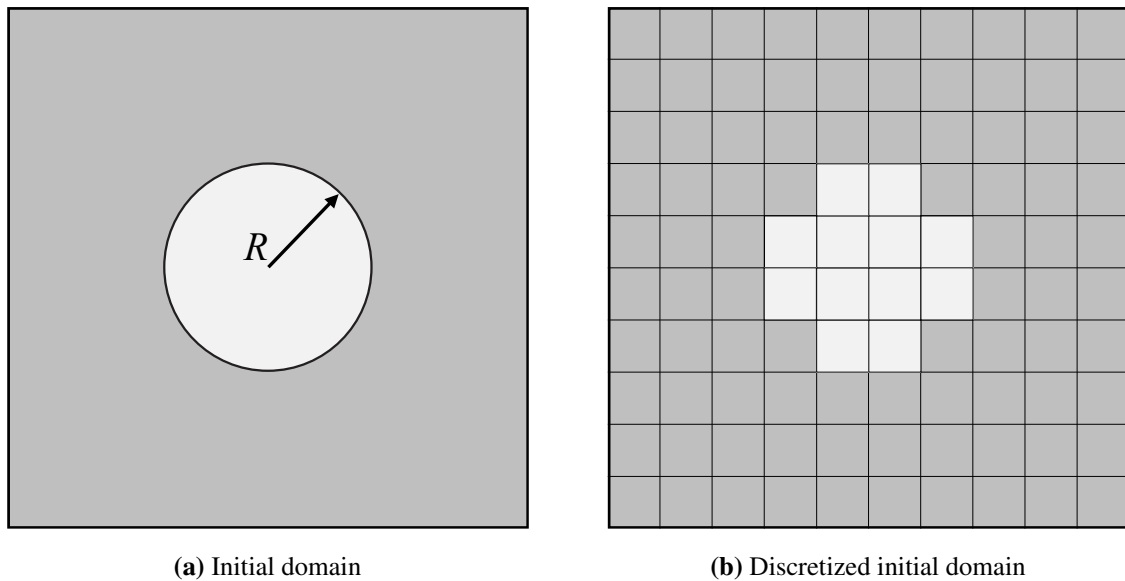
In structural topology optimization, researchers typically set the material penalization parameter to $p_{max} = 3$ in the SIMP method, a practice observed in numerous studies such as those by Bendsøe and Sigmund (2003) and Xia et al. (2016). This value is generally considered adequate for generating predominantly solid-and-void designs. However, it is worth noting that while the prevailing recommendation is often $p_{max} = 3$, the literature offers a range of alternative values. For example, Petersson and Sigmund (1998) suggest $p_{max} = 5$, while Edwards et al. (2007) and Sridhara et al. (2022) advocate for $p_{max} = 10$, asserting that it provides a suitably discretized solution. This work assigns the material penalization parameter for each specific case of the material's effective property to be maximized based on previous experiments focused on obtaining a final topology closer to the solid-and-void pattern.

5 NUMERICAL EXAMPLES

5.1 Initial Remarks

Several numerical examples are analyzed to assess the performance of the finite-volume theory employed in topology optimization for designing periodic cellular materials with optimized elastic properties. These analyses aim to achieve desired properties, such as effective maximized shear and bulk moduli (κ^* and μ^*) or auxetic materials with an effective negative Poisson's ratio (ν^*), without employing filtering techniques in the topology optimization procedure, except for the comparison case with the theoretical HS upper bound. For simplicity, a square repeating unit cell with two axes of symmetry along the horizontal and vertical directions is adopted, with a specific emphasis on designing orthotropic materials, due to the shape of the unit cell. Normalized reference properties include Young's modulus $E_0 = 1$, Poisson's ratio $\nu = 0.3$, and a minimum Young's modulus value of $E_{min} = 10^{-9}$ to simulate porous (void) regions and prevent singularity in the global stiffness matrix. In addition, the analyses are performed considering the plane stress state, aiming to simulate thin sheets of perforated materials.

Figure 12 – Illustrative analysis domain employed in the Cartesian coordinates formulation of the FVT



Font: Author (2024).

Unlike structural topology optimization, which starts from an initial design domain featuring a uniform density distribution, periodic material design procedures require an initial domain with material heterogeneity to enable the calculation of fluctuating displacements. Here, the initial domain or initial material design considers a circular shape localized at the center of the square unit cell, representing the soft material as illustrated in Figure 12(a). The finite-volume simulations employ a structured mesh similar to a discretized domain in Figure 12(b), where the circular region is approximated by defining the soft material's radius or the number

of subvolumes inside this region. Nonetheless, the initial material design volume fraction is strategically suitable for the constraint solid material volume fraction in the topology optimization procedure to avoid numerical instability in the initial algorithm's iterations. Furthermore, an optimal solution is supposed to be reached when the maximum variation of the design variables is lower than a user-defined tolerance (tol). As the literature suggests, the algorithm's tolerance and the optimization parameter's move limit are set to $tol = 0.01$ and $m = 0.2$, respectively.

The analyses are performed with a promising computational code in Matlab language, named TopMatFVT, implemented in the Matlab[®] R2023a programming language running in a computer equipped with a 12th generation Intel[®] Core[™] i7-1260P processor (2.10 GHz and 16.0 GB DDR5 RAM) and a 64-bit Windows 11 Pro operating system. The flowchart description of the TopMatFVT is shown in Appendix B.

5.2 Cellular Materials Shear Modulus Maximization

The present study proposes an investigation focusing on cellular material design with maximized shear modulus. This study initially compares the results obtained by the developed TopMatFVT with the finite element outcomes, considering two paths for determining effective properties. Subsequently, the study examines the influence of several aspects, including the variation of increments in penalization parameters within the continuation method, the impact of initial material design, and how increasing volume fraction constraints affect the optimized topology.

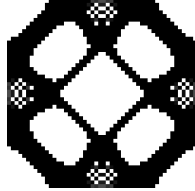
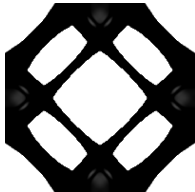
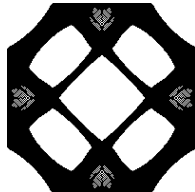
5.2.1 Comparison with finite element analysis

The analyses compare results obtained through the TopMatFVT implemented in the context of the finite-volume theory (Appendix B) with those produced by the topX educational code developed by Xia and Breikopf (2015). The topX code employs Q4 finite element with unitary element discretization and Matlab's vectorization resources for assembling the stiffness matrix and load vector, drawing inspiration from the work of Andreassen et al. (2011). In this investigation, the SIMP method penalizes intermediate densities with a fixed material penalization parameter $p = 3$ since this method is the only one implemented in the topX code. The damping factor in the OC method (η) regularizes possible oscillations during the optimization process, specifically in cases where no filtering techniques are applied. As the literature suggests, $\eta = 1/2$ provides faster convergence for the overall process. The aforementioned damping factor is employed in this analysis to avoid modifying the original topX code and to make comparisons more suitable. A comparative analysis focuses on the quality of optimized microstructural topologies and the computational codes' efficiency in processing time.

The headers of the Matlab functions within computational codes for a mesh discretization of 50×50 unitary elements/subvolumes are established as: `topX(50, 50, 0.5, 3, 1e-9, 1)` and `TopMatFVT(50, 50, 0.5, 3, [], [])`, which input parameters correspond, in this order,

to discretization in the horizontal and vertical directions of the domain, volume fraction constraint, material penalization parameter, filtering radius, and filter type. Despite the analysis conducted without a filtering scheme, it becomes crucial in the topX code to define the filtering parameters to avoid numerical inconsistencies due to the application of the convolution operator as shown in Eqs. (46) and (48). In this scenario, a minimum filtering radius ($1e-9$) was a strategic choice, even though it does not delineate a viable filtering region. For a comprehensive and reliable time processing measurement, both functions are called five times, and then the average of the measures is calculated.

Table 1 – Optimized topologies with maximized shear modulus employing TopMatFVT and topX codes

Discretization/ Soft material radius	TopMatFVT Strain energy-based	TopMatFVT Mean-field theory	topX
50×50 $R = 50/6$	 $\mu^* = 0.1223$ 28 iter and 1.48 s	 $\mu^* = 0.1223$ 28 iter and 1.92 s	 $\mu^* = 0.1208$ 29 iter and 1.39 s
100×100 $R = 100/6$	 $\mu^* = 0.1267$ 29 iter and 3.51 s	 $\mu^* = 0.1267$ 29 iter and 8.16 s	 $\mu^* = 0.1254$ 37 iter and 3.75 s
200×200 $R = 200/6$	 $\mu^* = 0.1302$ 36 iter and 18.09 s	 $\mu^* = 0.1302$ 36 iter and 42.29 s	 $\mu^* = 0.1250$ 75 iter and 29.99 s

Font: Author (2024).

Table 1 shows optimized topologies with maximized shear modulus for a fixed solid material volume fraction constraint of 50%, considering different soft material radii (R) over the mesh discretization for defining the initial material heterogeneity, which produce the same porosity of 8.72% on both cases. Initially, this study compares the final topologies obtained using two approaches for determining effective material properties: strain energy-based and mean-field

theory, within the context of finite-volume analyses (TopMatFVT). As expected, the optimized topologies are identical, and the total number of iterations (iter) for solution convergence is the same, given that the approaches for determining macroscopic properties are equivalent. However, the processing time during the optimization procedure was slightly higher in all scenarios when using the mean-field theory strategy. This increase in processing time is due to the requirement to calculate the adjoint vector at each iterative step, which is necessary to determine the sensitivities of the effective constitutive matrix components.

The results obtained through the finite element method (topX) show processing times lower than those achieved by employing the finite-volume theory with the mean-field theory approach despite requiring more iterations for solution convergence. On the other hand, they exhibit slightly higher processing times compared to the results from the finite-volume theory employing the strain energy-based approach. Additionally, the optimized topologies obtained through the finite element method display a checkerboard pattern (artificial stiffness), which are expected results since no filters were employed to regularize the problem's solution. Furthermore, these optimized topologies exhibit maximized shear modulus values (μ^*) lower than those obtained via finite-volume theory, approximately 4% for the case of the mesh discretized into 200×200 elements/subvolumes.

Despite the optimized topologies presenting localized gray regions, all analyzed scenarios with the finite-volume theory presented material designs free from the checkerboard, demonstrating this powerful technique's excellent performance when used to assist in the design of cellular materials. However, the continuation method is recommended to mitigate gray regions and achieve manufacturable microstructural topologies.

The optimized topologies generated are intended as preliminary suggestions for a material design, which must refine the edges of the optimized topology depending on the desired level of detail. Given the similarities in the optimized topologies produced with the approaches employed for determining effective material properties, which represent two variations of the same material modeling and are physically equivalent, the following examples will focus on the strain energy-based approach due to its superior computational efficiency.

5.2.2 Influence of the continuation method

Firstly, an initial domain discretized into 100×100 unitary subvolumes with the convenient imposition of the PBCs defines the numerical model employed in the following analyses. It is important to emphasize that the objective of this work is not to present a detailed account of the aspects related to mesh dependency, given that such dependency is strictly associated with the desired level of solution refinement (more refined meshes induce the appearance of holes in the optimized topology due to the presence of multiple local extremal). The optimality criteria (OC) method updates the design variables employing a damping factor $\eta = 1/3$ in the following analyses, strategically selected to regularize displacement oscillations in less dense

regions during the iterative process and to avoid the oscillatory phenomena that can occur in analyses without filtering scheme with the FVT simulations using the continuation method, particularly for the SIMP method, as observed by Araujo (2018) for compliance minimization problems. The same damping factor value is consistently applied in the RAMP analysis, ensuring a fair and meaningful comparison with the microstructural topologies derived from the SIMP method.

Table 2 – Optimized topologies with maximized shear modulus employing continuation method

Increment	SIMP	RAMP
$\Delta p = 0.1$	 $\mu^* = 0.1299$ 470 iter	 $\mu^* = 0.1323$ 585 iter
$\Delta p = 0.5$	 $\mu^* = 0.1275$ 243 iter	 $\mu^* = 0.1316$ 318 iter
$\Delta p = 1$	 $\mu^* = 0.1269$ 146 iter	 $\mu^* = 0.1313$ 243 iter

Font: Author (2024).

An initial domain characterized by a soft material radius $R = 100/6$ with a solid volume fraction constraint $\vartheta = 50\%$ is employed, and to verify the influence of the continuation method on the optimized topologies, three increments in the material penalization parameter (Δp) are considered. The results are then compared with those achieved using a fixed penalization strategy. Although the material penalization parameter in the SIMP and RAMP starts from different values, as mentioned in Section 4.5, the same range of possible values is conveniently adopted for a suitable comparison. Thus, the maximum limits are $p_{max} = 4$ for the SIMP and $p_{max} = 3$ for the RAMP. The selection of these maximum limits enables solid-and-void designs for the

optimized microstructural topologies with maximized shear modulus.

Table 2 shows the optimized microstructural topologies with maximized shear moduli concerning the increment on the material penalization parameter. The analysis investigates how the continuation method's choice of material penalization parameter influences the final topologies when employing both SIMP and RAMP approaches. Notably, this parameter variation strongly affects the optimized microstructural topology when employing the SIMP method, resulting in a difference of approximately 2.31% between the shear moduli for the topologies obtained with $\Delta p = 0.1$ and $\Delta p = 1$. Conversely, the RAMP method demonstrates stability across the generated microstructural topologies, even when subjected to varying increments in the material penalization parameters. As an essential parameter to assist in choosing the approach, the RAMP method produced final topologies with higher shear stiffness (μ^*) than the SIMP method in all cases. Besides, the final topologies generated by the RAMP method present simpler designs, thicker bars, and smaller perimeters (cut path), which are crucial features for the manufacturing process.

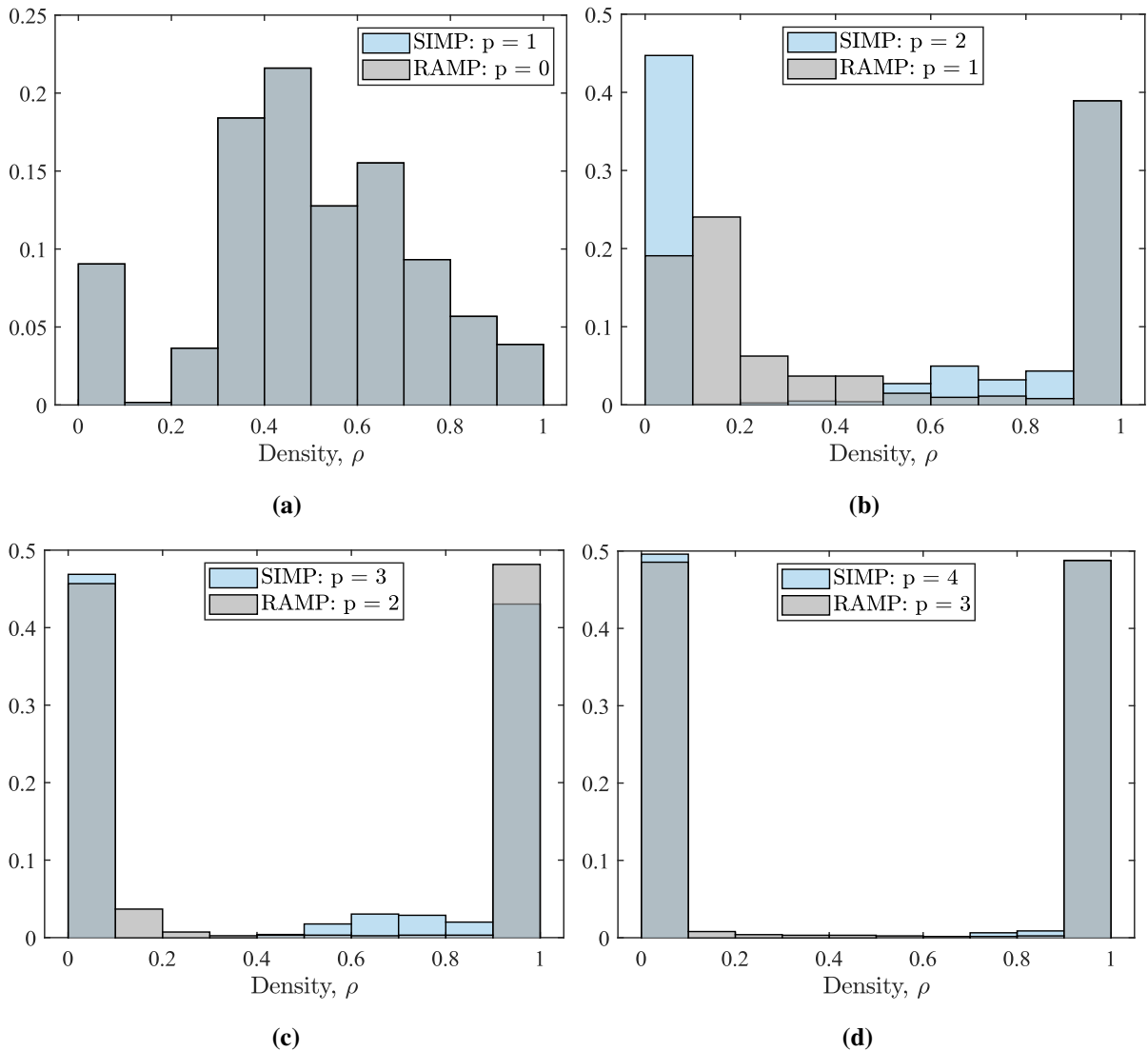
Table 3 – Optimized topologies with maximized shear modulus employing fixed penalization

SIMP ($p = 4$)	RAMP ($p = 3$)
	
$\mu^* = 0.1207$ 25 iter	$\mu^* = 0.1305$ 88 iter

Font: Author (2024).

These results suggest that implementing the continuation method does not necessarily require a small increment to produce good material designs, especially for the RAMP method, which has a similar optimized topology compared with the fixed penalization strategy and presents slightly higher shear stiffness. Naturally, the continuation method requires a more significant number of iterations and, consequently, higher computational costs than the fixed penalization strategy (Table 3). However, it minimizes the possibility of getting trapped in a distant local extremal from the global solution. For both methods of material penalization (SIMP and RAMP) with or without a continuation method, the optimized topologies achieved are checkerboard-free patterns, demonstrating the potential of the finite-volume theory when employed for designing cellular materials.

Figure 13 – Comparison of material density distribution considering the continuation scheme with the increment $\Delta p = 1$ for the SIMP and RAMP methods



Font: Author (2024).

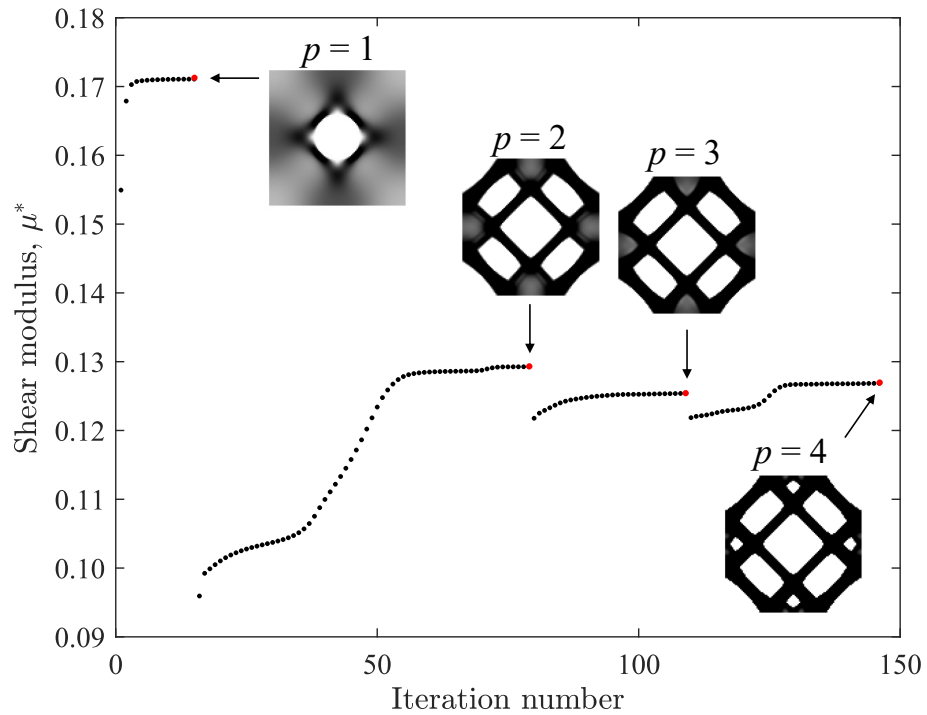
Figure 13 shows the material distribution across various density levels for an increment of $\Delta p = 1$ in the material penalization parameter, inspired by the optimized topologies in Table 2. In Figure 13(a), the material distribution is the same for both approaches, as expected since the respective approaches are equivalent to the initial penalization stages, as can be concluded based on the Eqs. (34-35). The increase in the parameter (p) reduces the intermediate densities, resulting in a material distribution close to the solid-and-void pattern. Furthermore, the relaxation in the intermediate densities produced by the density-based methods, although it has no physical meaning, is essential to avoid the discrete programming (0-1), which causes numerical ill-conditioning due to the abrupt change in the values of the design variables that require many iterations and, therefore, higher computational time. As the increment progresses, the SIMP method penalizes intermediate densities more quickly, as illustrated in Figure 13(b), which is justified by the penalty curves showing slight changes in the material's stiffness for low densities. This feature can create difficulties in convergence when using strategies based on objective

function gradients with high material penalization parameters. On the other hand, in the final stages, the RAMP method sufficiently penalizes intermediate densities, achieving a more defined solid-and-void pattern, as illustrated in Figures 13(c)-13(d).

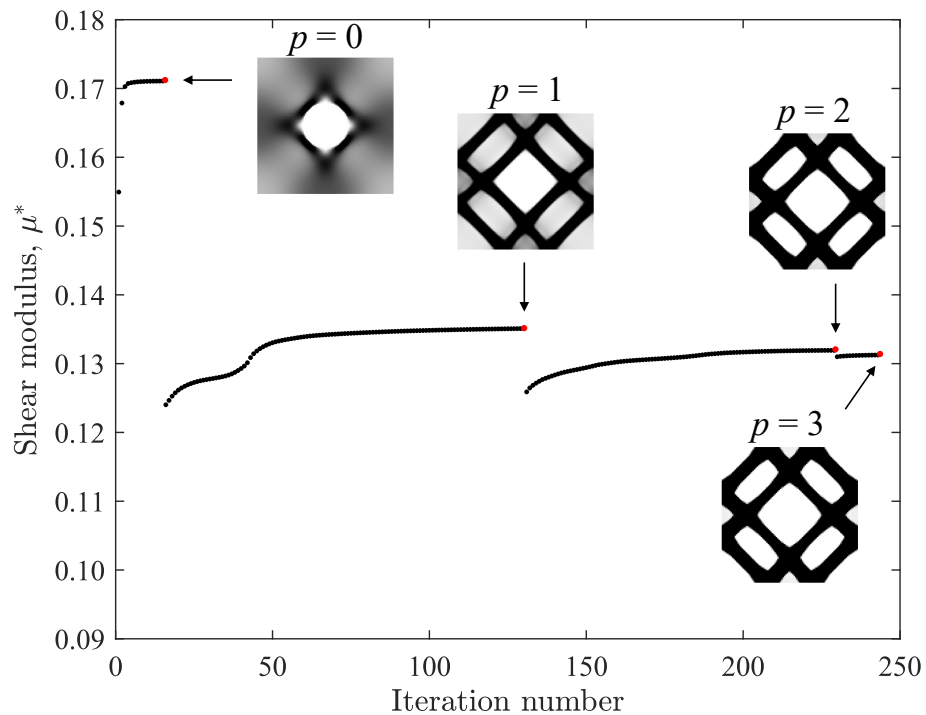
Figure 14 illustrates the evolutionary trajectory of the maximized shear modulus regarding the material penalization parameter stage ($\Delta p = 1$) in the continuation method, considering the SIMP and RAMP approaches. The results show the local optima points corresponding to the solution problems for different material penalization parameters (red dots). Optimized topologies in the initial penalization stages ($p = 1$ for the SIMP and $p = 0$ for the RAMP) are equivalent because the material distribution is the same for both approaches. Furthermore, the presence of gray regions in the topologies obtained at the initial penalization stages is evident, making it necessary to evolve this parameter to levels where the penalization curves do not violate the HS upper bound, $p \geq 3$ for SIMP and $p \geq 2$ for RAMP, as discussed in Section 4.1.1. The observed presence of wide gaps between sets of values with different p is more expressive in SIMP results, and this can be attributed to the wide spacing of penalization curves as illustrated in Figure 10. A gradual decrease in the discontinuity between the curves representing the trajectory of shear stiffness is visible for the SIMP and RAMP methods. However, while the optimum value for the RAMP method consistently decreases with the increment of the penalization parameter, this does not occur for the SIMP method, where the optimum value for $p = 4$ is higher than the optimum value for $p = 3$.

In summary, while both SIMP and RAMP are widely used in topology optimization, RAMP's ability to provide smoother transitions and more apparent solid-and-void solutions often gives it a more significant physical appeal in practical applications. It is worth noting that while the RAMP method necessitates a more significant number of iterations compared to SIMP, it has demonstrated superior numerical stability throughout the penalization process. Consequently, the following analyses will exclusively employ the RAMP method, maintaining an incremental approach ($\Delta p = 1$) in the material penalization parameter. This strategic decision is grounded in the method's reliability and capacity to deliver high-quality results consistently.

Figure 14 – Evolutionary trajectory of the maximized shear modulus



(a) SIMP



(b) RAMP

Font: Author (2024).

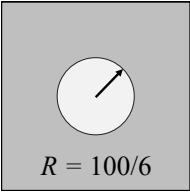
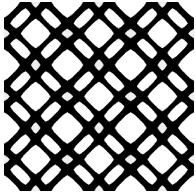
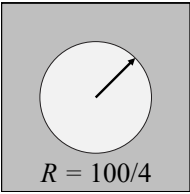
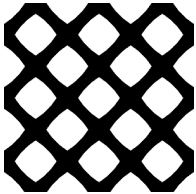
5.2.3 Impact of initial material design

Alvarez et al. (2019) assert that the successful resolution of a topology optimization problem through density-based methods like SIMP and RAMP hinges upon several key variables.

These variables encompass the material penalization parameter, mesh size, filtering scheme, filter radius, the optimization solver employed for updating design variables, and the choice of the initial material design, requiring the designer's experiences as observed by Xia and Breitkopf (2015) and Liu et al. (2021), among others.

The analyses examine the initial material design impact on the optimized microstructural topologies, considering two distinct initial domains while adhering to the same solid volume fraction constraint of $\vartheta = 50\%$. These initial domains are characterized by soft material radii $R = 100/6$ and $R = 100/4$, which produce porosities of 8.72% and 19.76%, respectively. The results in Table 4 show that the choice of initial material design strongly influences the final design because multiple local optima points exist in this approach to designing cellular materials. Nonetheless, when the material designer possesses prior knowledge of the desired optimal topology shape, opting for an initial guess aligning with the desired objective is advisable.

Table 4 – Impact of initial material design on the optimized topology with maximized shear modulus

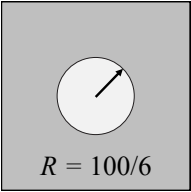
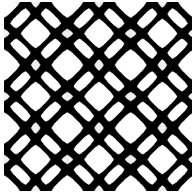
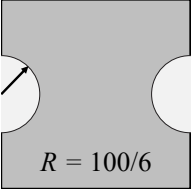
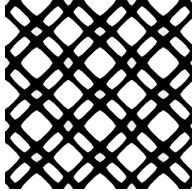
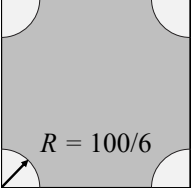
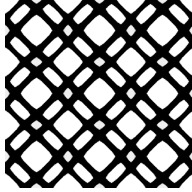
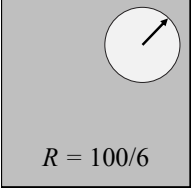
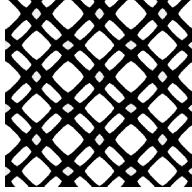
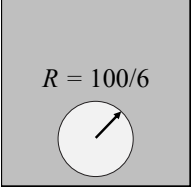
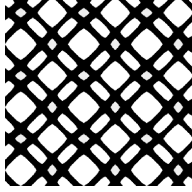
Initial domain	Unit cell	3×3 cells	Effective properties
 $R = 100/6$			$\mathbf{C}^* = \begin{bmatrix} 0.1833 & 0.1556 & 0 \\ sym. & 0.1833 & 0 \\ \mu^* = 0.1313 & & 0.1313 \end{bmatrix}$
 $R = 100/4$			$\mathbf{C}^* = \begin{bmatrix} 0.1980 & 0.1532 & 0 \\ sym. & 0.1980 & 0 \\ \mu^* = 0.1353 & & 0.1353 \end{bmatrix}$

Font: Author (2024).

Additionally, when the same periodic arrangement is defined by different unit cells, as illustrated in Figure 6, distinct optimized topologies are achieved, thereby confirming the non-uniqueness of the solution (Table 5). Conversely, combining the different optimized topologies achieves an identical periodic arrangement, resulting in an equally effective constitutive matrix, demonstrating the stability of the optimization process. These results are consistent with the principles of inverse homogenization design, highlighting that various repeating unit cells can display the same effective elastic properties, underscoring the significant impact of the initial material design on the optimized topology, as discussed by Sigmund (1994a). However, It is worth emphasizing the possibility of choosing more straightforward and more manufacturable alternatives among solutions with varying topological characteristics. Distinct microstructures featuring well-defined regions are achieved, resulting in optimized designs that exhibit minimal gray regions. Considering different initial material designs, this nearly uniform distribution of

solid-and-void materials contributes to the excellent performance of cellular materials obtained by the finite-volume theory modeling.

Table 5 – Impact of initial material design on the optimized topology with maximized shear modulus considering different repeat unit cells with the same periodic arrangement

Initial domain	Unit cell	3×3 cells	Effective properties
			$\mathbf{C}^* = \begin{bmatrix} 0.1833 & 0.1556 & 0 \\ & 0.1833 & 0 \\ \text{sym.} & & 0.1313 \end{bmatrix}$ $\mu^* = 0.1313$
			$\mathbf{C}^* = \begin{bmatrix} 0.1833 & 0.1556 & 0 \\ & 0.1833 & 0 \\ \text{sym.} & & 0.1313 \end{bmatrix}$ $\mu^* = 0.1313$
			$\mathbf{C}^* = \begin{bmatrix} 0.1833 & 0.1556 & 0 \\ & 0.1833 & 0 \\ \text{sym.} & & 0.1313 \end{bmatrix}$ $\mu^* = 0.1313$
			$\mathbf{C}^* = \begin{bmatrix} 0.1833 & 0.1556 & 0 \\ & 0.1833 & 0 \\ \text{sym.} & & 0.1313 \end{bmatrix}$ $\mu^* = 0.1313$
			$\mathbf{C}^* = \begin{bmatrix} 0.1833 & 0.1556 & 0 \\ & 0.1833 & 0 \\ \text{sym.} & & 0.1313 \end{bmatrix}$ $\mu^* = 0.1313$

Font: Author (2024).

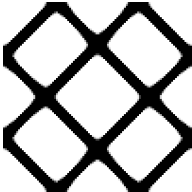
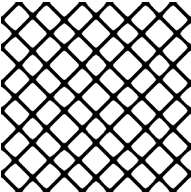
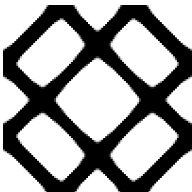
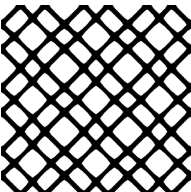
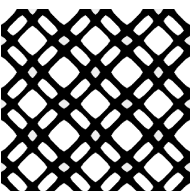
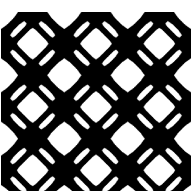
5.2.4 Influence of volume fraction constraint

The present study aims to evaluate the change in the optimized microstructural topologies with maximized shear modulus under varying solid material volume fraction constraints (ϑ). The results shown in Table 4 demonstrated that the material initial design strongly influences the outcome due to multiple local optima caused by the flexibility of the design domain. Therefore, the applications in this subsection are restricted to an initial design domain with a soft material

radius $R = 100/6$. The choice of this parameter was merely to avoid repeating results, and this selection does not lose generality.

Table 6 provides a visual representation of the optimized topologies, emphasizing the evolution of the material distribution within the design domain as the volume constraint is varied. As expected, increasing the volume of solid material leads to an optimized topology with enhanced shear stiffness, demonstrating a clear correlation between material usage and mechanical performance. This tendency indicates the importance of volume fraction in achieving desired structural properties in topology optimization.

Table 6 – Optimized topologies with maximized shear modulus, considering four levels of volume fraction constraints (ϑ)

ϑ	Unit cell	3×3 cells	Effective properties
30%			$\mathbf{C}^* = \begin{bmatrix} 0.0844 & 0.0793 & 0 \\ & 0.0844 & 0 \\ sym. & & 0.0716 \end{bmatrix}$ $\mu^* = 0.0716$
40%			$\mathbf{C}^* = \begin{bmatrix} 0.1292 & 0.1150 & 0 \\ & 0.1292 & 0 \\ sym. & & 0.1006 \end{bmatrix}$ $\mu^* = 0.1006$
50%			$\mathbf{C}^* = \begin{bmatrix} 0.1833 & 0.1556 & 0 \\ & 0.1833 & 0 \\ sym. & & 0.1313 \end{bmatrix}$ $\mu^* = 0.1313$
60%			$\mathbf{C}^* = \begin{bmatrix} 0.2559 & 0.2059 & 0 \\ & 0.2559 & 0 \\ sym. & & 0.1716 \end{bmatrix}$ $\mu^* = 0.1716$

Font: Author (2024).

5.3 Cellular Materials Bulk Modulus Maximization

The examples in this section focus on maximizing the material's bulk modulus under hydrostatic loading. Bulk modulus maximization has been extensively studied in scenarios involving filtering techniques, for instance, Sigmund (2000), Xia and Breitkopf (2015) and Collet et al. (2018). The bulk modulus property is essential in structural mechanics once it quantifies

the material's response to changes in volume. Characterization of materials concerning their compressive stiffness is fundamental in various engineering applications, such as designing load-bearing structures in civil engineering, designing implants and prosthetics in biomedical engineering, and enhancing vehicle safety and performance in automotive engineering, see for example Fardis (2009), Ratner et al. (2004) and Brach et al. (2022).

This study evaluates optimized microstructural topologies with maximized bulk modulus variation under different Poisson ratios and solid material volume fraction constraints. Additionally, the numerically obtained bulk modulus can be conveniently compared with the theoretical upper bound proposed by Hashin and Shtrikman (1963) to assess the efficiency of the optimization procedure. The analysis establishes a maximum limit $p_{max} = 10$ for the material penalization parameter, aiming for the solid-void pattern, because the optimality criteria algorithm has difficulty accommodating solid material for very low volume fraction constraints, particularly for bulk modulus maximization. Studies by Petersson and Sigmund (1998), Edwards et al. (2007), and Sridhara et al. (2022) have documented a similar approach and provided suitable solutions. Furthermore, after evaluating various possibilities, an initial design domain with a soft material radius $R = 100/4$ was chosen, as it provided reasonably optimized topologies, especially without filtering techniques.

5.3.1 Influence of Poisson's ratio

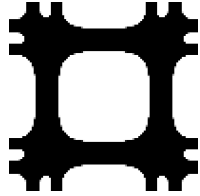
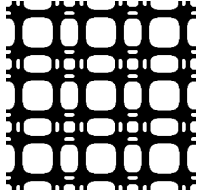
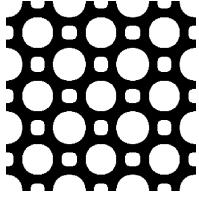
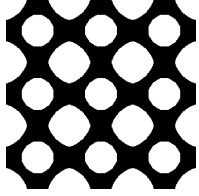
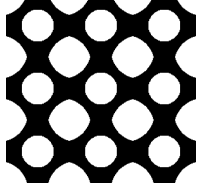
Classical elasticity theory predicts Poisson's ratio (ν) to range between -1 and $1/2$ due to the necessity for mechanical properties (Young, shear, and bulk moduli) to have positive values (Mott; Roland, 2009). However, the range of Poisson's ratios chosen in this application encompasses values corresponding to a material with zero Poisson's ratio ($\nu = 0$) to the limit of an incompressible material ($\nu = 1/2$). Designing materials and structures to achieve very low Poisson ratios, such as through metamaterial structures, becomes crucial in scenarios where minimizing lateral deformation is essential.

The present study aims to evaluate the change in the optimized microstructural topologies with maximized bulk modulus under varying Poisson's ratio of the solid material. It is important to emphasize that the change in shear modulus due to variations in Poisson's ratio is relatively small, which implies that the sensitivity of the shear modulus concerning Poisson's ratio is not significant enough to cause major changes in the material distribution during topology optimization. Conversely, the bulk modulus is highly sensitive to Poisson's ratio variations. When maximizing the bulk modulus, the optimization process must account for the variations in Poisson's more critically because they can substantially impact the resulting bulk modulus and affect the optimal material distribution to achieve the desired maximization.

Table 7 shows how variations in the solid material's Poisson ratio (ν) can significantly influence the final design of the optimal microstructure, considering a fixed solid volume fractions constraint of $\vartheta = 50\%$. As expected, the variation in the Poisson's ratio significantly influences

the material bulk modulus. Besides, low values of Poisson's ratio lead to more complexity-microstructural topologies. This tendency emphasizes the importance of accurately accounting for material properties in the optimization process, as these parameters directly impact the mechanical performance and feasibility of the resulting designs. By carefully selecting and adjusting the Poisson's ratio, engineers can tailor the optimization outcomes to match the desired material behavior better, ensuring more efficient structural solutions.

Table 7 – Optimized topologies with maximized bulk modulus for fixed solid volume fractions constraint of 50%, considering four values of Poisson's ratio (ν)

ν	Unit cell	3×3 cells	Effective properties
0			$\mathbf{C}^* = \begin{bmatrix} 0.3069 & 0.0158 & 0 \\ & 0.3069 & 0 \\ sym. & & 0.0195 \end{bmatrix}$ $\kappa^* = 0.1613$
1/6			$\mathbf{C}^* = \begin{bmatrix} 0.2210 & 0.1183 & 0 \\ & 0.2210 & 0 \\ sym. & & 0.0527 \end{bmatrix}$ $\kappa^* = 0.1697$
1/3			$\mathbf{C}^* = \begin{bmatrix} 0.2094 & 0.1428 & 0 \\ & 0.2094 & 0 \\ sym. & & 0.1080 \end{bmatrix}$ $\kappa^* = 0.1761$
1/2			$\mathbf{C}^* = \begin{bmatrix} 0.2190 & 0.1531 & 0 \\ & 0.2190 & 0 \\ sym. & & 0.1055 \end{bmatrix}$ $\kappa^* = 0.1860$

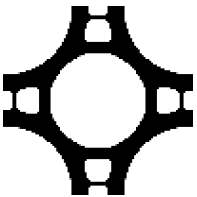
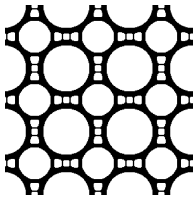
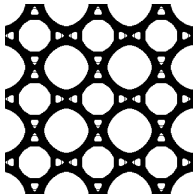
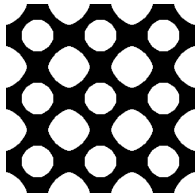
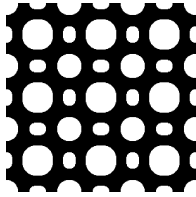
Font: Author (2024).

5.3.2 Influence of volume fraction constraint

The present study aims to evaluate the change in the optimized microstructural topologies with maximized bulk modulus under varying the solid volume fraction constraint of the solid material. Table 8 shows the optimized microstructural topologies with maximized bulk modulus for different solid volume fraction constraint levels. Even though one might expect a proportional variation in structure thickness with changes in available material, the optimization results show the emergence of distinct microstructural patterns. The smaller volume fractions can lead the

optimization process to converge to different local extremals. This phenomenon occurs because the reduced material availability restricts the design space, potentially causing difficulty for the algorithm in determining suboptimal configurations. Consequently, the final microstructures may differ significantly from those obtained with higher material fractions, emphasizing the sensitivity of the optimization process to volume constraints.

Table 8 – Optimized topologies with maximized bulk modulus, considering four levels of volume fraction constraints (ϑ)

ϑ	Unit cell	3×3 cells	Effective properties
30%			$\mathbf{C}^* = \begin{bmatrix} 0.0971 & 0.0734 & 0 \\ & 0.0971 & 0 \\ sym. & & 0.0084 \end{bmatrix}$ $\kappa^* = 0.0853$
40%			$\mathbf{C}^* = \begin{bmatrix} 0.1483 & 0.1041 & 0 \\ & 0.1483 & 0 \\ sym. & & 0.0510 \end{bmatrix}$ $\kappa^* = 0.1262$
50%			$\mathbf{C}^* = \begin{bmatrix} 0.2074 & 0.1407 & 0 \\ & 0.2074 & 0 \\ sym. & & 0.1088 \end{bmatrix}$ $\kappa^* = 0.1741$
60%			$\mathbf{C}^* = \begin{bmatrix} 0.3430 & 0.1331 & 0 \\ & 0.3430 & 0 \\ sym. & & 0.0746 \end{bmatrix}$ $\kappa^* = 0.2380$

Font: Author (2024).

5.3.3 Comparison with the Hashin-Shtrikman upper bound

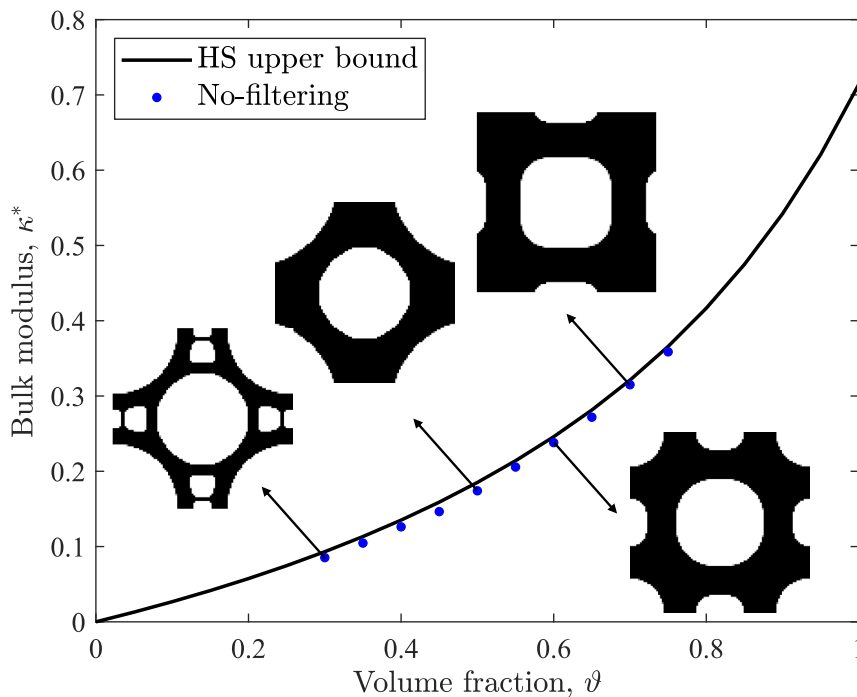
This study aims to evaluate the change in the optimized microstructure under varying solid volume fraction constraints, precisely at 30% to 75% and compare with the theoretical Hashin-Shtrikman (HS) upper bound (Hashin; Shtrikman, 1963). The results are produced with no-filtering scenarios, and those achieved employing sensitivity and density filtering techniques (Sigmund, 2007; Bruns; Tortorelli, 2001; Bourdin, 2001). Although the Hashin–Shtrikman bounds define a range of admissible values in which the composite exhibits isotropy, several researchers, such as Huang et al. (2011), Collet et al. (2018), and Liu et al. (2021), among others,

have observed that the maximum bulk modulus of orthotropic materials with square symmetry closely approximates the HS upper bound. According to Torquato et al. (1998), in the scenario where the elastic properties of one phase are equal to zero (voids), the HS upper bound in the plane stress state can be expressed by:

$$\kappa^{HS} = \frac{\vartheta \kappa_0 \mu_0}{(1 - \vartheta) \kappa_0 + \mu_0}, \quad (49)$$

where κ_0 and μ_0 are the solid material's bulk and shear moduli, respectively.

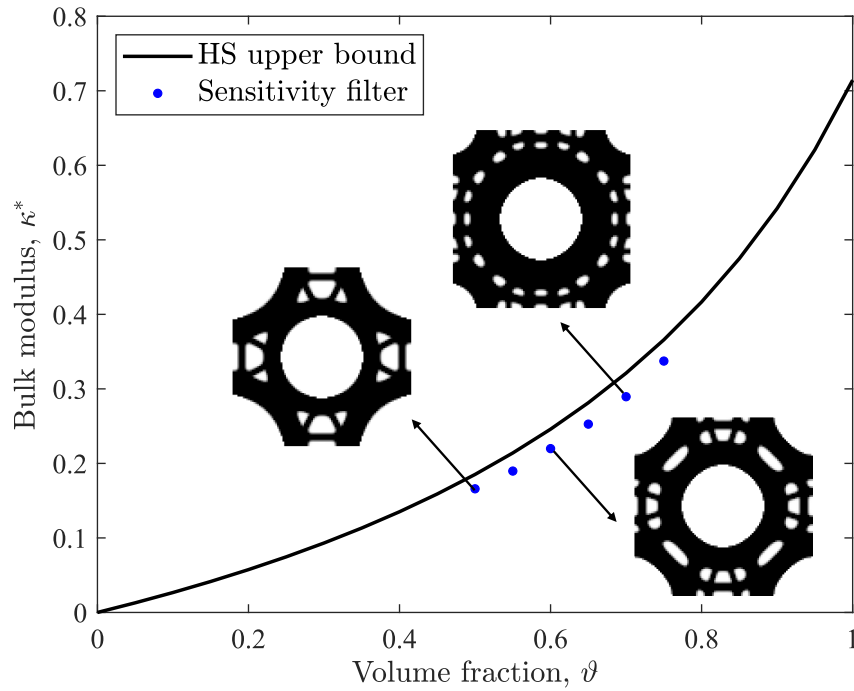
Figure 15 – Maximized bulk modulus for different optimized topologies and the HS upper bound as a function of the volume fraction constraint (ϑ), considering no-filtering scenario



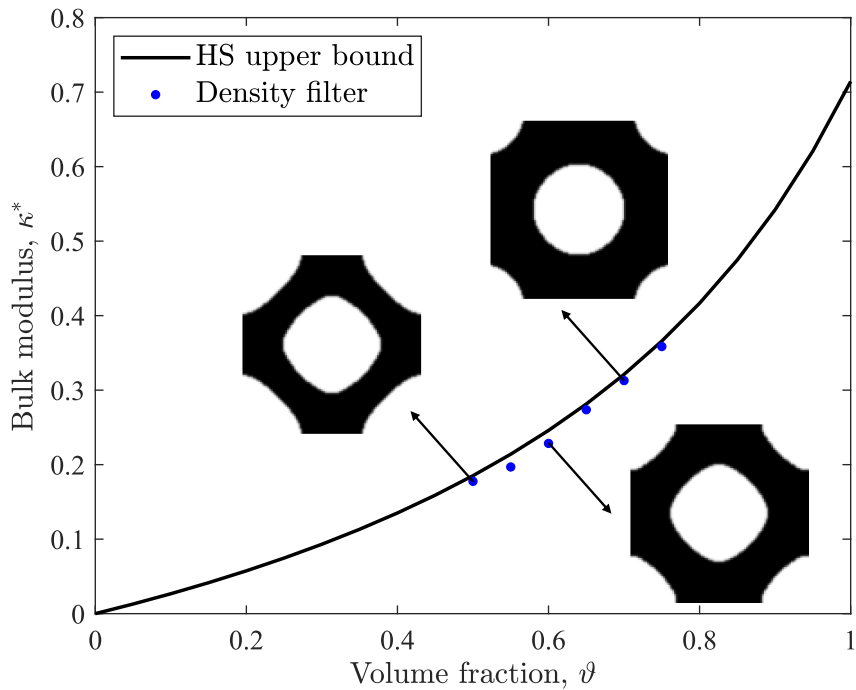
Font: Author (2024).

Figure 15 illustrates the maximized bulk modulus of various optimized topologies as a function of the volume fraction constraints, comparing them to the theoretical Hashin-Shtrikman (HS) upper bound. As observed, topology optimization produces materials' designs with an effective bulk modulus that satisfies the HS upper bound. This illustration emphasizes the efficiency of finite-volume theory in searching for optimized topologies with maximized bulk moduli without filtering techniques. The method produces well-defined optimized topologies for a significant range of solid volume fraction constraints. The finite-volume theory also allows for precise control over material properties and distribution, resulting in designs that combine high stiffness and material efficiency.

Figure 16 – Maximized bulk modulus for different optimized topologies and the HS upper bound as a function of the volume fraction constraint ϑ , considering filtering applications



(a) Sensitivity filter analysis



(b) Density filter analysis

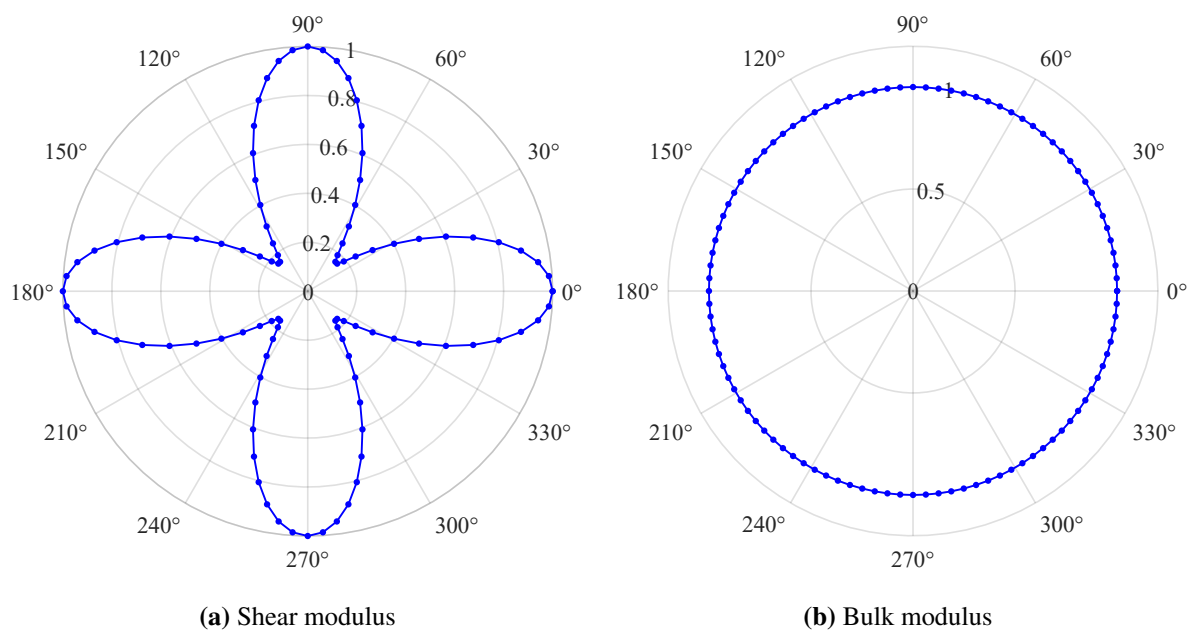
Font: Author (2024).

Figure 16 illustrates the maximized bulk modulus for different optimized topologies and the HS upper bound, varying the volume fraction constraint and utilizing sensitivity and density filtering, respectively, with a filter radius $r_{fl} = 1.5$. The final topologies resulting from sensitivity

filtering exhibit greater complexity than those from density filtering, indicating limitations from a material manufacturing point of view. Additionally, when applying a volume fraction constraint less than 50%, the algorithm converges to a solution featuring a substantial gray region for both filtering strategies.

Furthermore, employing the finite-volume theory without filtering techniques for material design results in higher effective elastic properties of the material (Figure 15). This aspect emphasizes that employing the finite-volume theory significantly contributes to topology optimization, providing robust and efficient solutions without the added complexity of filtering techniques.

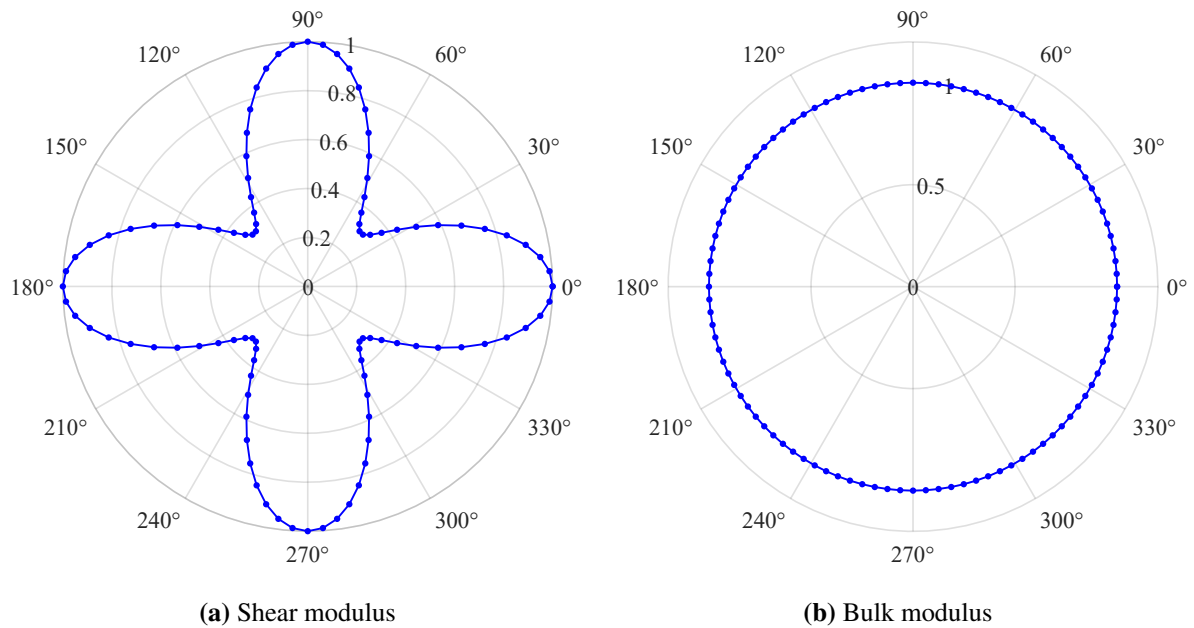
Figure 17 – Normalized macroscopic elastic modulus for rotated axes relative to the material principal axes: shear modulus maximization



Font: Author (2024).

It is essential to highlight that the topology optimization process applied to materials design with periodic microstructures, considering a repeating square unit cell, leads to an optimized topology that exhibits a high degree of material anisotropy due to the symmetry of the unit cell. Figures 17-18 illustrate normalized macroscopic elastic modulus for rotated axes relative to the material principal axes for shear and bulk moduli maximization, respectively, considering a solid volume fraction constraint of 50%. The results in Figures 17(a)-18(a) suggest that the optimization process maximizes the shear modulus in the material principal axes (0 and 90 degrees) and considerably minimizes it at a 45-degree angle. For this reason, the maximized shear modulus violates the HS upper bound in the case of orthotropic materials. On the other hand, despite the optimized topology displaying a high degree of anisotropy, the bulk modulus remained invariant with the rotation of the reference axes relative to the material principal axes, as illustrated in Figures 17(b)-18(b). This feature enables the maximized bulk modulus to stay within the HS upper bound without violation.

Figure 18 – Normalized macroscopic elastic modulus for rotated axes relative to the material principal axes: bulk modulus maximization



Font: Author (2024).

If a practical application demands material isotropy, material designers can consider the incorporation of an isotropy constraint within the problem's formulation for topology optimization as suggested by Radman et al. (2013). However, it requires implementing a more robust algorithm for design variable updates, such as the method of moving asymptotes (MMA) developed by Svanberg (1987). It is known, through the study conducted by Khatam et al. (2009), that circular and hexagonal holes arranged in hexagonal arrays produce transversely isotropic homogenized moduli, with the plane of isotropy coinciding with the sheet's plane. A challenge for future research is to evaluate whether modeling a hexagonal periodic cell can generate transversely isotropic optimized topologies without additional isotropy constraints.

5.4 Cellular Materials with Negative Poisson's ratio

Researchers have recently focused on engineered materials with non-conventional properties, showing significant potential for innovation in various industrial sectors (Andreassen et al., 2014). A fascinating class of these materials, named auxetic materials, stands out for their unique mechanical properties compared to natural materials. These materials are designed at the microstructural level to exhibit distinctive and counter-intuitive behavior due to their internal geometry and spatial distributions (Kelkar et al., 2020). Besides, they exhibit exotic functionalities, such as pattern and shape transformations in response to mechanical forces, unidirectional guiding of motion and waves, and reprogrammable stiffness or dissipation (Bertoldi et al., 2017). One practical application of auxetic materials is their potential use in designing crashworthiness devices for automotive or aerospace engineering, as discussed in Liu (2006).

The application of topology optimization to design structural materials is an active field of research. For example, Andreassen et al. (2014) developed a procedure based on topology optimization to create manufacturable extraordinary elastic materials with a negative Poisson's ratio, employing the finite element method and filtering technique. Herein, the finite-volume theory without filtering techniques or image processing is employed to find the optimized microstructural topology of auxetic materials with a negative Poisson ratio.

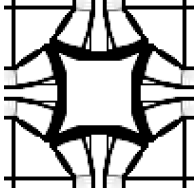
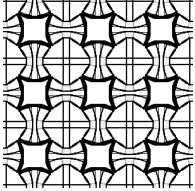
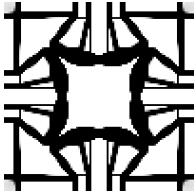
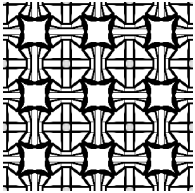
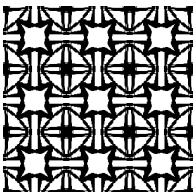
5.4.1 Influence of volume fraction constraint

This study aims to demonstrate the change in the final design of auxetic materials with varying volume fraction constraints (ϑ), considering an initial design domain with a soft material radius $R = 100/6$. The material penalization parameter assigned to the model ranged from $p = 0$ to $p_{max} = 3$, with a unit increment in the continuation method and the OC move limit $m = 0.1$ strategic choice to stabilize the algorithm, improving convergence performance. Optimized topologies in Tables 9-10 align with the auxetic behavior by employing slender components interconnected via compliant joints (compliant mechanisms), resulting in lateral expansion when subjected to axial stretching. Compliant mechanisms are widely employed in several microelectromechanical systems (MEMS) applications, for example, airbag acceleration sensors (Sigmund, 1997b).

The optimization process consistently yields re-entrant characteristics across all design scenarios, with progressively thinner joints as the solid volume fraction constraint decreases, enhancing the negative Poisson's ratio behavior. However, these slender joints pose manufacturing challenges and may contribute to fatigue and structural failure concerns. Additionally, the choice of the numerical parameter β can influence the definition of the optimized topology, in which higher values lead to results with an even more pronounced negative Poisson's ratio but also result in topologies featuring thinner and more delicate bars. The design process must consider this trade-off between achieving the desired mechanical properties and maintaining structural integrity. Implementing these parameters needs to be balanced to ensure manufacturability while achieving the intended mechanical performance.

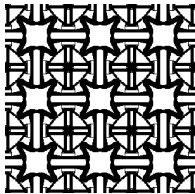
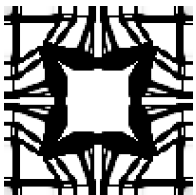
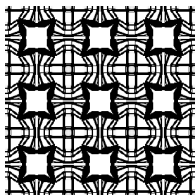
Finally, the results demonstrate the effectiveness of the finite-volume theory when applied to material design through topology optimization methods without filtering techniques. This approach showcases its capabilities in generating meaningful and efficient designs, offering valuable insights into the optimization process for various material properties and characteristics. Furthermore, it highlights the robustness and versatility of this methodology, emphasizing its applicability in a range of engineering and scientific domains. Overall, these findings advance materials science and design, showcasing the utility of the finite-volume theory as a valuable alternative tool for innovative and optimized material development.

Table 9 – Optimized topologies with negative Poisson’s ratio for a fixed $\beta = 0.8$, considering four levels of volume fraction constraints (ϑ)

ϑ	Unit cell	3×3 cells	Effective properties
30%			$\mathbf{C}^* = \begin{bmatrix} 0.0547 & -0.0448 & 0 \\ & 0.0547 & 0 \\ sym. & & 0.0005 \end{bmatrix}$ $\nu^* = -0.8190$
40%			$\mathbf{C}^* = \begin{bmatrix} 0.0754 & -0.0575 & 0 \\ & 0.0754 & 0 \\ sym. & & 0.0028 \end{bmatrix}$ $\nu^* = -0.7626$
50%			$\mathbf{C}^* = \begin{bmatrix} 0.0846 & -0.0636 & 0 \\ & 0.0846 & 0 \\ sym. & & 0.0087 \end{bmatrix}$ $\nu^* = -0.7518$
60%			$\mathbf{C}^* = \begin{bmatrix} 0.0906 & -0.0715 & 0 \\ & 0.0906 & 0 \\ sym. & & 0.0162 \end{bmatrix}$ $\nu^* = -0.7892$

Font: Author (2024).

Table 10 – Optimized topologies with negative Poisson’s ratio for a fixed volume fraction constraints of 50%, considering other two values of β parameter

β	Unit cell	3×3 cells	Effective properties
0.7			$\mathbf{C}^* = \begin{bmatrix} 0.0825 & -0.0626 & 0 \\ & 0.0825 & 0 \\ sym. & & 0.0051 \end{bmatrix}$ $\nu^* = -0.7588$
0.9			$\mathbf{C}^* = \begin{bmatrix} 0.0955 & -0.0751 & 0 \\ & 0.0955 & 0 \\ sym. & & 0.0040 \end{bmatrix}$ $\nu^* = -0.7864$

Font: Author (2024).

6 CONCLUSIONS

This work introduced an innovative approach that synthesized principles from the standard or zeroth-order formulation of finite-volume theory, homogenization methods, and density-based topology optimization to design high-performance periodic cellular materials within an efficient computational code. The design procedure was formulated as a topology optimization problem, with the objective function aiming to maximize or minimize a linear combination of the components of the effective constitutive matrix. This combination was strategically chosen to yield macroscopic material parameters such as the shear/bulk moduli and the negative Poisson's ratio characteristic of auxetic materials.

A numerical homogenization procedure based on strain energy equivalence and the classical micromechanics mean-field theory approaches was developed and included in the TopMatFVT, aiming to evaluate the effective elastic properties of cellular materials as an intermediate stage of the optimization procedure. Substantial reductions in computer processing time and storage demands were achieved by implementing matrix vectorization techniques in the Matlab programming language to solve numerical models, based on the works by Andreassen et al. (2011) and Xia and Breitkopf (2015).

Several numerical examples were investigated to explore optimized microstructural topology's behavior concerning numerical model parameters and those directly relevant to engineering applications. These parameters included the material interpolation methods SIMP and RAMP, the continuation method of the material penalization parameter, the initial material design, the Poisson's ratio, and the selected material volume fraction constraint. The analyzed applications demonstrated that the finite-volume theory, which does not require additional restrictions on the problem, such as filtering techniques, combined with the topology optimization strategy, is a valuable tool for aiding the design of periodic cellular materials.

Despite requiring more iterations than SIMP, the RAMP method has displayed better numerical stability during the material penalization process and presented results with less complex topologies, simpler designs, thicker bars, and smaller perimeters (cut path), which are essential aspects of a material from a manufacturing point of view. Another crucial characteristic observed is the strong dependence on the chosen initial material design when employing the gradient-based approach, requiring prior knowledge of the final design desired by material designers. On the other hand, selecting an initial material design characterized by different repeat unit cells representing the same initial periodic arrangement leads to distinct optimized topologies but with the same final periodic arrangement and effective material properties.

The results of optimized topologies with maximized shear or bulk modulus concerning solid volume fraction constraints reveal distinct microstructural patterns. As expected, the increase in final solid material results in an optimized topology with higher stiffness. Besides, the variation in Poisson's ratio significantly influences the material bulk modulus, where low

values can lead to more complex microstructural topologies. This emphasizes the importance of accurately accounting for material properties in optimization.

The orthotropic material's effective bulk modulus values for the range of solid volume fraction constraints analyzed closely approximate the theoretical Hashin-Shtrikman upper bound as an essential result, given that no filters were employed to regularize the solution. In the negative Poisson's ratio study, the optimization results produced optimized topologies with re-entrant features in all design scenarios. As the solid volume fraction constraint decreases, the joints become thinner, enhancing the negative Poisson's ratio behavior. However, fragile joints can pose challenges in manufacturing cellular materials. They may lead to fatigue and structural failure, demanding a delicate balance between the choice of engineering parameter and the desired sophistication of the optimized topology.

Finally, the optimized topologies derived from the approach developed in this dissertation suggest an arrangement that will help material designers and should be viewed as something other than immediately manufacturable solutions. Refining the response or treatment of "jagged" edges necessitates smoothing strategies for these regions. This smoothing process corresponds to a necessary step in the design for the final generation of manufacturable topologies, different from the use of filters employed in the context of finite element analysis to avoid the occurrence of checkerboard patterns. Therefore, the results presented are expected to inspire researchers to develop innovative microstructures of cellular materials, especially without filters.

Further Works

As a continuation of the work presented in this dissertation, one may consider the following subjects:

- The effectiveness of a gradient-based algorithm is highly dependent on the initial material distribution within the design domain. It is crucial to carefully consider the starting design to ensure optimal results. A comparative study with alternative strategies, such as evolutionary methods, is recommended. These methods offer distinct advantages, including different convergence behaviors and the ability to escape local extremal, providing a broader perspective on achieving optimal structural designs;
- To employ the TopMatFVT to design efficient materials with prescribed elastic properties using an inverse homogenization approach. This strategy focuses on optimizing the material distribution to achieve the desired material properties, guided by the constitutive matrix of the target material;
- A periodic hexagonal unit cell should be modeled and incorporated into the TopMatFVT. Conduct the analyses to verify if the optimal periodic microstructures present the behavior of transversely isotropic materials. This modeling is justified due to the limitations of the

optimality criteria (OC) method, which is effective only for a single constraint, and the method of moving asymptotes (MMA) requires the imposition of additional constraints to produce optimized topologies with transversely isotropic materials;

- Implementing a model into TopMatFVT that penalizes intermediate densities for bi-materials (solid-solid) will enable the topology optimization of reinforced composite materials and expand the range of practical applications that can be simulated;
- An extension from the two dimensions to the three dimensions domain is recommended. This extension can facilitate a more authentic exploration of materials with more complex periodic microstructures.

REFERENCES

- Aboudi, J.; Arnold, S.; Bednarczyk, B. *Micromechanics of Composite Materials: A Generalized Multiscale Analysis Approach*. : Elsevier Science, 2012. 984 p.
- Aboudi, J.; Pindera, M.-J.; Arnold, S. Higher-order theory for functionally graded materials. *Composites Part B: Engineering*, v. 30, n. 8, p. 777–832, 1999.
- Aboudi, J.; Pindera, M.-J.; Arnold, S. Linear thermoelastic higher-order theory for periodic multiphase materials. *Journal of Applied Mechanics-transactions of The Asme*, v. 68, 2001.
- Aboudi, J.; Pindera, M.-J.; Arnold, S. High-fidelity generalization method of cells for inelastic periodic multiphase materials. *NASA Technical Memorandum 2002-211469, NASA-Glenn Research Center*, 2002.
- Alvarez, H.; Zambrano, H.; Silva, O. Influence of density-based topology optimization parameters on the design of periodic cellular materials. *Materials*, v. 12, 11 2019.
- Andreassen, E.; Clausen, A.; Schevenels, M.; Lazarov, B. S.; Sigmund, O. Efficient topology optimization in matlab using 88 lines of code. *Structural and Multidisciplinary Optimization*, v. 43, p. 1–16, 1 2011.
- Andreassen, E.; Lazarov, B. S.; Sigmund, O. Design of manufacturable 3d extremal elastic microstructure. *Mechanics of Materials*, Elsevier B.V., v. 69, p. 1–10, 2014.
- Araujo, M. V. O. *Finite-Volume Theory Applied to Topological Optimization of Continuous Elastic Structures*. 162 p. Thesis (Master in Civil Engineering) — Federal University of Alagoas, 2018.
- Araujo, M. V. O. *Energy Analysis of the Generalized Finite-volume Theory and Application to Topology Optimization with Compliance Minimization*. 124 p. Thesis (Doctoral in Civil Engineering) — Federal University of Alagoas, 2022.
- Araujo, M. V. O.; Lages, E. N.; Cavalcante, M. A. A. Checkerboard free topology optimization for compliance minimization applying the finite-volume theory. *Mechanics Research Communications*, v. 108, p. 103581, 2020a.
- Araujo, M. V. O.; Lages, E. N.; Cavalcante, M. A. A. Checkerboard-free topology optimization for compliance minimization of continuum elastic structures based on the generalized finite-volume theory. *Latin American Journal of Solids and Structures*, Brazilian Association of Computational Mechanics, v. 17, p. 1–21, 2020b.
- Araujo, M. V. O.; Lages, E. N.; Cavalcante, M. A. A. Energy analysis of continuum elastic structures by the generalized finite-volume theory. *Acta Mechanica*, Springer, v. 232, p. 4625–4643, 11 2021.
- Bansal, Y.; Pindera, M.-J. Efficient reformulation of the thermoelastic higher-order theory for functionally graded materials. *Journal of Thermal Stresses*, v. 26, p. 1055–1092, 11 2003.
- Bansal, Y.; Pindera, M.-J. A second look at the higher-order theory for periodic multiphase materials. *Journal of Applied Mechanics*, v. 72, n. 2, p. 177–195, 2005.

- Bansal, Y.; Pindera, M.-J. Finite-volume direct averaging micromechanics of heterogeneous materials with elastic–plastic phases. *International Journal of Plasticity*, v. 22, n. 5, p. 775–825, 2006.
- Bendsøe, M. Optimal shape design as a material distribution problem. *Structural Optimization 1*, v. 1, p. 193–202, 1989.
- Bendsøe, M. P.; Kikuchi, N. Generating optimal topologies in structural design using a homogenization method. *Computer Methods in Applied Mechanics and Engineering*, v. 71, p. 197–224, 1988.
- Bendsøe, M. P.; Sigmund, O. Material interpolation schemes in topology optimization. *Archive of Applied Mechanics*, v. 69, p. 635–654, 1999.
- Bendsøe, M. P.; Sigmund, O. *Topology Optimization: Theory, Methods and Applications*. Berlin: Springer Berlin, 2003. 370 p.
- Bensoussan, A.; Lions, J.-L.; Papanicolau, G. *Asymptotic analysis for periodic structures*. : Elsevier, 1978.
- Bertoldi, K.; Vitelli, V.; Christensen, J.; Hecke, M. Flexible mechanical metamaterials. *Nature Reviews Materials*, v. 2, p. 17066, 10 2017.
- Bose, S.; Ke, D.; Sahasrabudhe, H.; Bandyopadhyay, A. Additive manufacturing of biomaterials. *Progress in Materials Science*, v. 93, p. 45–111, 2018.
- Bourdin, B. Filters in topology optimization. *International Journal for Numerical Methods in Engineering*, v. 50, p. 2143 – 2158, 03 2001.
- Brach, M.; Mason, J.; Brach, R. *Vehicle Accident Analysis and Reconstruction Methods*. : SAE International, 2022.
- Bruns, T.; Tortorelli, D. Topology optimization of non-linear structures and compliant mechanisms. *Computer Methods in Applied Mechanics and Engineering*, v. 190, p. 3443–3459, 03 2001.
- Cavalcante, M. A.; Marques, S. P.; Pindera, M. J. Parametric formulation of the finite-volume theory for functionally graded materials - part i: Analysis. *Journal of Applied Mechanics, Transactions ASME*, v. 74, p. 935–945, 9 2007.
- Cavalcante, M. A.; Marques, S. P.; Pindera, M. J. Parametric formulation of the finite-volume theory for functionally graded materials - part ii: Numerical results. *Journal of Applied Mechanics, Transactions ASME*, v. 74, p. 946–957, 9 2007.
- Cavalcante, M. A.; Pindera, M. J. Generalized finite-volume theory for elastic stress analysis in solid mechanics-part i: Framework. *Journal of Applied Mechanics, Transactions ASME*, v. 79, 2012a.
- Cavalcante, M. A.; Pindera, M. J.; Khatam, H. Finite-volume micromechanics of periodic materials: Past, present and future. *Composites Part B: Engineering*, v. 43, p. 2521–2543, 9 2012.
- Cavalcante, M. A. A. *Modelling of the transient thermo-mechanical behavior of composite material structures by the finite-volume theory*. 130 p. Thesis (Master in Civil Engineering) — Federal University of Alagoas, 2006.

Chen, H. et al. Porous scaffold design for additive manufacturing in orthopedics: A review. *Frontiers in Bioengineering and Biotechnology*, Frontiers Media S.A., v. 8, 6 2020.

Christensen, P. W.; Klarbring, A. *An Introduction to Structural Optimization*. Netherlands: Springer Science & Business Media, 2008.

Christoff, B. G.; Brito-Santana, H.; Cardoso, E. L.; Abot, J. L.; Tita, V. A topology optimization approach used to assess the effect of the matrix impregnation on the effective elastic properties of a unidirectional carbon nanotube bundle composite. *Materials Today: Proceedings*, v. 8, p. 789–803, 2019.

Collet, M.; Noël, L.; Bruggi, M.; Duysinx, P. Topology optimization for microstructural design under stress constraints. *Structural and Multidisciplinary Optimization*, Springer Verlag, v. 58, p. 2677–2695, 12 2018.

Deaton, J. D.; Grandhi, R. V. A survey of structural and multidisciplinary continuum topology optimization: Post 2000. *Structural and Multidisciplinary Optimization*, v. 49, p. 1–38, 1 2013.

Díaz, A.; Sigmund, O. Checkerboard patterns in layout optimization. *Structural Optimization*, v. 10, p. 40–45, 08 1995.

Drago, A.; Pindera, M. J. Micro-macromechanical analysis of heterogeneous materials: Macroscopically homogeneous vs periodic microstructures. *Composites Science and Technology*, v. 67, p. 1243–1263, 5 2007.

Díaz, R. G.; Bravo-Castillero, J.; Sabina, F. Closed-form expressions for the effective coefficients of fibre-reinforced composite with transversely isotropic constituents-II. elastic and hexagonal symmetry. *Journal of the Mechanics and Physics of Solids*, v. 49, p. 1445–1462, 07 2001.

Edwards, C.; Kim, H.; Budd, C. An evaluative study on eso and simp for optimising a cantilever tie—beam. *Structural and Multidisciplinary Optimization*, Springer Verlag, v. 34, n. 5, p. 403–414, 2007.

Escarpini Filho, R. S. *Analysis of Structures of Linear Viscoelastic Composite Materials using Finite Volume Theory*. 86 p. Thesis (Master in Civil Engineering) — Federal University of Alagoas, 2010.

Escarpini Filho, R. S.; Almeida, F. P. A. Reinforced masonry homogenization by the finite-volume direct averaging micromechanics—FVDAM. *Composite Structures*, v. 320, p. 117185, 05 2023.

Escarpini Filho, R. S.; Marques, S. A model for evaluation of effective thermal conductivity of periodic composites with poorly conducting interfaces. *Materials Research*, v. 17, p. 1344–1355, 09 2014.

Fardis, M. N. *Seismic Design, Assessment and Retrofitting of Concrete Buildings*. : Springer, 2009.

Gattu, M. *Parametric finite volume theory for periodic heterogeneous materials*. Thesis (MS Thesis, Civil Engineering Department) — University of Virginia, Charlottesville, 2007.

Gattu, M.; Khatam, H.; Drago, A. S.; Pindera, M. J. Parametric finite-volume micromechanics of uniaxial continuously-reinforced periodic materials with elastic phases. *Journal of Engineering Materials and Technology*, American Society of Mechanical Engineers (ASME), v. 130, p. 0310151–03101515, 2008.

- Guedes, J. M.; Kikuchi, N. Preprocessing and postprocessing for materials based on the homogenization method with adaptive finite element methods. *Computer Methods in Applied Mechanics and Engineering*, v. 83, p. 143–198, 1990.
- Hashin, Z.; Shtrikman, S. A variational approach to the theory of the elastic behavior of multiphase materials. *Journal of the Mechanics and Physics of Solids*, v. 11, n. 2, p. 127–140, 1963.
- Hill, R. Elastic properties of reinforced solids: some theoretical principles. *Journal of The Mechanics and Physics of Solids*, v. 11, p. 357–372, 1963.
- Hiremath, S. Design and analysis of 3d printed perforated sheet metal testing and manufacturing. 11 2020.
- Hori, M.; Nemat-Nasser, S. On two micromechanics theories for determining micro–macro relations in heterogeneous solids. *Mechanics of Materials*, v. 31, n. 10, p. 667–682, 1999.
- Huang, X.; Radman, A.; Xie, Y. M. Topological design of microstructures of cellular materials for maximum bulk or shear modulus. *Computational Materials Science*, v. 50, p. 1861–1870, 4 2011.
- Huang, X.; Xie, Y. A further review of eso type methods for topology optimization. *Structural and Multidisciplinary Optimization*, v. 41, p. 671–683, 05 2010.
- Hyer, M.; Waas, A. *Micromechanics of Linear Elastic Continuous Fiber Composites*. : Elsevier, 2017.
- Jang, G.-W. et al. Checkerboard-free topology optimization using non-conforming finite elements. *International Journal for Numerical Methods in Engineering*, v. 57, p. 1717–1735, 01 2003.
- Kelkar, P. et al. Cellular auxetic structures for mechanical metamaterials: A review. *Sensors*, v. 20, p. 3132, 06 2020.
- Khatam, H.; Chen, L.; Pindera, M.-J. Elastic and plastic response of perforated metal sheets with different porosity architectures. *Journal of Engineering Materials and Technology*, v. 131, p. 0310151–03101514, 07 2009.
- Khatam, H.; Pindera, M.-J. Parametric finite-volume micromechanics of periodic materials with elastoplastic phases. *International Journal of Plasticity*, v. 25, n. 7, p. 1386–1411, 2009.
- Khatam, H.; Pindera, M.-J. Thermo-elastic moduli of periodic multilayers with wavy architectures. *Composites Part B: Engineering*, v. 40, n. 1, p. 50–64, 2009.
- Kumar, P. Honeytop90: A 90-line matlab code for topology optimization using honeycomb tessellation. *Optimization and Engineering*, v. 24, p. 1–28, 04 2022.
- Lages, E. N.; Marques, S. P. C. Thermoelastic homogenization of periodic composites using an eigenstrain-based micromechanical model. *Applied Mathematical Modelling*, v. 85, p. 1–18, 2020.
- Liu, P.; Yan, Y.; Zhang, X.; Luo, Y.; Kang, Z. Topological design of microstructures using periodic material-field series-expansion and gradient-free optimization algorithm. *Materials & Design*, v. 199, p. 109437, 2021.

Liu, Q. Literature review: Materials with negative poisson's ratios and potential applications to aerospace and defence. *Aust. Gov. Dep. Def.*, 01 2006.

Michell, A. The limits of economy of material in frame-structures. *The London, Edinburgh, and Dublin Philosophical Magazine and Journal of Science*, Taylor & Francis, v. 8, n. 47, p. 589–597, 1904.

Mironovs, V.; Tatarinov, A.; Gorbačova, S. Expanding application of perforated metal materials in construction and architecture. *IOP Conference Series: Materials Science and Engineering*, v. 251, p. 012027, 10 2017.

Mott, P. H.; Roland, C. M. Limits to poisson's ratio in isotropic materials. *Phys. Rev. B*, American Physical Society, v. 80, p. 132104, Oct 2009.

Moukalled, F.; Mangani, L.; Darwish, M. *The Finite Volume Method in Computational Fluid Dynamics: An Advanced Introduction with OpenFOAM® and Matlab®*. 2015. v. 113. 791 p. ISBN 978-3-319-16873-9.

Nemat-Nasser, S.; Iwakuma, T.; Hejazi, M. On composites with periodic structure. *Mechanics of Materials*, v. 1, n. 3, p. 239–267, 1982.

Nemat-Nasser, S.; Taya, M. On effective moduli of an elastic body containing periodically distributed voids. *Quarterly of Applied Mathematics*, v. 39, 04 1981.

Neves, M.; Rodrigues, H.; Guedes, J. Optimal design of periodic linear elastic microstructures. *Computers Structures*, v. 76, n. 1, p. 421–429, 2000.

Petersson, J.; Sigmund, O. Slope constrained topology optimization. *International Journal for Numerical Methods in Engineering*, v. 41, n. 8, p. 1417–1434, 1998.

Pindera, M. J.; Khatam, H.; Drago, A. S.; Bansal, Y. Micromechanics of spatially uniform heterogeneous media: A critical review and emerging approaches. *Composites Part B: Engineering*, v. 40, p. 349–378, 7 2009.

Qu, J.; Cherkaoui, M. Fundamentals of micromechanics of solids. In: . 2006.

Radman, A.; Huang, X.; Xie, Y. Topological optimization for the design of microstructures of isotropic cellular materials. *Engineering Optimization*, Taylor & Francis, v. 45, n. 11, p. 1331–1348, 2013.

Ramírez-Torres, A.; Penta, R.; Grillo, A. Effective properties of hierarchical fiber-reinforced composites via a three-scale asymptotic homogenization approach. *Mathematics and Mechanics of Solids*, v. 24, p. 108128651984768, 05 2019.

Ratner, B.; Hoffman, A.; Schoen, F.; Lemons, J. *Biomaterials Science: An Introduction to Materials in Medicine*. : Elsevier Science, 2004.

Rodríguez-Ramos, R.; Sabina, F. J.; Guinovart-Díaz, R.; Bravo-Castillero, J. Closed-form expressions for the effective coefficients of a fiber-reinforced composite with transversely isotropic constituents – i. elastic and square symmetry. *Mechanics of Materials*, v. 33, n. 4, p. 223–235, 2001.

Rojas-Labanda, S.; Stolpe, M. Automatic penalty continuation in structural topology optimization. *Structural and Multidisciplinary Optimization*, v. 52, 07 2015.

Rozvany, G. I. N.; Bendsoe, M. P.; Kirsch, U. Layout Optimization of Structures. *Applied Mechanics Reviews*, v. 48, n. 2, p. 41–119, 02 1995.

Rozvany, G. I. N.; Zhou, M.; Birker, T. Generalized shape optimization without homogenization. *Structural optimization*, v. 4, p. 250–252, 1992.

Sigmund, O. *Design of Material Structures Using Topology Optimization*. 109 p. Thesis — Technical University of Denmark, 01 1994a.

Sigmund, O. Materials with prescribed constitutive parameters: An inverse homogenization problem. *International Journal of Solids and Structures*, v. 31, n. 17, p. 2313–2329, 1994b.

Sigmund, O. On the design of compliant mechanisms using topology optimization*. *Mechanics of Structures and Machines*, Taylor & Francis, v. 25, n. 4, p. 493–524, 1997b.

Sigmund, O. A new class of extremal composites. *Journal of the Mechanics and Physics of Solids*, Elsevier, v. 48, n. 2, p. 397–428, 2000.

Sigmund, O. Morphology-based black and white filters for topology optimization. *Structural and Multidisciplinary Optimization*, v. 33, p. 401–424, 4 2007.

Sigmund, O.; Maute, K. Topology optimization approaches a comparative review. *Structural and Multidisciplinary Optimization*, v. 48, 12 2013.

Sigmund, O.; Petersson, J. Numerical instabilities in topology optimization: A survey on procedures dealing with checkerboards, mesh-dependencies and local minima. *Structural Optimization*, v. 16, p. 68–75, 08 1998.

Sigmund, O.; Torquato, S. Design of materials with extreme thermal expansion using a three-phase topology optimization method. *Journal of the Mechanics and Physics of Solids*, Elsevier, v. 45, n. 6, p. 1037–1067, 1997a.

Sridhara, S.; Chandrasekhar, A.; Suresh, K. A generalized framework for microstructural optimization using neural networks. *Materials & Design*, v. 223, p. 111213, 2022.

Stolpe, M.; Svanberg, K. An alternative interpolation scheme for minimum compliance topology optimization. *Struct Multidisc Optim*, Springer-Verlag, v. 22, p. 116–124, 2001.

Sutradhar, A.; Paulino, G. H.; Miller, M. J.; Nguyen, T. H. Topological optimization for designing patient-specific large craniofacial segmental bone replacements. *Proceedings of the National Academy of Sciences of the United States of America*, v. 107, n. 30, p. 13222–13227, July 2010.

Svanberg, K. The method of moving asymptotes—a new method for structural optimization. *International Journal for Numerical Methods in Engineering*, v. 24, p. 359–373, 1987.

Talischi, C.; Paulino, G.; Pereira, A.; Menezes, I. Polytop: a matlab implementation of a general topology optimization framework using unstructured polygonal finite element meshes. *Structural and Multidisciplinary Optimization*, v. 45, 02 2012.

Torquato, S.; Gibiansky, L.; Silva, M.; Gibson, L. Effective mechanical and transport properties of cellular solids. *International Journal of Mechanical Sciences*, v. 40, n. 1, p. 71–82, 1998.

Vieira, C. de S.; Marques, S. P. C. A new three-dimensional finite-volume model for evaluation of thermal conductivity of periodic multiphase composites. *International Journal of Heat and Mass Transfer*, v. 139, p. 412–424, 2019.

- Wang, C.; Zhao, Z.; Zhou, M.; Sigmund, O.; Zhang, X. S. A comprehensive review of educational articles on structural and multidisciplinary optimization. *Structural and Multidisciplinary Optimization*, Springer Science and Business Media Deutschland GmbH, v. 64, p. 2827–2880, 11 2021.
- Wang, M. Y.; Wang, X.; Guo, D. A level set method for structural topology optimization. *Computer Methods in Applied Mechanics and Engineering*, v. 192, n. 1, p. 227–246, 2003.
- Wang, Y.; Li, X.; Kai, L.; Wei, P. Open-source codes of topology optimization: A summary for beginners to start their research. *Computer Modeling in Engineering & Sciences*, v. 137, p. 1–34, 01 2023.
- Wu, J.; Sigmund, O.; Groen, J. P. Topology optimization of multi-scale structures: a review. *Structural and Multidisciplinary Optimization*, Springer Science and Business Media Deutschland GmbH, v. 63, p. 1455–1480, 3 2021.
- Xia, L.; Breitkopf, P. Design of materials using topology optimization and energy-based homogenization approach in matlab. *Structural and Multidisciplinary Optimization*, Springer Verlag, v. 52, p. 1229–1241, 12 2015.
- Xia, L.; Xia, Q.; Huang, X.; Xie, Y. Bi-directional evolutionary structural optimization on advanced structures and materials: A comprehensive review. *Archives of Computational Methods in Engineering*, v. 25, 11 2016.
- Yin, S.; He, Z.; Pindera, M.-J. A new hybrid homogenization theory for periodic composites with random fiber distributions. *Composite Structures*, v. 269, p. 113997, 2021.
- Zhao, X. et al. Microstructure design and optimization of multilayered piezoelectric composites with wavy architectures. *Mechanics of Advanced Materials and Structures*, p. 1–17, 02 2023.
- Zhong, Y.; Bansal, Y.; Pindera, M.-J. Efficient reformulation of the thermal higher-order theory for FGMs with locally variable conductivity. *International Journal of Computational Engineering Science*, v. 5, p. 795–832, 12 2004.
- Zhou, M.; Rozvany, G. The COC algorithm, part II: Topological, geometrical and generalized shape optimization. *Computer Methods in Applied Mechanics and Engineering*, v. 89, n. 1, p. 309–336, 1991.

APPENDIX A – SENSITIVITY EQUATIONS

In gradient-based techniques like the optimality criteria method, the knowledge of the derivatives (sensitivities) of the problem's objective function is crucial. This section elaborates on deriving the sensitivities of the effective constitutive matrix components for the two equivalent approaches utilized in this study.

Sensitivity equation for strain energy-based approach

Assuming the surface-averaged tractions due to the application of individual macroscopic strain case $\varepsilon|_{(\cdot)}$ as:

$$\hat{\mathbf{t}}^{(q)}|_{(\cdot)} = \mathbf{N}^{(q)}\mathbf{C}^{(q)}\bar{\boldsymbol{\varepsilon}}|_{(\cdot)} + \mathbf{K}^{(q)}\hat{\mathbf{u}}'^{(q)}|_{(\cdot)} = \mathbf{K}^{(q)}\hat{\mathbf{u}}_0^{(q)}|_{(\cdot)} + \mathbf{K}^{(q)}\hat{\mathbf{u}}'^{(q)}|_{(\cdot)} = \mathbf{K}^{(q)}\hat{\mathbf{u}}^{(q)}|_{(\cdot)} \quad (\text{B.1})$$

and the resultant of forces on the faces of the subvolume q ,

$$\mathbf{R}^{(q)}|_{(\cdot)} = \hat{\mathbf{H}}^{(q)}\bar{\boldsymbol{\varepsilon}}|_{(\cdot)} + \hat{\mathbf{K}}^{(q)}\hat{\mathbf{u}}'^{(q)}|_{(\cdot)} = \hat{\mathbf{K}}^{(q)}\hat{\mathbf{u}}_0^{(q)}|_{(\cdot)} + \hat{\mathbf{K}}^{(q)}\hat{\mathbf{u}}'^{(q)}|_{(\cdot)} = \hat{\mathbf{K}}^{(q)}\hat{\mathbf{u}}^{(q)}|_{(\cdot)}, \quad (\text{B.2})$$

once the summation of the homogenized and fluctuating displacement fields can be represented by Eq. (2), and $\hat{\mathbf{u}}_0^{(q)}|_{(\cdot)}$ is the surface-averaged homogenized displacement vector. This implies:

$$\hat{\mathbf{K}}\hat{\mathbf{u}}'|_{(\cdot)} = \hat{\mathbf{F}}|_{(\cdot)} = -\hat{\mathbf{K}}\hat{\mathbf{u}}_0|_{(\cdot)} \text{ and } \hat{\mathbf{K}}\hat{\mathbf{u}}_0|_{(\cdot)} + \hat{\mathbf{K}}\hat{\mathbf{u}}'|_{(\cdot)} = \hat{\mathbf{K}}\hat{\mathbf{u}}|_{(\cdot)} = \mathbf{0}, \quad (\text{B.3})$$

where $\hat{\mathbf{u}}_0|_{(\cdot)}$ is the global surface-averaged homogenized displacement vector and $\hat{\mathbf{u}}|_{(\cdot)}$ is the global total surface-averaged displacement vector. In terms of energetically conjugated quantities (force and displacement), the local stiffness matrix becomes symmetric and, therefore, $\hat{\mathbf{K}}^{(q)} = \hat{\mathbf{K}}^{(q)T}$. Thus, the derivatives of the effective constitutive matrix components, Eq. (28), are given by:

$$\frac{\partial C_{ij}^*}{\partial \rho_r} = \frac{1}{\Omega} \sum_{q=1}^{N_q} \hat{\mathbf{u}}^{(q)T}|_{(i)} \frac{\partial \hat{\mathbf{K}}^{(q)}}{\partial \rho_r} \hat{\mathbf{u}}^{(q)}|_{(j)} + \frac{2}{\Omega} \sum_{q=1}^{N_q} \hat{\mathbf{u}}^{(q)T}|_{(i)} \hat{\mathbf{K}}^{(q)} \frac{\partial \hat{\mathbf{u}}^{(q)}|_{(j)}}{\partial \rho_r}. \quad (\text{B.4})$$

Employing the relation of transformation in global/local displacements: $\hat{\mathbf{u}}^{(q)}|_{(\cdot)} = \mathbf{Q}^{(q)}\hat{\mathbf{u}}|_{(\cdot)}$,

$$\frac{\partial C_{ij}^*}{\partial \rho_r} = \frac{1}{\Omega} \hat{\mathbf{u}}^{(r)T}|_{(i)} \frac{\partial \hat{\mathbf{K}}^{(r)}}{\partial \rho_r} \hat{\mathbf{u}}^{(r)}|_{(j)} + \frac{2}{\Omega} \hat{\mathbf{u}}^T|_{(i)} \sum_{q=1}^{N_q} \mathbf{Q}^{(q)T} \hat{\mathbf{K}}^{(q)} \mathbf{Q}^{(q)} \frac{\partial \hat{\mathbf{u}}|_{(j)}}{\partial \rho_r}. \quad (\text{B.5})$$

Being $\hat{\mathbf{K}} = \sum_{q=1}^{N_q} \mathbf{Q}^{(q)T} \hat{\mathbf{K}}^{(q)} \mathbf{Q}^{(q)}$, which implies:

$$\frac{\partial C_{ij}^*}{\partial \rho_r} = \frac{1}{\Omega} \hat{\mathbf{u}}^{(r)T}|_{(i)} \frac{\partial \hat{\mathbf{K}}^{(r)}}{\partial \rho_r} \hat{\mathbf{u}}^{(r)}|_{(j)} + \frac{2}{\Omega} \hat{\mathbf{u}}^T|_{(i)} \hat{\mathbf{K}} \frac{\partial \hat{\mathbf{u}}|_{(j)}}{\partial \rho_r}. \quad (\text{B.6})$$

$$\frac{\partial C_{ij}^*}{\partial \rho_r} = \frac{1}{\Omega} \hat{\mathbf{u}}^{(r)T}|_{(i)} \frac{\partial \hat{\mathbf{K}}^{(r)}}{\partial \rho_r} \hat{\mathbf{u}}^{(r)}|_{(j)} + \frac{2}{\Omega} \mathbf{R}^T|_{(i)} \frac{\partial \hat{\mathbf{u}}|_{(j)}}{\partial \rho_r}. \quad (\text{B.7})$$

As $\mathbf{R}^T|_{(i)} = \mathbf{0}$,

$$\frac{\partial C_{ij}^*}{\partial \rho_r} = \frac{1}{\Omega} \hat{\mathbf{u}}^{(r)T}|_{(i)} \frac{\partial \hat{\mathbf{K}}^{(r)}}{\partial \rho_r} \hat{\mathbf{u}}^{(r)}|_{(j)}. \quad (\text{B.8})$$

Sensitivity equation for mean-field theory approach

Here, the derivatives of the effective constitutive matrix components are demonstrated by employing the classical micromechanics mean-field theory.

Applying a macroscopic strain case $\bar{\varepsilon}|_{(i)}$ on both sides of Eq. (31) and employing the Eq. (29) yields:

$$\bar{\varepsilon}^T|_{(i)} \mathbf{C}^* \bar{\varepsilon}|_{(j)} = \bar{\varepsilon}^T|_{(i)} \sum_{q=1}^{N_q} c^{(q)} \mathbf{C}^{(q)} \mathbb{A}^{(q)} \bar{\varepsilon}|_{(j)} = \bar{\varepsilon}^T|_{(i)} \sum_{q=1}^{N_q} c^{(q)} \mathbf{C}^{(q)} \bar{\varepsilon}^{(q)}|_{(j)}. \quad (\text{B.9})$$

The Hill's localization relation can be expressed as:

$$\bar{\varepsilon}^{(q)}|_{(j)} = \bar{\varepsilon}|_{(j)} + \bar{\mathbf{B}}^{(q)} \hat{\mathbf{u}}'^{(q)}|_{(j)}, \quad (\text{B.10})$$

where $\bar{\mathbf{B}}^{(q)}$ is the strain/displacement operator. Then,

$$\bar{\varepsilon}^T|_{(i)} \mathbf{C}^* \bar{\varepsilon}|_{(j)} = \bar{\varepsilon}^T|_{(i)} \sum_{q=1}^{N_q} c^{(q)} \mathbf{C}^{(q)} \left(\bar{\varepsilon}|_{(j)} + \bar{\mathbf{B}}^{(q)} \hat{\mathbf{u}}'^{(q)}|_{(j)} \right). \quad (\text{B.11})$$

Due to the imposition of the unit strain case, the effective constitutive matrix components can be evaluated as:

$$C_{ij}^* = \bar{\varepsilon}^T|_{(i)} \sum_{q=1}^{N_q} c^{(q)} \mathbf{C}^{(q)} \left(\bar{\varepsilon}|_{(j)} + \bar{\mathbf{B}}^{(q)} \hat{\mathbf{u}}'^{(q)}|_{(j)} \right). \quad (\text{B.12})$$

Similar to Christoff et al. (2019), consider the following Augmented Lagrangian functional:

$$L(\rho) = \bar{\varepsilon}^T|_{(i)} \sum_{q=1}^{N_q} c^{(q)} \mathbf{C}^{(q)} \left(\bar{\varepsilon}|_{(j)} + \bar{\mathbf{B}}^{(q)} \hat{\mathbf{u}}'^{(q)}|_{(j)} \right) + \hat{\boldsymbol{\lambda}}^T \left(\hat{\mathbf{K}} \hat{\mathbf{u}}'|_{(j)} - \hat{\mathbf{F}}|_{(j)} \right), \quad (\text{B.13})$$

where $\hat{\boldsymbol{\lambda}}$ is an arbitrary adjoint vector. The derivative of the Augmented Lagrangian functional in respect to ρ_r is given by:

$$\begin{aligned} \frac{\partial L(\rho)}{\partial \rho_r} &= \bar{\varepsilon}^T|_{(i)} \sum_{q=1}^{N_q} c^{(q)} \frac{\partial \mathbf{C}^{(q)}}{\partial \rho_r} \left(\bar{\varepsilon}|_{(j)} + \bar{\mathbf{B}}^{(q)} \hat{\mathbf{u}}'^{(q)}|_{(j)} \right) + \sum_{q=1}^{N_q} c^{(q)} \mathbf{C}^{(q)} \bar{\mathbf{B}}^{(q)} \frac{\partial \hat{\mathbf{u}}'^{(q)}|_{(j)}}{\partial \rho_r} \\ &+ \hat{\boldsymbol{\lambda}}^T \left(\frac{\partial \hat{\mathbf{K}}}{\partial \rho_r} \hat{\mathbf{u}}'|_{(j)} + \hat{\mathbf{K}} \frac{\partial \hat{\mathbf{u}}'|_{(j)}}{\partial \rho_r} + \sum_{q=1}^{N_q} \mathbf{Q}^{(q)T} \frac{\partial \hat{\mathbf{H}}^{(q)}}{\partial \rho_r} \bar{\varepsilon}|_{(j)} \right). \end{aligned} \quad (\text{B.14})$$

Employing the global/local displacements relation $\hat{\mathbf{u}}^{(q)}|_{(i)} = \mathbf{Q}^{(q)} \hat{\mathbf{u}}|_{(i)}$,

$$\begin{aligned} \frac{\partial L(\rho)}{\partial \rho_r} &= c^{(r)} \bar{\varepsilon}^T|_{(i)} \frac{\partial \mathbf{C}^{(r)}}{\partial \rho_r} \left(\bar{\varepsilon}|_{(j)} + \bar{\mathbf{B}}^{(r)} \hat{\mathbf{u}}'^{(r)}|_{(j)} \right) \\ &+ \left(\bar{\varepsilon}^T|_{(i)} \sum_{q=1}^{N_q} c^{(q)} \bar{\mathbf{B}}^{(q)T} \mathbf{C}^{(q)} \mathbf{Q}^{(q)} \right) \frac{\partial \hat{\mathbf{u}}'|_{(j)}}{\partial \rho_r} \\ &+ \hat{\boldsymbol{\lambda}}^T \left(\frac{\partial \hat{\mathbf{K}}}{\partial \rho_r} \hat{\mathbf{u}}'|_{(j)} + \hat{\mathbf{K}} \frac{\partial \hat{\mathbf{u}}'|_{(j)}}{\partial \rho_r} + \mathbf{Q}^{(r)T} \frac{\partial \hat{\mathbf{H}}^{(r)}}{\partial \rho_r} \bar{\varepsilon}|_{(j)} \right). \end{aligned} \quad (\text{B.15})$$

$$\begin{aligned}
\frac{\partial L(\rho)}{\partial \rho_r} &= c^{(r)} \bar{\varepsilon}^T|_{(i)} \frac{\partial \mathbf{C}^{(r)}}{\partial \rho_r} \left(\bar{\varepsilon}|_{(j)} + \bar{\mathbf{B}}^{(r)} \hat{\mathbf{u}}'^{(r)}|_{(j)} \right) \\
&+ \bar{\varepsilon}^T|_{(i)} \left(\sum_{q=1}^{N_q} c^{(q)} \bar{\mathbf{B}}^{(q)T} \mathbf{C}^{(q)} \mathbf{Q}^{(q)} + \hat{\boldsymbol{\lambda}}^T \hat{\mathbf{K}} \right) \frac{\partial \hat{\mathbf{u}}'|_{(j)}}{\partial \rho_r} \\
&+ \hat{\boldsymbol{\lambda}}^T \left(\frac{\partial \hat{\mathbf{K}}}{\partial \rho_r} \hat{\mathbf{u}}'|_{(j)} + \mathbf{Q}^{(r)T} \frac{\partial \hat{\mathbf{H}}^{(r)}}{\partial \rho_r} \bar{\varepsilon}|_{(j)} \right).
\end{aligned} \tag{B.16}$$

Consider the following equation, which aims to find an adjoint vector solution $\hat{\boldsymbol{\lambda}}$ that imposes the sum of the terms that multiply the derivatives of the surface-averaged fluctuating displacement vector to be zero:

$$\left(\bar{\varepsilon}^T|_{(i)} \sum_{q=1}^{N_q} c^{(q)} \bar{\mathbf{B}}^{(q)T} \mathbf{C}^{(q)} \mathbf{Q}^{(q)} + \hat{\boldsymbol{\lambda}}^T \hat{\mathbf{K}} \right) \frac{\partial \hat{\mathbf{u}}'|_{(j)}}{\partial \rho_r} = \mathbf{0}. \tag{B.17}$$

$$\hat{\boldsymbol{\lambda}}^T \hat{\mathbf{K}} = -\bar{\varepsilon}^T|_{(i)} \sum_{q=1}^{N_q} c^{(q)} \bar{\mathbf{B}}^{(q)T} \mathbf{C}^{(q)} \mathbf{Q}^{(q)}. \tag{B.18}$$

$$\hat{\mathbf{K}}^T \hat{\boldsymbol{\lambda}} = \hat{\mathbf{K}} \hat{\boldsymbol{\lambda}} = - \left(\sum_{q=1}^{N_q} c^{(q)} \mathbf{Q}^{(q)T} \mathbf{C}^{(q)} \bar{\mathbf{B}}^{(q)} \right) \bar{\varepsilon}|_{(i)}. \tag{B.19}$$

$$\begin{aligned}
\frac{\partial L(\rho)}{\partial \rho_r} &= c^{(r)} \bar{\varepsilon}^T|_{(i)} \frac{\partial \mathbf{C}^{(r)}}{\partial \rho_r} \left(\bar{\varepsilon}|_{(j)} + \bar{\mathbf{B}}^{(r)} \hat{\mathbf{u}}'^{(r)}|_{(j)} \right) \\
&+ \hat{\boldsymbol{\lambda}}^T \left(\frac{\partial \hat{\mathbf{K}}}{\partial \rho_r} \hat{\mathbf{u}}'|_{(j)} + \mathbf{Q}^{(r)T} \frac{\partial \hat{\mathbf{H}}^{(r)}}{\partial \rho_r} \bar{\varepsilon}|_{(j)} \right).
\end{aligned} \tag{B.20}$$

Being $\hat{\mathbf{K}} = \sum_{q=1}^{N_q} \mathbf{Q}^{(q)T} \hat{\mathbf{K}}^{(q)} \mathbf{Q}^{(q)}$,

$$\frac{\partial \hat{\mathbf{K}}}{\partial \rho_r} = \sum_{q=1}^{N_q} \mathbf{Q}^{(q)T} \frac{\partial \hat{\mathbf{K}}^{(q)}}{\partial \rho_r} \mathbf{Q}^{(q)} = \mathbf{Q}^{(r)T} \frac{\partial \hat{\mathbf{K}}^{(r)}}{\partial \rho_r} \mathbf{Q}^{(r)}. \tag{B.21}$$

Thus,

$$\begin{aligned}
\frac{\partial L(\rho)}{\partial \rho_r} &= c^{(r)} \bar{\varepsilon}^T|_{(i)} \frac{\partial \mathbf{C}^{(r)}}{\partial \rho_r} \left(\bar{\varepsilon}|_{(j)} + \bar{\mathbf{B}}^{(r)} \hat{\mathbf{u}}'^{(r)}|_{(j)} \right) \\
&+ \hat{\boldsymbol{\lambda}}^T \left(\mathbf{Q}^{(r)T} \frac{\partial \hat{\mathbf{K}}^{(r)}}{\partial \rho_r} \mathbf{Q}^{(r)} \hat{\mathbf{u}}'|_{(j)} + \mathbf{Q}^{(r)T} \frac{\partial \hat{\mathbf{H}}^{(r)}}{\partial \rho_r} \bar{\varepsilon}|_{(j)} \right).
\end{aligned} \tag{B.22}$$

$$\begin{aligned}
\frac{\partial L(\rho)}{\partial \rho_r} &= c^{(r)} \bar{\varepsilon}^T|_{(i)} \frac{\partial \mathbf{C}^{(r)}}{\partial \rho_r} \left(\bar{\varepsilon}|_{(j)} + \bar{\mathbf{B}}^{(r)} \hat{\mathbf{u}}'^{(r)}|_{(j)} \right) \\
&+ \boldsymbol{\lambda}^T \mathbf{Q}^{(r)T} \left(\frac{\partial \hat{\mathbf{K}}^{(r)}}{\partial \rho_r} \hat{\mathbf{u}}'^{(r)}|_{(j)} + \frac{\partial \hat{\mathbf{H}}^{(r)}}{\partial \rho_r} \bar{\varepsilon}|_{(j)} \right).
\end{aligned} \tag{B.23}$$

Employing the global/local relation $\hat{\boldsymbol{\lambda}}^{(q)} = \mathbf{Q}^{(q)} \hat{\boldsymbol{\lambda}}$,

$$\begin{aligned} \frac{\partial C_{ij}^*(\rho)}{\partial \rho_r} = \frac{\partial L(\rho)}{\partial \rho_r} = c^{(r)} \bar{\boldsymbol{\varepsilon}}^T|_{(i)} \frac{\partial \mathbf{C}^{(r)}}{\partial \rho_r} \left(\bar{\boldsymbol{\varepsilon}}|_{(j)} + \bar{\mathbf{B}}^{(r)} \hat{\mathbf{u}}^{(r)}|_{(j)} \right) \\ + \hat{\boldsymbol{\lambda}}^{(r)T} \left(\frac{\partial \hat{\mathbf{K}}^{(r)}}{\partial \rho_r} \hat{\mathbf{u}}^{(r)}|_{(j)} + \frac{\partial \hat{\mathbf{H}}^{(r)}}{\partial \rho_r} \bar{\boldsymbol{\varepsilon}}|_{(j)} \right). \end{aligned} \quad (\text{B.24})$$

APPENDIX B – COMPUTATIONAL PROCEDURE

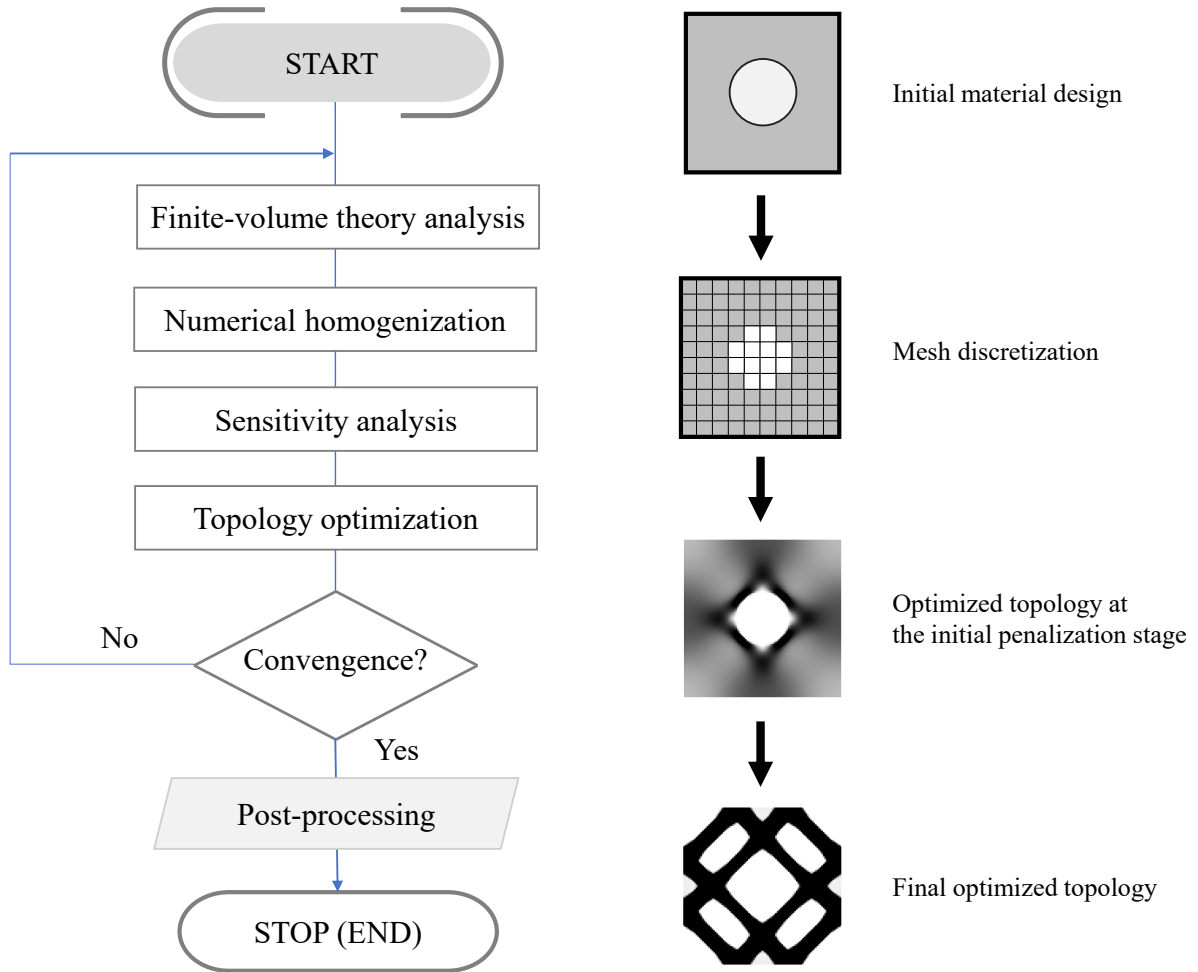
TopMatFVT is a Matlab computational code developed to design microstructures employing density-based topology optimization and finite-volume method. This code integrates material interpolation methods such as SIMP and RAMP to relax the design domain, aiming to achieve an effective optimized microstructural topology. Besides, it incorporates two paths for determining the effective properties of periodic cellular materials as an intermediate step of the optimization procedure. The objective functions are defined by combining linear constitutive matrix components to extremize specific materials' macroscopic properties. These properties include the material's shear/bulk moduli and negative Poisson's ratio in two-dimensional space, focusing on scenarios involving perforated sheets.

The proposed code is a collection of Matlab functions that implement the material properties, initial material design (RUC), finite-volume theory analysis, numerical homogenization, topology optimization, mesh-independency filters (not necessarily used), and post-processing. Initial material design is defined as containing a soft material region inside the domain to enable the calculation of the fluctuating displacement vector due to the material heterogeneity and the imposition of periodic boundary conditions.

A structured finite-volume mesh with a unitary subvolume containing isotropic elastic material properties and constant density is defined as input to the topology optimization problem. The choice of unitary subvolumes to circumvent eventual numerical imprecisions and accelerate the convergence process. Therefore, the main features of the topX code (Xia; Breitkopf, 2015) are now explored in this version, such as loop vectorization and memory preallocation, which are strengths of Matlab explored in this program. Periodic boundary conditions are implemented considering the equivalence between the degrees of freedom of the opposite edges of the periodic cell. Additionally, some parts of the code are moved out of the optimization loop, guaranteeing they are only performed once.

The finite-volume theory analysis is performed under a plane stress state, and the gradient-based topology optimization problem is solved using the optimality criteria (OC) method. The stopping criterion is a tolerance of $tol = 0.01$, representing the maximum allowable change in the design variables between successive iterations. Two mesh-independent filters are implemented based on the filtering approaches: sensitivity filter (Sigmund; Petersson, 1998) and density filter (Bourdin, 2001; Bruns; Tortorelli, 2001) implemented in efficient codes by Andreassen et al. (2011) and Xia and Breitkopf (2015). Finally, the algorithm prints the obtained optimized topology and the investigated numerical aspects, such as the number of iterations, processing time, objective function estimations, and effective constitutive matrix. Figure 19 illustrates the overview flowchart of the developed TopMatFVT computational code.

Figure 19 – Flowchart of the TopMatFVT for the topology optimization of periodic cellular materials



Font: Author (2024).